TRANSPORT PHENOMENA IN VISCOUS FLOW

AND

PARTICLE MOTION IN FLUIDIZED BEDS

by

WILLIAM JAMES MITCHELL, B.E. (Hons.)

A dissertation submitted in fulfillment of the requirements

for the degree of Master of Engineering Science

in the University of Adelaide

September, 1988

awarded 20.2.90

Department of Chemi[illegible]gineerin[illegible]

The [illegible]d laide

Adelaide, S.A. 5001

Australia

DECLARATION

This thesis contains no material which has been accepted for the award of any other degree or diploma in any University and, to the best of the author's knowlege and belief, the thesis contains no material previously published or written by another person, except where due reference is made in the text or where common knowledge is assumed.

The author consents to the thesis being made available for photocopying and loan if accepted for the award of the degree.

W.J. Mitchell

ACKNOWLEDGEMENTS

I would like to thank the following people and organizations for their help in this work:

- my supervisor, Dr. Pradeep Agarwal for his invaluable advice and guidance throughout this study;

- the rest of the academic staff and in particular, Mr. Michael Hounslow, Dr. Ravi Sankar and Dr. David Bogle for their help in parts of this study;

- the Commonwealth of Australia for a postgraduate research award and the University of Adelaide for a tutorship that provided the financial assistance;

- Colin Tipper, Andrew Wright, Peter Kay, Brian Mulcahy and Bruce Ide in the workshop for their assistance with the set up and consequent "debugging" of the experimental apparatus;

- the department secretaries, Mary Barrow and Heather Gordon for always having time to help me when I needed it;

- the other post-graduate students for helping me through this ordeal;

- my girlfriend, Sonia Wilson for her encouragement and friendship;

and - finally, my parents, Ann and Bill, for giving me both the opportunity and the confidence to come this far.

TABLE OF CONTENTS

LIST OF FIGURES

LIST OF TABLES

ABSTRACT

GENERALIZED INTERPHASE TRANSPORT PHENOMENA IN NEWTONIAN VISCOUS FLOW

- A single viscous drag relationship applicable to both internal flows through conduits of arbitrary cross-section and external flows over axisymmetric bodies has been developed.
- This has led to a generalised expression for the Chilton-Colburn heat/mass transfer factor, and generalised Sherwood/Graetz relationships.
- The model results have been compared with existing Leveque/Levich type solutions with excellent agreement.
- The work has enabled formulation of an analogy between momentum, mass and heat transport for slow flow conditions.

ACTIVE PARTICLE MOTION IN THE EMULSION PHASE OF A FLUIDIZED BED

- An equation of motion for an active, moving particle in liquid and gas fluidised beds (of inert particles) has been developed and solved.
- Comparisons have been made with the literature, and with experiments as part of the present work.
- The study has illustrated the importance of the formation of a defluidised cap of smaller particles on the top surface of the larger, active, upward moving particle.
- Necessary and sufficient conditions to determine whether an active particle will float or mix in particulate or bubbling fluidised beds have also been developed.

CHAPTER I

INTRODUCTION

1.1 OVERVIEW

The theory presented in the thesis extends the research of Agarwal and co-workers on Newtonian transport phenomena in multi-particle systems (Agarwal and O'Neill, 1988; Agarwal, 1988; Agarwal et al., 1988) to two other distinct areas of research interest.

In Agarwal and O'Neill (1988) and Agarwal (1988), expressions that predict the convective transport coefficients to spheres in multi-particle systems were developed. These model expressions were applicable over the whole range of porosity: from 0.26 for cubic close packed spheres to 1.0 for the isolated sphere. This was by virtue of a shape or cross-section factor, z, which could characterize the flow channel geometry at different bed porosities. Consequently, these papers effectively bridged the hydraulic radius (or equivalent conduit) model - conventionally applicable to only low bed porosities - with the submerged object (or individual particle) approach used most often at higher porosities. These results lend weight to the possibility of convective transport phenomena to a conduit or a tube being treated on the same basis (or by the same expressions) as an axisymmetric body (be it in an infinite fluid or a particle assemblage). This problem has been addressed in the first part of the thesis, for the viscous flow regime, by the methodology outlined below.

A generalized Reynolds number has been defined in terms of a generalized length parameter that is simply the ratio of the hydraulic radius, m, to the cross-section factor, z. This Reynolds number has been used to obtain a single drag relation that is applicable to flow through conduits, to flow over axisymmetric bodies and flat plates, and to flow over spheres in multi-particle systems in the viscous flow regime. Use of this drag relation in the thin thermal (concentration) boundary layer equations for well developed flow over flat plates and through conduits permits a more general solution for the transport coefficients under the constant wall temperature boundary condition. Appropriate rearrangement of this solution yields a simple expression for the Chilton-Colburn transfer factor. Alternatively, the generalized Sherwood (Nusselt) number is expressed in terms of a generalized Graetz number, Gz_G (which reduces to the Peclet number for a sphere). The results are compared with existing Leveque type solutions for different conduit geometries with excellent agreement. For axisymmetric bodies, the solution of the boundary equations involves a cumbersome integral (Lochiel and Calderbank, 1964); however, the simple expression for flow in conduits compares well with the rigorous results for creeping flow transfer from spheroids over a wide range of aspect ratios ($E > 0.5$). Further, this conduit solution has also been transformed to the particle-fluid heat (mass) transfer expression derived earlier by Agarwal (1988) and modified by Agarwal et al. (1988) for spheres in multi-particle systems. The good agreement obtained for different flow geometries has enabled the formulation of an analogy between momentum and mass (heat) transport for $Gz_G \to \infty$ and slow flow conditions. Finally, in analogy with the approximation obtained by bridging the $Pe \to \infty$ and the $Pe \to 0$ solutions for a sphere (Clift et al., 1978), simple empirical correlations have been developed for laminar forced convection heat (mass) transfer in conduits of different cross-section geometries over the whole Graetz number range.

The second part of the study was motivated by the current interest (LaNauze, 1985) in the estimation of the mass transfer of oxygen to coal particles burning in

fluidized bed combustors. In Agarwal et al. (1988), a mechanistic model for mass transfer to an active-sphere in bubbling gas fluidized beds of inert particles was developed. As in the fluidized bed combustion of coal, the active particle was considered to have a different size and density to that of the inert bed material (the inerts were assumed to make up over 95% of the bed). The model assumed that the active particle could reside in both the emulsion or particle rich phase (where the particle was assumed to move down) and the bubble or particle lean phase (where the particle moves up). The analysis of the emulsion phase assumed that the active-particle would move at the same velocity as the inert particles. However, the different size and density of the active particle would be expected to produce a motion different from that of the inert particles. To determine its effect on the mass transfer rate to the active particle, it is obvious that an expression for this velocity is required. This problem has been addressed in the second part of the thesis by solving the force or momentum balance (that is, the equation of motion) for the active particle. To do this the relevant forces acting on the particle, whilst in the emulsion phase, need to be determined. These have been identified as:

1) a fluid drag force (the expression used allowed for the increase in drag due to the presence of neighbouring particles);

2) a weight plus buoyancy force that was assumed to be proportional to the difference in density between the active particle and the suspension;

and 3) a particle interaction force that accounted for collisions between the active and inert particles (as a direct result of their relative motion).

An analytical expression for the steady-state or terminal segregation velocity has been obtained by neglecting the acceleration term. Comparison with literature experimental data for the terminal velocities of heavy spheres falling through both liquid and particulate gas fluidized beds is excellent. Further, the dynamic response is obtained by

numerical integration of the full force balance equation. Experiments, where light particles would rise to the top of a liquid fluidized bed, have been performed by the author to verify the behaviour predicted by the model. A criterion that predicts the conditions when the active particles may float at the top of either particulate or bubbling fluidized beds is also developed by consideration of the active particle force balance coupled with knowledge of the inert particle movement (in the case of bubbling gas fluidized beds). The model is in exact agreement with the experiments of Chiba et al. (1980). Finally, implications for mass transfer studies in gas fluidized beds are also discussed.

CHAPTER II

GENERALIZED INTER-PHASE TRANSPORT PHENOMENA IN VISCOUS FLOW

2.1 INTRODUCTION

2.1.1 Background

There is a wide range of important applications in several engineering disciplines that require knowledge of the interphase forced convection transport phenomena that occur in conduits of different cross-sections and from particulate systems in the viscous flow regime: for example, knowledge of the pressure drop and the heat transfer rates in plate, and shell and tube heat exchangers; determination of the mass transfer rate from spheroidal bubbles in fermenters and bubble column reactors as well as mass and heat transport rates to and from spherical catalyst particles in fixed and fluidized bed reactors.

Flow in the viscous flow regime results in a drag coefficient that is inversely proportional to the Reynolds number

$$(Drag\,coefficient) = K_d(Reynolds\,number)^{-1} \qquad (1)$$

The effect of the flow geometry is considered by appropriate definition of the proportionality factor, K_d, and the inclusion of a suitable length parameter in the Reynolds number.

Mass/heat transfer correlations in this flow regime and under high Graetz number conditions (or Peclet number for a sphere) can be derived from the Leveque (1928) and/or the Levich (1962) type solution as

$$(Sherwood\,number) = B\,(Graetz\,number)^{1/3} \qquad (2)$$

where B is a proportionality constant. As for momentum transport, the definition of the factor, B, as well as the inclusion of an appropriate length parameter in the Nusselt number accounts for the effect of flow geometry. At low Graetz numbers, the Nusselt number solution asymptotes to a constant value.

The main research effort has been directed at the determination of the coefficients K_d and B for different geometries with the Reynolds or Nusselt number being based on an "equivalent" diameter (for example, the hydraulic diameter if conduits are being considered).

To extend the results for momentum transfer to heat/mass transfer, analogies between transport phenomena have been proposed in the literature (Jakob, 1949). These analogies, however, are more successful in the turbulent flow regime.

Recent work on unifying the hydraulic radius and submerged object approaches for modelling macroscopic momentum transfer in multi-particle systems (Agarwal and O'Neill, 1988) and its extension to particle-fluid heat/mass transfer (Agarwal, 1988) indicates, however, that there is a possibility for treating the Newtonian viscous flow transfer processes in conduits and around axisymmetric bodies on a common basis.

2.1.2 Objectives

The main objectives of this study, applicable only to viscous flow conditions, are to:

1) collapse the various expressions for the drag coefficient in different geometries to a single expression by incorporating the geometry factor, K_d, in the definition of a generalized length parameter;

2) collapse the various high Graetz number correlations for the heat/mass transport coefficients in different geometries to a single expression by expressing the geometry factor, B, as a function of the generalized length parameter;

3) obtain an analogy between momentum and heat/mass transport;

and 4) extend the heat/mass transfer analysis to develop correlations applicable to the whole Graetz number range.

2.2 LITERATURE SURVEY

Most of the literature involved with research on viscous flow transport phenomena are already available in the form of comprehensive reviews. So rather than rewrite them, only the salient aspects of the reviews will be presented here.

DUCTS: Pressure loss in conduits of arbitrary shape under viscous flow conditions have been analysed by Davies and White (1929) as discussed by Jakob (1949). The constant, K_d, in the drag coefficient expression (equation 1), was expressed as $N_f L/d_h$ where d_h is the hydraulic diameter and N_f is an individual constant for each shape of the cross-section. Values of N_f for different geometries are presented in Table 1. More recently, Shah and London (1978) have presented more extensive data for the K_d factor as $(4f)Re_{d_h} L/d_h$ where f is the Fanning friction factor. An example of the fRe_{d_h} data tabulated by Shah and London (1978) for elliptical ducts is shown in Table 2.

An extensive compilation of the available solutions for forced convection heat transfer in the viscous flow of Newtonian fluids through conduits of different geometries, up to 1975, has been given in Shah and London (1978). Solutions were presented for:

1) all the common duct geometries such as rectangular, elliptical, triangular, parallel plates, and annulii;

2) all possible flow conditions, that is, fully developed flow as well as both hydrodynamically and/or thermally developing flow;

and 3) various boundary conditions (amongst them being, the constant wall temperature and constant wall heat flux conditions).

TABLE 1

Constant N_f for use in the Pressure Drop Equation of Davies and White (1929) for Different Conduit Geometries (from Jakob, 1949)

Conduit geometry	Aspect ratio, E	N
Ellipse	1.000	64
	0.700	65
	0.500	68
	0.300	73
	0.200	76
	0.100	78
Rectangle	1.000	57
	0.500	62
	0.333	69
	0.250	73
	0.200	76
	0.100	85
	0.000	96
Equilateral triangle	0.866	53

TABLE 2

fRe_{d_h} factor for the Estimation of the Pressure Drop in Elliptical Conduits (from Shah and London, 1978)

Aspect ratio, E	fRe_{d_h}
1.000	2.000
0.900	2.003
0.800	2.012
0.750	2.020
0.667	2.039
0.600	5.493
0.500	2.103
0.400	2.162
0.333	2.210
0.250	2.280
0.200	2.325
0.167	2.356
0.125	2.393
0.100	2.414
0.050	2.450
0.000	2.467

Numerical data derived from these solutions were given over the whole Graetz number range, that is, incorporating the Leveque solution for high Graetz numbers and the constant asymptotic solution for low Graetz numbers. Data for the constant wall temperature condition are given in Appendix C. The proportionality constant, B, in the Leveque solution (equation 2) was derived in terms of the fRe_{d_h} product (as used in the K_d factor above) from intuitive arguments. Churchill and Ozoe (1973) bridged the high Graetz solution, Nu^{∞} with the low Graetz solution, Nu^{0} for an isothermal tube by assuming the form

$$(Nu)^n = (Nu^0)^n + (Nu^\infty)^n \tag{3}$$

to obtain a rather complex correlation for the Nusselt number, Nu that was applicable for all Graetz numbers. The adjustable parameter, n was chosen as 8/3 and the length parameter in the Nusselt number was the tube diameter. The authors themselves admit that the final relation "appears to be somewhat ungainly" but claim that their expression is the still the simplest possible.

AXISYMMETRIC BODIES: Transport phenomena associated with isolated spherical and non-spherical bodies have been reviewed by Clift et al. (1978).

The drag force for spheroidal particles was expressed in terms of a "principal translational resistance", C_f. This resistance factor could be interpreted in terms of the K_d factor as $(4\pi C_f)/a$ where a is the equatorial radius of the spheroid. Values for C_f are given in Table 3 for the oblate and the prolate spheroid as determined from Happel and Brenner (1983).

TABLE 3

Resistance Factor, C_f to Calculate the Drag Coefficient for Spheroids in Creeping Flow (from Happle and Brenner, 1983)

Oblate Spheroid (E < 1)	Prolate Spheroid (E > 1)
axial flow	
Exact solution	
$\frac{8\pi a(1-E^2)}{(1-2E^2)\cos^{-1}(E/\sqrt{(1-E^2)})+E}$	$\frac{8\pi a(E^2-1)}{(2E^2-1)\ln((E+\sqrt{(E^2-1)})/\sqrt{(E^2-1)})-E}$
Approximate solution	
$1.2\pi a(4+E)$	$1.2\pi a(4+E)$
normal flow	
Exact solution	
$\frac{16\pi a(1-E^2)}{(3-2E^2)\cos^{-1}(E/\sqrt{(1-E^2)})-E}$	$\frac{16\pi a(E^2-1)}{(2E^2-3)\ln((E+\sqrt{(E^2-1)})/\sqrt{(E^2-1)})+E}$
Approximate solution	
$1.2\pi a(3+2E)$	$1.2\pi a(3+2E)$

- 2a is the maximum dimension normal to the axis of symmetry (i.e. equatorial diameter)
- the approximate solution gives a good estimate of the more complex exact solution over the whole E range for axial flow and within 10% for normal flow when $E \leq 5$)

The Levich solution constant, B, for spheroidal particles was presented in graphical form from the calculations of Sehlin (1969) over the range of aspect ratio 0.1 to 10 (see Figure 3). The length parameter used in the Nusselt number was twice the equatorial radius of the spheroid.

MULTI-PARTICLE SYSTEMS: Experimental data and hydraulic radius models for pressure loss in porous media have been discussed by Carmen (1956) and Scheidegger (1960). Criticism has been directed at the hydraulic radius approach (Molerus, 1980); the major objection being that the limiting resistance for a single particle is not predicted as $\varepsilon \to 1$ where ε is the bed porosity. A submerged object approach has also been applied, but the resulting expressions predict too small a dependence on solids concentration. However, extension of the hydraulic radius approach to higher porosities has been successfully achieved by Andersson (1961). A porosity dependent cross-section factor, z that accounts for the dependence of the viscous flow drag loss on the flow geometry was defined. The viscous flow pressure drop can be written as

$$\frac{\Delta p}{L} = z q^2 \frac{(1-\varepsilon)^2 \mu}{\varepsilon^3 d_p^2} U_0 \tag{4}$$

where q is the tortuosity factor, μ is the fluid viscosity and U_0 is the superficial fluid velocity. Agarwal and O'Neill (1988) combined this expression with a submerged object model to obtain an expression for the particle drag coefficient, so that the K_d factor could be written as $48z(1-\varepsilon)$ for this flow geometry. The length parameter used in the Reynolds number was simply the particle diameter.

Agarwal (1988) presented a comprehensive review of the work done on heat/mass transfer to spheres in multi-particle systems. A model for forced convection heat/mass transfer was also proposed with good agreement with

experiment over a wide range of Reynolds and Schmidt numbers. Problems with the viscous flow data for gases (low Schmidt numbers) were rationalized by Agarwal et al. (1988). Under viscous flow conditions the model can be reduced to the standard Levich solution with the B factor being a complex function of the bed properties. It is important to note that a number of experimental studies have been performed in the viscous flow regime and under high Pe conditions which will allow model verification (at least for transport in multi-particle systems)

2.3 MODEL DEVELOPMENT

2.3.1 Momentum Transfer: derivation of the m/z factor

The generalized Reynolds number, Re_G, is defined as

$$Re_G = \left(\frac{3m}{z}\right)\left(\frac{\overline{U}}{\nu}\right) \tag{4}$$

where $\overline{U}$ is the average approach velocity, ν is the kinematic viscosity and m is the hydraulic radius defined in the conventional sense as the ratio of the cross-sectional area to the wetted perimeter. The cross-section factor, z, is a geometric parameter which depends on the shape of the cross-section of the flow path perpendicular to the direction of the flow (Andersson, 1961; Agarwal and O'Neill, 1988). For regular conduits, z is identical to the Kozeny shape factor (Carman, 1956). The values of z for different cross-sections and aspect ratios are plotted, as calculated from the tabulations provided by Shah and London (1978), in Figure 1. For multi-particle systems, z depends on the system voidage, ε, since ε characterises the flow channel geometry (Andersson, 1961). Expressions for z as a function of bed porosity are presented in Table 4 in terms of the modified Kozeny factor, zq^2 (equation 4). In the limit of $\varepsilon \rightarrow 1$ for multi-particle systems, the ratio (m/z) approaches a constant value independent of the porosity; the limiting values for different axisymmetric bodies are discussed later. It is postulated that (m/z) is the generalized length parameter for inclusion in the Reynolds number. This definition of the Reynolds number was first proposed by Andersson (1961) for liquid fluidized beds; however, its general applicability was not recognized. The factor of 3 is introduced in equation 4 to ensure that for an isolated sphere of diameter d_p, Re_G reduces to the conventional particle Reynolds number $Re_p = Ud_p/\nu$ since the approach velocity is equivalent to the superficial

TABLE 4

Modified Kozeny Factor and Tortuosity Factor Expressions for the Evaluation of z in Multi-Particle Systems

Parameter		Equation
zq^2	$\varepsilon < 0.5$:	$5.3\left(\frac{\varepsilon}{1-\varepsilon}\right)^{0.3}$
	$\varepsilon > 0.5$:	$\frac{1}{2}\frac{\varepsilon^3}{1-\varepsilon}\left(\frac{1+4.7(1-\varepsilon)}{1-1.83(1-\varepsilon)}\right)$
q		$\frac{1}{1-0.9(\varepsilon-0.25)^{1/3}(1-\varepsilon)^{2/3}}$

taken from: , Andersson (1961); , Reed and Anderson (1980) as derived in Agarwal and O'Neill (1988)

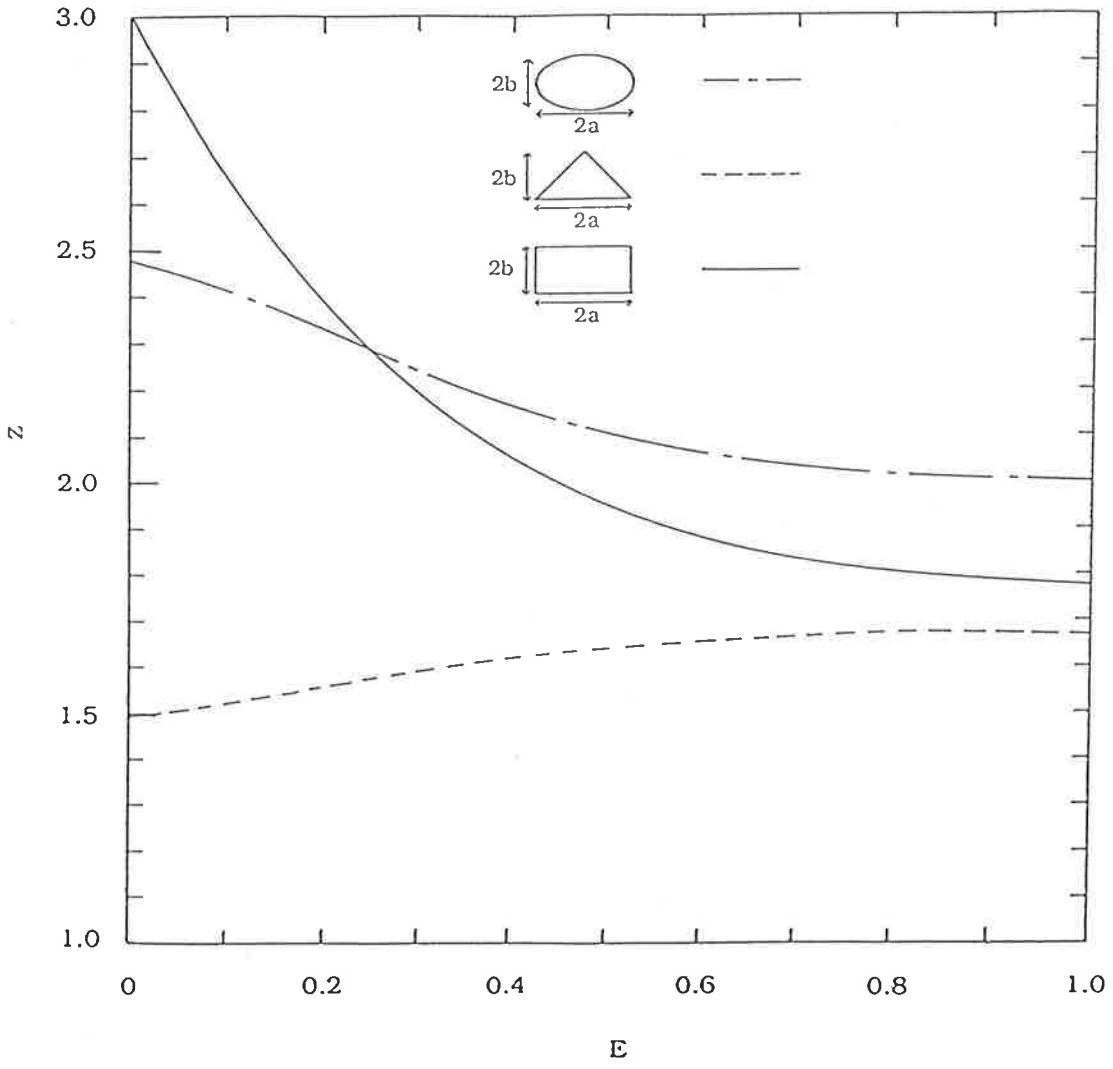

Figure 1 : z Factors for the Common Duct Geometries

velocity and (Agarwal and O'Neill, 1988)

$$\left(\frac{m}{z}\right)_{sphere} = \frac{d_p}{3} \tag{5}$$

For an assemblage of spheres, the average approach (interstitial) velocity is Uq/ε where q is a tortuosity factor. Using the conventional definition of the hydraulic radius for granular porous media composed of spherical particles ($m = d_p\varepsilon/6(1-\varepsilon)$), it can be shown that Re_G reduces to $Re_\varepsilon = Re_p q/2z(1-\varepsilon)$, a multi-particle Reynolds number used earlier by Agarwal and O'Neill (1988).

The generalized drag factor, ϕ, is defined as

$$\phi = \frac{(F_d/A_s)}{\frac{1}{2}\rho\,\overline{U}^2} \tag{6a}$$

where F_d is the average drag force on the surface area A_s. F_d/A_s may be related to the pressure loss per unit length, $\Delta P/L_e$, as

$$\frac{F_d}{A_s} = \frac{\Delta P}{L_e} m \tag{6b}$$

L_e is the total length of the flow channel. Also by analogy with Jakob (1949) we may write

$$\frac{\Delta P}{\frac{1}{2}\rho\overline{U}^2} = \left(\frac{2z}{m}\right)\left(\frac{L_e}{m}\right)\left(\frac{\nu}{\overline{U}}\right) \tag{6c}$$

Equations 4 and 6a-c may be used to obtain the generalized drag relation as

$$\phi = \frac{6}{Re_G} \tag{7}$$

It may be verified that equation 7 applies to conduits as well as to an isolated sphere (keeping in mind that the drag factor used here is based on the surface area whereas the conventional drag coefficient for a sphere is based on the maximum projected area normal to the flow).

The applicability of the generalized Reynolds number would be limited for external flows if the knowledge of the relevant (m/z) factors was confined only to the sphere. In Appendix A, however, the drag force expression given in equation 6a is compared with expressions available in the literature for drag on axisymmetric bodies in the viscous flow regime. This step yields an equation for (m/z) applicable to all axisymmetric bodies

$$\left(\frac{m}{z}\right)=\frac{8}{\pi K_1}\frac{A_s}{d_e} \tag{8}$$

K_1 is defined in equation A.3 in Appendix A. Several bases can be used to define the equivalent sphere diameter, d_e (Clift et al., 1978); however, (d_eK_1) is independent of the definition. Values of (m/z) for different axisymmetric bodies under axial/normal flow can be obtained using equation 8 and are presented in Table 5.

To obtain (m/z) for a flat plate of length L, the analytical solution (Jakob, 1949) for the corresponding friction factor in terms of $Re_L=\overline{U}L/\nu$

$$\phi=(4/3)Re_L^{-1/2} \tag{9}$$

is combined with equation 7 (as for axisymmetric bodies) to give

$$\left(\frac{m}{z}\right)_{plate}=(9/20)\delta_m \tag{10a}$$

where δ_m, the surface average boundary layer thickness, is given by

$$\delta_m=(10/3)LRe_L^{-1/2} \tag{10b}$$

and

$$Re_G=(9/2)Re_L^{1/2} \tag{10c}$$

The above expressions for (m/z) have been obtained using viscous flow solutions simply because it was convenient to do so. Conceptually, the (m/z)

TABLE 5

(m/z) factors for axisymmetric bodies

Body	d_e	$f(E) = A_s/(2\pi a^2)$	Flow Direction	K_1*	$\left(\frac{m}{z}\right)$
Sphere (E = 1)	2a	2	axial	24	$\frac{2a}{3}$
			normal	24	$\frac{2a}{3}$
Prolate Spheroid (E > 1)	2a	$1+\frac{E^2}{e}\sin^{-1}\left(\frac{e}{E}\right)$	axial	$4.8(4+E)$	$\frac{8af(E)}{4.8(4+E)}$
		$e=\sqrt{E^2-1}$	normal	$4.8(3+2E)$	$\frac{8af(E)}{4.8(3+2E)}$
Oblate Spheroid (E < 1)	2a	$1+\frac{1}{2}\frac{E^2}{e}\ln\left(\frac{1+e}{1-e}\right)$	axial	$4.8(4+E)$	$\frac{8af(E)}{4.8(4+E)}$
		$e=\sqrt{1-E^2}$	normal	$4.8(3+2E)$	$\frac{8af(E)}{4.8(3+2E)}$

* : from Clift et al. (1978) and Happel and Brenner (1983)

factor is thought to be a geometric quantity. This is clearly so for internal flow through ducts (Figure 1) and external flow over axisymmetric bodies (Table 5). Additional work is required to determine the applicability of m/z for these cases to turbulent flow conditions. Recent work on multiparticle systems (Agarwal and O'Neill, 1988) however, indicates that m/z obtained from viscous flow considerations can apply to the turbulent flow regime as well. The flat plate remains an anamoly because, although m/z depends on the boundary layer thickness, δ_m (which is a geometry factor), it also depends on the flow conditions since δ_m is a function of Re_L.

2.3.2 Heat and Mass Transfer

We next consider mass transfer from different bodies under the thin concentration boundary layer limit. The mass transfer rate across any surface element of area dA may be found by applying Fick's law

$$k_x^{\infty}(c_s - c_0)dA = -D\left(\frac{\partial c}{\partial y}\right)_{y=0} dA \qquad (11a)$$

where k_x^{∞} is the peripheral average (local) mass transfer coefficient (based on the initial concentration difference) and D is the mass diffusivity. The co-ordinate systems defining x and y are considered in detail in Appendix B. The overall transfer rate is given by

$$k_m^{\infty}A_s(c_s - c_0) = -\int_{A_s} D\left(\frac{\partial c}{\partial y}\right)_{y=0} dA \qquad (11b)$$

where k_m^{∞} is the surface average mass transfer coefficient (also based on the initial concentration difference). In terms of the dimensionless concentration, c_1 (defined in Appendix B)

$$k_m^{\infty} = -\frac{D}{A_s}\int_0^{L_f}\left(\frac{\partial c_1}{\partial y}\right)_{y=0} P_w dx \qquad (12)$$

where P_w is the local wetted perimeter which, in general, depends on the distance, x, along the flow path of length, L_f. The local wetted perimeter may be represented as $(P_w)_{r=1.0}\, r$; where for a flat plate $(P_w)_{r=1.0}$ is the plate width and 2π for axial flow over an axisymmetric body. Using the expressions for the dimensionless concentration gradient at the surface (equation B.15) and $d\chi$ (equation B.12b) given in Appendix B, we obtain in the thin concentration boundary layer limit

$$k_m^{\infty} = \frac{(P_w)_{r=1.0}}{A_s}\frac{1}{\Gamma(4/3)\,9^{1/3}}\int_0^{x=L_f}\frac{d\chi}{\chi^{1/3}} \qquad (13)$$

Integration leads to the general expression for the mass transfer coefficient as

$$k_m^{\infty} = D^{2/3}\frac{(P_w)_{r=1.0}}{A_s}\frac{(3/2)}{\Gamma(4/3)\,9^{1/3}}\left(\int_0^{L_f}(u_0' r)^{1/2}\, r\, dx\right)^{2/3} \qquad (14)$$

For flow over axisymmetric bodies, equation 14 is similar to that obtained by Lochiel and Calderbank (1964). Since, in this case, the dimensionless velocity gradient is a function of x, analytical integration has been considered cumbersome (Lochiel and Calderbank, 1964; Clift et al., 1978).

For fully developed flow over a flat plate and through conduits, r is constant and will be cancelled from the above expressions. The velocity gradient is also constant i.e. $u_0' = (u_0')_m$ and can be shown, using equations 6a and 7, to be

$$(u_0')_m = \frac{\overline{U}}{(m/z)} \qquad (15)$$

Hence using equations 14 and 15, for the flat plate and conduits,

$$j_d = St_m^{\infty} Sc^{2/3} = 1.68\left(\frac{m/z}{L_f}\right)^{1/3} Re_G^{-2/3} \tag{16}$$

where j_d is the Chilton-Colburn transfer factor and $St = k/\overline{U}$.

The generalized Sherwood number is defined as

$$Sh_G = \left(\frac{3m}{z}\right)\left(\frac{k}{D}\right) \tag{17a}$$

and the generalized Graetz number as

$$Gz_G = \left(\frac{3\pi}{2}\right)\left(\frac{m/z}{L_f}\right) Re_G Sc \tag{17b}$$

The reason for choosing the form of equation 17b will be clarified later. From equations 16 and 17a-b,

$$Sh_{G,m}^{\infty} = 1.68\left(\frac{m/z}{L_f}\right)^{1/3} Re_G^{1/3} Sc^{1/3} = Gz_G^{1/3} \tag{18}$$

Similarly, local peripheral average values of the mass transfer coefficient are derived by solving equation 11a directly, yielding

$$St_x^{\infty} Sc^{2/3} = 1.12\left(\frac{m/z}{x}\right)^{1/3} Re_G^{-2/3} \tag{19}$$

or in terms of the generalized Sherwood number,

$$Sh_{G,x}^{\infty} = 1.12\left(\frac{m/z}{x}\right)^{1/3} Re_G^{1/3} Sc^{1/3} \tag{20}$$

The above relations have been derived for mass transfer only; equivalent expressions for heat transfer can be obtained by replacing Sh_G and Sc by Nu_G (defined in an analogous manner) and Pr respectively.

2.4 RESULTS AND DISCUSSION

2.4.1 Momentum Transfer

As discussed earlier, the generalized drag relation given by equation 7 applies to flow through conduits as well as over flat plates and axisymmetric bodies using appropriate values of the (m/z) factor. For an assemblage of spherical particles, combining equations 6a and b, and using $\overline{U} = U_0 q/\varepsilon$ with $m = d_p\varepsilon/(6(1-\varepsilon))$ and $L_e = qL$, it may be shown that

$$\phi = \left(\frac{1}{3}\right)\left(\frac{\Delta P}{L}\right)\left(\frac{d_p}{\rho U_0^2}\right)\left(\frac{\varepsilon^3}{q^3(1-\varepsilon)}\right) \qquad (21a)$$

where L is the bed height. This multi-particle system friction factor differs from the one proposed earlier (Agarwal and O'Neill, 1988) by only a constant. In Figure 2, the generalized drag factor, ϕ, is plotted as a function of Re_G. The data for multi-particle systems analyzed earlier by Agarwal and O'Neill (1988) based on experimental observations reported in the literature have also been transposed, for $Re_G \leq 100$, on this generalized plot. Limitations to the applicability of our generalized drag model, due to the onset of turbulence or increased contribution from the inertial term, are still dictated by the flow geometry. The critical Re_G for the onset of turbulence is about 860 for a tube of circular cross-section, and about 3200 for a flat plate. For multi-particle systems, the agreement is generally good for $Re_G < 10$. Since the inertial contribution, for an isolated sphere, becomes increasingly important for $Re_G > 0.1$, it is thought that the transition Re_G for particulate systems would also depend on the system voidage. This could explain the relatively large scatter obtained by Agarwal and O'Neill (1988) for the experimental data in the intermediate region as compared with the good agreement obtained in the lower and higher Reynolds number regimes.

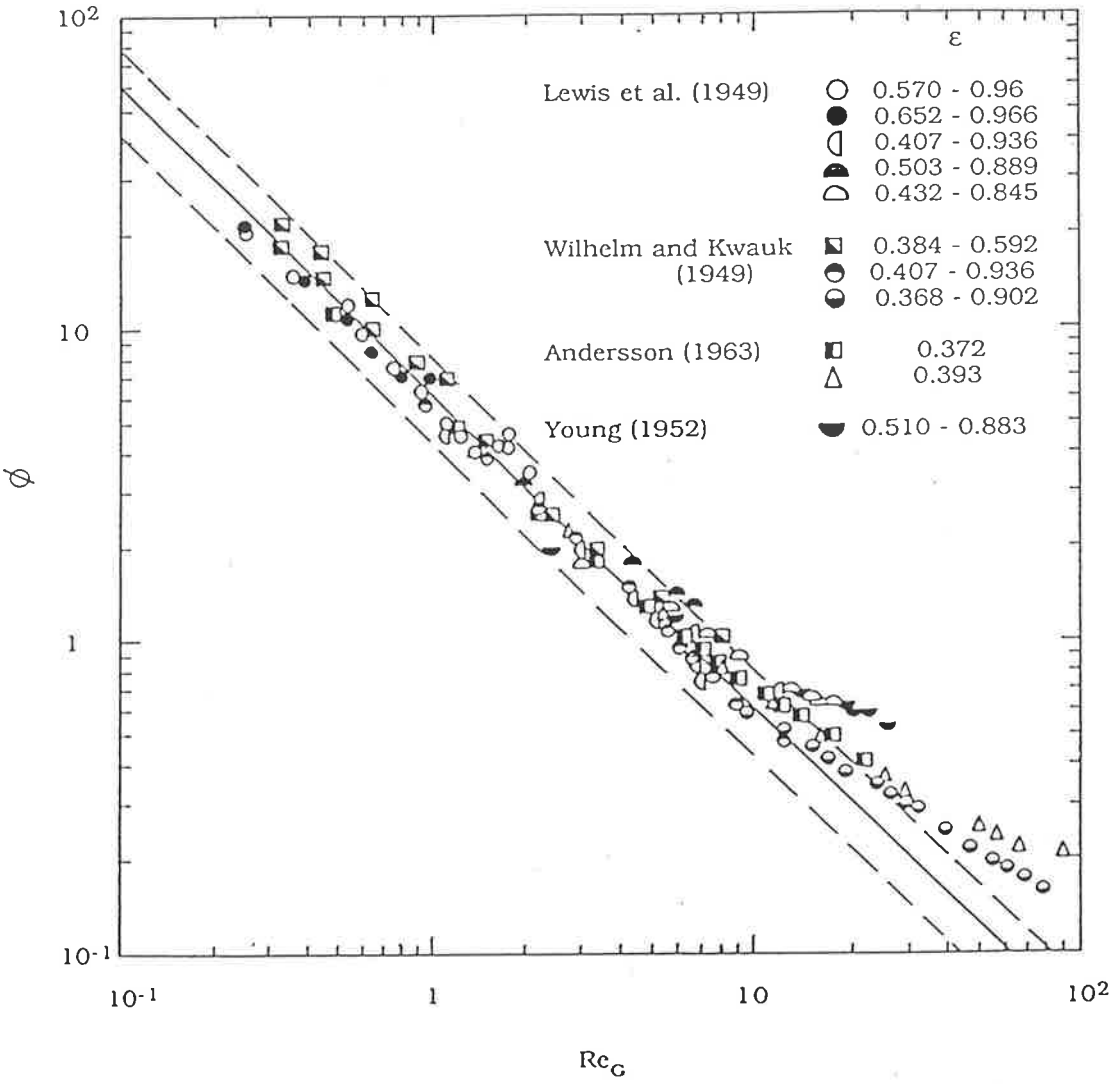

Figure 2 : Generalized Drag Factor as a function of the Generalized Reynolds Number for Conduits, Axisymmetric Bodies, Flat Plates and Multi-particle Systems in the Viscous Flow Regime : comparison of equation 7 with multi-particle system data

2.4.2 Heat/Mass Transfer in the Thin Thermal/Concentration Boundary Layer Limit (high Graetz number)

DUCTS: The conventional form for the Leveque type solution, under the thin thermal boundary layer (or $Gz_G \to \infty$) and fully developed flow assumptions, for laminar heat transfer in ducts of arbitrary cross section is

$$\mathrm{Nu}^{\infty}_{d_h,m} = B_m \, Re^{1/3}_{d_h} \, Pr^{1/3} \left(\frac{d_h}{L_e}\right)^{1/3} \tag{22}$$

where B_m depends only on geometry and d_h (= 4m) is the conventional hydraulic diameter. Equation 16 can be rearranged, with $L_f = L_e$, in terms of d_h resulting in a form similar to the above expression for ducts

$$\mathrm{Nu}^{\infty}_{d_h,m} = (1.282 z^{1/3}) \, Re^{1/3}_{d_h} \, Pr^{1/3} \left(\frac{d_h}{L_e}\right)^{1/3} \tag{23}$$

This leads to

$$B_m = 1.282 z^{1/3} \tag{24a}$$

and likewise for the peripheral average expression

$$B_x = 0.855 z^{1/3} \tag{24b}$$

Equations 23 and 24a-b, in a different form and obtained from intuitive arguments, have been used earlier by Shah and London (1978). Comparison of B_m and B_x values reported in the literature with the expressions given in equations 24 a-b are presented in Table 6. Conduit geometries considered are elliptic (including the slit and cylinder), rectangular (including parallel plates) and triangular cross-sections. For elliptic ducts, the calculated values of B_x and B_m are in good agreement with the results of James (1970) and Richardson (1980) respectively, for the entire range of aspect ratios. The values of B_m and B_x obtained by Rao et al. (1969), though in agreement with the present theory for extreme values of E, show a marked maximum for intermediate values of the aspect ratio. However, experimental work reported more recently (Oliver and

Table 6

Local and Average Nusselt Numbers for Heat Transfer in Conduits

Conduit Type	Aspect Ratio, E	z (Fig 1)	$B_x = \mathrm{Nu}^{\infty}_{d_h,x}\left(Re_{d_h} Pr \frac{d_h}{x}\right)^{-1/3}$ This Theory (eqn 24b)	B_x Literature Results	$B_m = \mathrm{Nu}^{\infty}_{d_h,m}\left(Re_{d_h} Pr \frac{d_h}{L_f}\right)^{-1/3}$ This Theory (eqn 24a)	B_m Literature Results	$\mathrm{Nu}^{0}_{d_h}$	$\mathrm{Nu}_{d_h,x}$ for all Gz_G (eqn 34c) K_5	Mean Error (%)	σ (%)	$\mathrm{Nu}_{d_h,m}$ for all Gz_G (eqn 34b) K_4	Mean Error (%)	σ (%)
Elliptical	1.000	2.000	1.077	1.070	1.615	1.615	3.657	4.7	1.7	2.3	4.6	0.7	0.8
	0.400	2.162	1.106	1.093	1.658	1.641							
	0.250	2.280	1.125	1.110	1.687	1.659	3.792						
	0.125	2.393	1.144	1.127	1.715	1.680	3.725						
	0.010	2.414	1.147	1.140	1.720	1.703							
	0.000	2.467	1.155	1.141	1.732	1.705	3.488						
Rectangular	1.000	1.778			1.553	1.520	2.976	3.8	0.9	0.5	3.7	1.0	0.7
	0.500	1.944			1.600	1.569	3.391	4.8	1.8	1.7	4.5	0.2	0.2
	0.333	2.136					3.956	5.3	1.3	0.9	4.9	0.3	0.2
	0.250	2.279			1.687	1.658	4.439	6.0	1.6	0.9	5.4	0.1	0.1
	0.200	2.384			1.713	1.690							
	0.167	2.463			1.731		5.137	7.0	1.5	0.7	6.1	0.3	0.2
	0.000	3.000	1.234	1.233			7.541	7.9	2.0	2.7	7.9	0.8	0.6
Triangular	1.000	1.644					2.34	4.1	2.5	2.5	4.7	3.7	2.1
	0.866	1.667	1.014		1.520	1.461	2.47	4.0	2.2	1.5	4.0	1.2	0.8

taken from: , Shah and London (1978); , James (1970); , Richardson (1980); ,

Krishnamurty (1967); , Krishnamurty and Sambasiva Rao (1967).

Rao, 1979) reveal that, while in good agreement with the work of James (1970), the model of Rao et al. (1969) can overpredict the data by as much as 40% for $0.07 < E < 0.39$. The agreement between the present theory and literature results (Krisnamurty, 1967; Krisnamurty and Sambasiva Rao, 1967; Shah and London, 1978) for rectangular and triangular geometries is seen to be good. For flat plates, using equations 10 and 18, it may be shown that

$$\mathrm{Nu}_L^{\infty} = (2/3) Re_L^{1/2} Pr^{1/3} \tag{25}$$

in agreement with the analytical solution (Jakob, 1949).

AXISYMMETRIC BODIES : For flow over axisymmetric bodies, the rigorous evaluation of equation 14 is cumbersome. For a sphere, however, using equation 5 and noting that L_f is the semi-circumferential length,

$$L_f = \frac{\pi d_p}{2} \tag{26}$$

in equation 17b, it may be shown that $Gz_G = Pe$. The reduction of Gz_G to Pe is indeed the reason for choosing the form of equation 17b implying that the $Gz_G \to \infty$ condition for conduits corresponds to the $Pe \to \infty$ condition for a sphere and multi-particle systems. Further, for the spherical geometry, equation 18 reduces to

$$Sh_p^{\infty} = Pe^{1/3} \tag{27}$$

Equation 27 is in excellent agreement with the more rigorous solution (Lochiel and Calderbank, 1964; Clift et al., 1978). In Figure 3, the application of equation 18 to spheroids of any aspect ratio is considered. Values of

$$K = \frac{Sh_{spheroid}^{\infty}}{Sh_p^{\infty}} \tag{28}$$

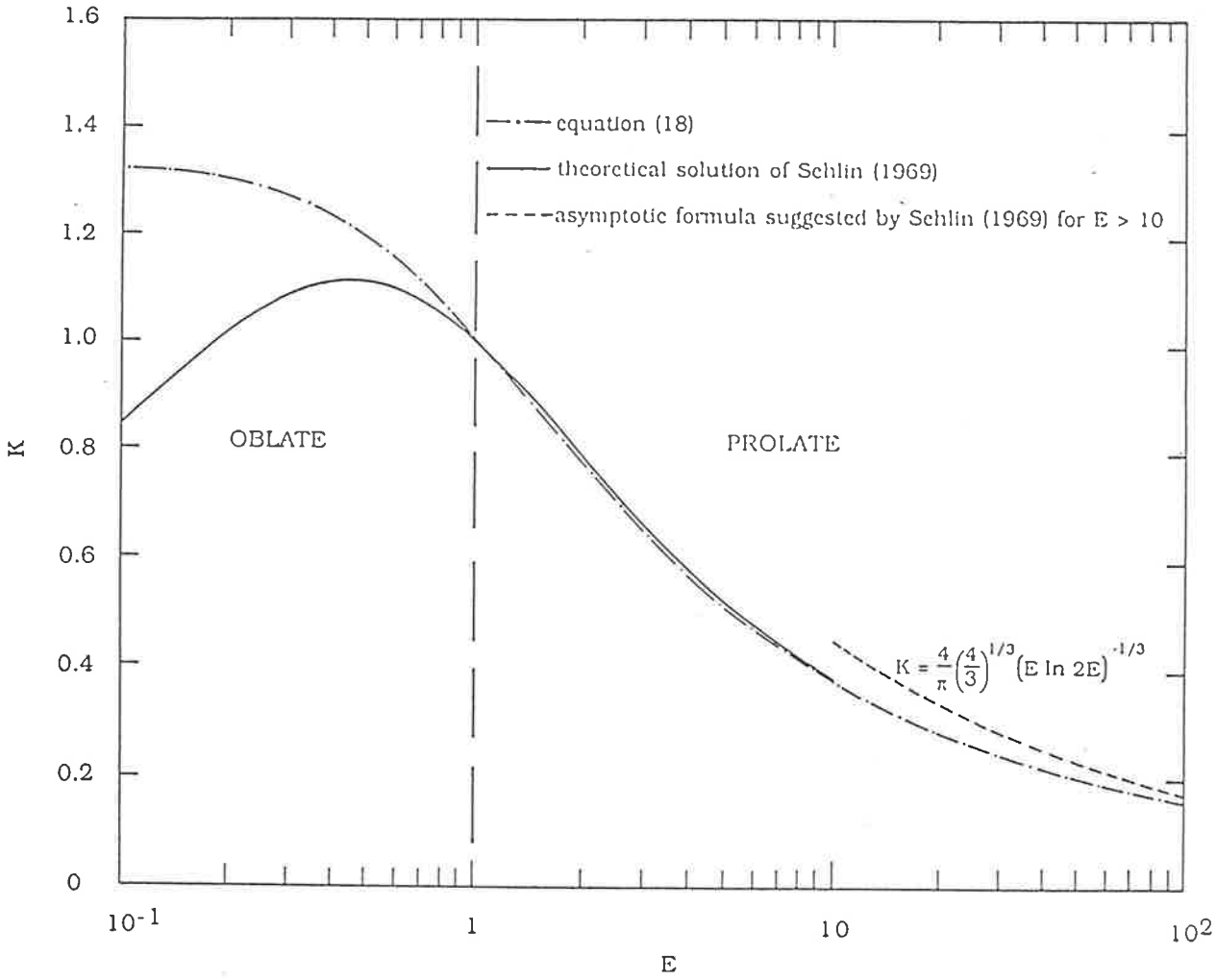

Figure 3 : Viscous Flow Mass Transfer from Spheroids under $Gz_G \rightarrow \infty$ conditions : comparison of equation 28 with the results of Sehlin (1969) as discussed by Clift et al. (1978)

calculated using equations 8, 18 and appropriate semi-circumferential lengths are compared with the detailed calculations reported by Sehlin (1969) as discussed by Clift et al. (1978). The prolate spheroid with the long axis parallel to the flow can be considered as a slender/flat body in the limit of large E. In this region, u_0' would not vary significantly with x, and the conduit solution with $u_0' = \text{constant}$ could become more applicable with increasing aspect ratio. For an oblate spheroid, however, the longer length is perpendicular to the flow and assuming u_0' as invariant with x is not a good representation. Further, the effect of form drag has not been taken into account in obtaining the expression for u_0' (equation 15). The excellent agreement obtained for $E > 0.5$ is then surprising. It seems that for prolate spheroids, the error due to neglecting the form drag is almost perfectly compensated by treating u_0' as constant in equation 14. The computational ease afforded by these results, however, cannot be ignored. These results, obviously, do not extend to the local transfer coefficients.

MULTI-PARTICLE SYSTEMS: To apply equation 18 to multi-particle systems, a suitable measure of L_f must be postulated. Taking into account the presence of stagnant regions (Agarwal and O'Neill, 1988), it is reasonable to expect that the effective flow length around a sphere in the assemblage should be less than that for an isolated sphere (equation 26) by a factor of $(\varepsilon - \varepsilon_b)/\varepsilon$ where ε_b is the stagnant voidage. This term represents the fraction of the void space available for flow. By equating the flow tortuosity, q, in the hydraulic radius model with the fraction of void space available for flow in the submerged object model, Agarwal and O'Neill (1988) obtained $q = \varepsilon/(\varepsilon - \varepsilon_b)$. Consequently, for a multi-particle system,

$$(L_f)_{multi-particle} = \frac{\pi d_p}{2q} \tag{29}$$

Since $q \to 1$ as $\varepsilon \to 1$, equation 29 reduces to equation 26 in the isolated sphere limit. Using equations 16 and 29, and noting that the Stanton number is based on the average approach velocity, $\overline{U} = (U_0 q/\varepsilon)$, it may be shown that

$$Sh_p^{\infty} = 0.695\left(Re_p \frac{q}{\varepsilon}\right)^{2/3}\left(\frac{3}{Re_G}\right)^{1/3} Sc^{1/3} \tag{30}$$

In an earlier paper (Agarwal, 1988), considering an individual particle to be an object submerged in the sphere assemblage and using the boundary layer theory, the following result was obtained

$$Sh_p = K_2\left(Re_p \frac{q}{\varepsilon}\right)^{2/3}\left(\frac{C_{D\varepsilon}}{8}\right)^{1/3} Sc^{1/3} \tag{31a}$$

where $C_{D\varepsilon} = (24q)/Re_\varepsilon$ for the slow flow conditions being considered here. From comparison with experimental data, $K_2 = 0.6$ had been chosen. Subsequently, to model the gas-solid multi-particle systems data for Pe < 10,

$$K_2 = 0.69\frac{((1+Pe)^{1/3} - 1)}{Pe^{1/3}} \tag{31b}$$

has been recommended (Agarwal et al., 1988). Noting that $Re_G = Re_\varepsilon$ for a multi-particle system, it can be verified that equation 30 is in complete agreement with equations 31a-b for high Pe. To model pressure drop in granular media, the submerged object and hydraulic radius approaches have been employed very often (Scheidegger, 1960; Foscolo et al., 1983); the complementary nature of these approaches has been established earlier (Agarwal and O'Neill, 1988). For heat and mass transfer, the use of the hydraulic radius approach - confined to packed bed voidages - has been attempted only very recently (Kawase and Ulbrecht, 1985). The result described in this section is seen as the unification of the submerged object and hydraulic radius approaches for heat/mass transfer in multi-particle systems, at least for low Reynolds and high Peclet number conditions.

In Figure 4, $j_d\{(m/z)/L_f\}^{-1/3}$, is plotted as a function of Re_G. The theory (equation 16) represents detailed solutions for conduits, the flat plate and spheroids with E > 0.5. It may be noted that the mass transfer factor for multi-particle systems is conventionally defined as $(Sh_p/Re_pSc)Sc^{2/3}$. In this paper, the Stanton number is based on the average approach velocity; leading to $j_d = (\varepsilon/q)(Sh_p/Re_pSc)Sc^{2/3}$. Solid-liquid mass transfer data for particulate systems with $0.26 \leq \varepsilon \leq 1$ - the entire range of voidage possible for monosized sphere assemblages - have been plotted in Figure 4 with very good agreement for $Re_G < 10$. As in the case of the generalized drag relation, deviations from equation 16 would occur at critical values of Re_G which depend on the flow geometry.

2.4.3 Analogy between the transport processes

In view of the success of equations 7 and 16 in representing the transfer solutions for various conduit cross-sectional geometries, the flat plate, axisymmetric bodies and the data for multi-particle systems, an analogy between transfer processes was sought. Combining equations 7 and 16, gives

$$j_d = 0.64\,\phi^{1/3}\left\{\frac{\nu}{\overline{U}L_f}\right\}^{1/3} \qquad (32a)$$

or

$$j_d\left\{\frac{m/z}{L_f}\right\}^{-1/3} = 0.51\,\phi^{2/3} \qquad (32b)$$

Equations 32a-b, though identical for the viscous flow regime, have different exponents on the generalized drag factor. It may be pointed out that the form of equation 32a has been used successfully to model heat/mass transfer in multi-particle systems with $Re_p < 10^4$. (Agarwal, 1988; Agarwal et al., 1988).

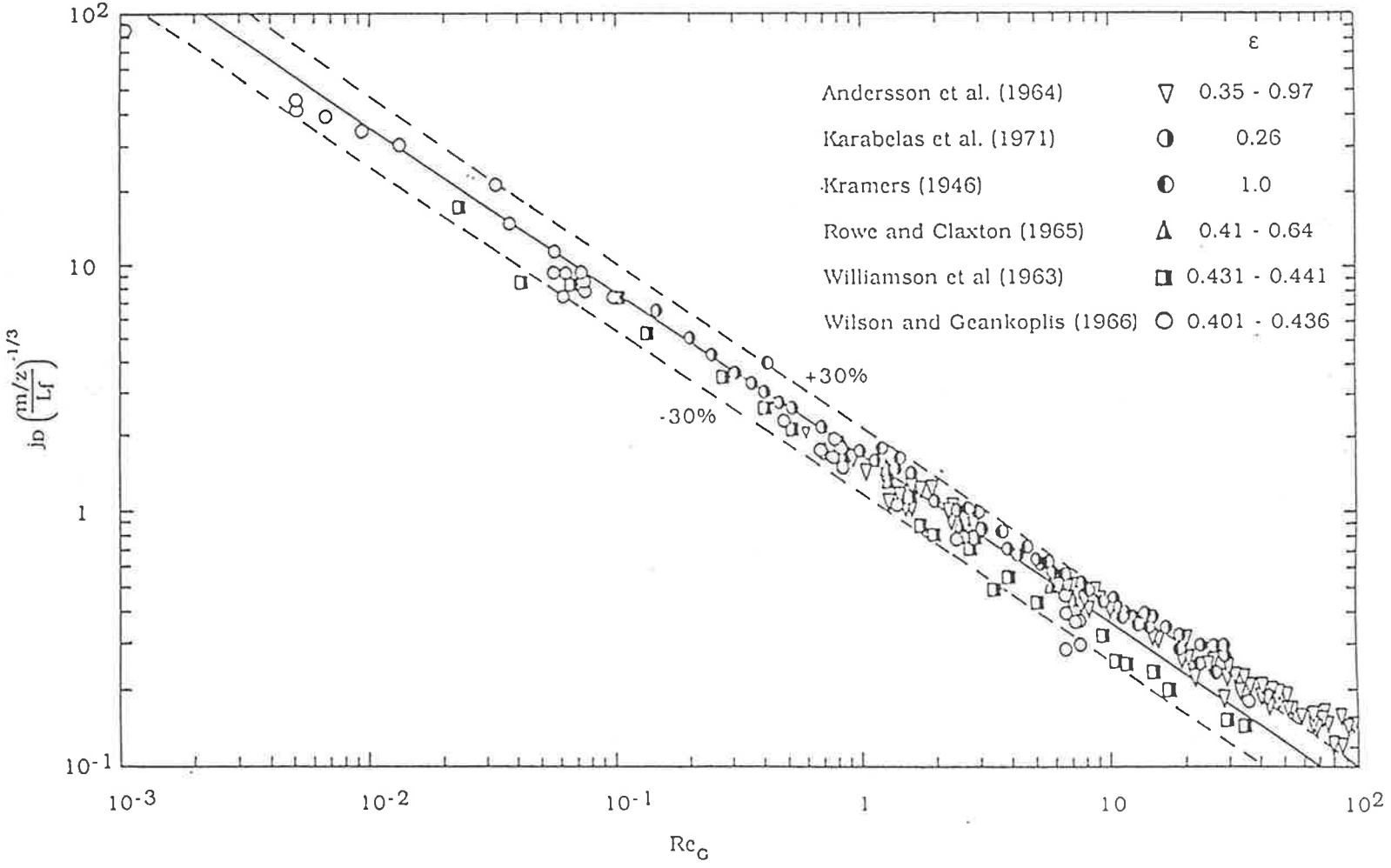

Figure 4 : Viscous Flow Heat/Mass Transfer from Conduits, Spheroids (E > 0.5), Flat Plates and Multi-particle Systems under $Gz_G \rightarrow \infty$ conditions : comparison of equation 16 with multi-particle system data

2.4.4 Heat/Mass Transfer for other Graetz Numbers

The results presented above are applicable only in the thin concentration boundary layer limit. It is of obvious importance to develop simple correlations for the entire range of Graetz numbers. It is known that different geometries have different asymptotic values for the Sherwood (or Nusselt) number in the $Gz_G \to 0$ limit. The relevant asymptotic values for flow and heat transfer in conduits (Shah and London, 1978) have been summarized in Table 6; for axisymmetric bodies, a tabulation has been provided by Clift et al. (1978). A generalization over a wide range of geometries was not possible as these limiting values do not correlate with the cross-section factor, z. However, some encouraging simplifications have been obtained for ducts and are presented in the following.

Clift et al. (1978) have linked the $Pe \to \infty$ solution with the $Pe \to 0$ solution for a sphere using

$$Sh_p = 1 + (1 + Pe)^{1/3} \tag{33}$$

Equation 33 has already been used to obtain the expression for interphase heat/mass transfer in multi-particle systems given by equations 31a-b (Agarwal et al., 1987). Further, in view of the excellent correspondence obtained between the spherical geometry and flow through conduits (equations 18 and 27), this empirical form for ducts was written as

$$\mathrm{Nu}_{G,m} = (\mathrm{Nu}^0_{G,m} - K_3) + (K_3{}^3 + Gz_G)^{1/3} \tag{34a}$$

Equation 34a may be rearranged to

$$\mathrm{Nu}_{d_h,m} = \left(\mathrm{Nu}^0_{d_h,m} - K_4\right) + \left(K_4{}^3 + \mathrm{Nu}^{\infty}_{d_h,m}{}^3\right)^{1/3} \tag{34b}$$

where $K_4 = (4z/3)K_3$. A similar expression may also be chosen for the peripheral average Sherwood number,

$$\mathrm{Nu}_{d_h,x} = \left(\mathrm{Nu}^{0}_{d_h,x} - K_5\right) + \left(K_5{}^3 + \mathrm{Nu}^{\infty}_{d_h,x}{}^3\right)^{1/3} \qquad (34c)$$

Values of K_4 and K_5, determined by fitting the numerical tabulations compiled by Shah and London (1978) for different conduit geometries, are included along with the resulting average error and standard deviation in Table 6 (page 28). It may be noted that in several cases the range of Graetz numbers for which numerical computations have been reported is somewhat limited. Though the agreement is excellent (model and literature data are tabulated in Appendix C), the values of K_4 and K_5 do not appear to correlate with z or with the asymptotic Nusselt number. However, the simplicity of these one-parameter forms is appealing in comparison with correlations available previously (Churchill and Ozoe, 1973; Shah and London, 1978). The highest standard deviation is observed for the right angled isoceles triangular ducts; however, this is not surprising in view of the low body curvature assumption (Appendix B) being invalid at the 45° vertices.

2.5 CONCLUSIONS

The proposed definition for the Reynolds number permits the formulation of a general drag curve which is applicable for a wide range of geometries under viscous flow conditions. The use of this drag relation in the thin concentration/ thermal boundary layer equations yields a solution for the heat/mass transfer factor which is strictly applicable for flat plates and conduits. This solution also provides excellent agreement with the available theoretical results for spheroids for $E > 0.5$. This is thought to occur because the error in neglecting the effects of form drag is compensated for by treating the surface average velocity gradient as constant. The conduit solution, with appropriate transformations, also applies to interphase heat/mass transfer in assemblages of multi-particle systems. The expression obtained is identical to the equation developed earlier based on a submerged object model. The agreement over such a wide range of flow geometries enables the formulation of an analogy between transport phenomena for viscous flow under the $Gz_G \to \infty$ conditions. Though the interphase transport phenomena for different flow geometries follow common curves in the viscous flow regime, deviations occur at critical values of Re_G - due to turbulence or increased inertial contribution - which still depend on the flow geometry. Extension of the approach to cover the entire range of Gz_G, though not entirely generalized, can be used to obtain simple one-parameter empirical correlations for surface and peripheral average interphase heat/mass transfer coefficients in conduits.

CHAPTER III

ACTIVE PARTICLE MOTION IN THE EMULSION PHASE OF A FLUIDIZED BED

3.1 INTRODUCTION

3.1.1 Background

When a fluid is passed upward through a bed of uniform particles at such a velocity that the upwards fluid drag force acting on the particles becomes equal to the downward weight of the particles, the particles will become suspended in the fluid. This is the onset of fluidization and the velocity at which this occurs is the minimum fluidization velocity, U_{mf}.

If the fluidizing fluid is a liquid, the bed will expand homogeneously as the velocity is increased above U_{mf}, so that the emulsion (or particle rich) phase porosity, ε, increases. Although there is no bulk convective movement of solids within the bed, particles are observed to move about in a random manner (that is, a diffusive solids mixing mechanism exists).

When a gas is used, bubbles or 'pockets' of gas form in the bed at superficial velocities greater than U_{mf}, allowing the gas to pass through the bed either through the bubbles or through the emulsion phase. Bed expansion, as the superficial velocity is increased, results primarily from the increase in the size of

bubbles in the bed. The emulsion phase remains essentially at ε_{mf}, the porosity at minimum fluidization conditions, for Group B and D powders (Geldart, 1973; Valenzuela and Glicksman, 1985). As a bubble rises in the bed, a wake of solids at its base is carried up. So, to maintain steady state conditions, there must be a net convective velocity of solids, U_D, downwards in the emulsion phase. An expression for this velocity has been determined by a mass balance on solids (Kunii and Levenspiel, 1969).

When an active particle of a different size and density to the inert particles that make up the bed is added to the emulsion phase of the bed, a movement that is distinct from that of the inert bed material results. This segregation, or classification, process is caused primarily by the density difference between the particles but size difference can also cause it.

For example, if a sufficiently heavy particle is added to a liquid fluidized bed of inert particles, the active particle will sink through the emulsion to the bottom of the bed and will probably stay there (called a jetsam particle). Likewise a sufficiently light particle will float to the top and stay there (called a flotsam particle). Note that the mechanism for mixing in liquid beds, namely random motion of the particles, is small and will probably be insufficient to move the active particle back into the bed bulk.

However, the mixing process that results from bubble motion in a gas fluidized bed is considerably more significant when compared to the segregation process that occurs in the emulsion phase. A sufficiently heavy particle will move down in the emulsion phase to the bottom of the bed (as in liquid beds),

however, the particle may be swept into the wake of a passing bubble and lifted back upwards into the bed bulk. A sufficiently light active particle that moves upwards with respect to the inert emulsion particles, may still move downwards in relation to the container walls, if the rise velocity of the active particle with respect to the emulsion is less than the bubble-induced emulsion phase velocity, U_D, downwards. Once again, the active particle is swept upwards by being picked up by a passing bubble wake. Consequently, if mixing of the active particle within the gas fluidized bed is to occur, then it must move downwards with respect to the container walls whilst in the emulsion phase. The particle will always move upwards in the bubble phase.

3.1.2 Objectives

The main objectives of this study are to:

1) develop an expression, that is applicable to both gas and liquid fluidized beds, for the emulsion phase segregation velocity of the active particle from first principles;

2) develop criteria (necessary and sufficient conditions) that determine, from the properties of the fluidized system, whether the active particle will float, sink or mix in a particulate (no bubbles) as well as a bubbling fluidized bed;

and 3) test the predictions that result from 1 and 2 above with data available in the literature and with data determined from experiments performed by the author.

It should be pointed out that this study is applicable only when there are relatively few active particles fluidized along with the inert bed material, that is,

less than ten percent by volume. Consequently, the bulk bed properties such as U_{mf} and bed porosity, ε, can be assumed to be dependent on the inert particle properties only.

3.1.3 Why Bother? :Applications for the Study

Both liquid fluidized beds and incipiently fluidized gas beds (that is, the fluidizing velocity is at U_{mf}) can be used as classification devices to separate particles with a sufficient difference in either size or density, since there will be no significant mixing mechanism that opposes the desired segregation process in these configurations (section 2.1.1). The removal of loose solid impurities from a valuable ore or mineral, such as stone dusts from coal (Daniels, 1961), is an example of such a process. It is obvious that the design of these classifiers would be improved if an expression for this segregation rate was available during the design process.

As mentioned in Chapter 1, the fluidized bed combustion of coal was the initial motivation for this work. This process involves burning coal particles in a hot air fluidized bed of inert limestone particles that are both heavier and smaller than the active coal particles. As expected, the combustion rate of the coal within the bed is an important design parameter. This rate is directly related to the mass transfer rate of oxygen to the particle surface. Whilst in the emulsion phase, the convective mass transport coefficient that governs this transfer rate is influenced by the relative velocity between the interstitial air and the active coal particle. Consequently, any accurate modelling study of the reaction and mass transfer rates requires knowledge of the coal particle velocity. It is also important that the coal particle resides in the bed bulk: one of the reasons being that SO_x generated

by the combustion process can then be removed in situ by reaction with the limestone particles. Being able to predict, therefore, whether the coal particle will float or mix within the bed will also be important in the design process.

3.2 LITERATURE SURVEY

3.2.1 Segregation Studies in Liquid Fluidized Beds

BINARY MIXTURES - general: In liquid fluidized beds of binary particles that differ in size and/or density, segregation will occur to produce two separate particle layers: one of jetsam particles at the bottom of the bed and the other of flotsam particles at the top. The diffusion or mixing process (due to the particles random motion) produces an interfacial region that contains a fraction of both particles. The size of this region will depend on the relative magnitudes of the mixing and segregation processes. To determine these characteristics Kennedy and Bretton (1964) expressed the mixing process in terms of a one-dimensional diffusive flux and the segregation process in terms of a convective flux based on a segregation velocity (details of this velocity are presented in the next section). Steady state concentration profiles of the jetsam within the bed were obtained by equating these fluxes. This model remains the most widely used for mixing and segregation in particulate beds; its limitations have been discussed recently (Gibilaro et al., 1985).

SEGREGATION VELOCITY: The segregation process in liquid fluidized beds has been modelled primarily from hydrodynamic considerations, and only the steady state or terminal segregation velocity appears to have been considered.

Prudhoe and Whitmore (1964) reported terminal velocity data for various heavy spheres falling through oil fluidized beds of glass beads in an attempt to determine the effective viscosity of a fluidized bed. The highly viscous oil ensured that inertial fluid drag effects could be neglected. Only two fluid velocities were considered. The modelling study assumed that the falling sphere

shears a suspension of viscosity, $\overline{\mu_s}$, and that Stokes law holds. The sphere was also assumed to displace the suspension so that the buoyancy force was proportional to the suspension density, $\overline{\rho_s}$. To account for the influence of the upward flow of fluidizing liquid on the terminal velocity it was assumed that

$$U_a - V_u = U_a' \tag{35}$$

where U_a is the true terminal velocity of the sphere, U_a' is the terminal velocity that would result if the sphere was falling through a stagnant suspension and V_u the effective upward velocity of fluid within the bed. An additional empirical correction factor had to be added to the model expression so that the predicted effective viscosity, $\overline{\mu_s}$, determined from fitting their own terminal velocity data, would not have an apparent active particle diameter dependence.

Kennedy and Bretton (1966) in their mixing/segregation model for a particulate fluidized bed (as mentioned in the previous section) used an intuitive argument to obtain an expression for the segregation velocity in a bed of porosity, ε, as

$$U_a = \frac{(U_0)_a - (U_0)_i}{\varepsilon} \tag{36}$$

where $(U_0)_a$ is the fluid velocity required to fluidize a bed of only active spheres to a porosity ε, and $(U_0)_i$ is, likewise, the velocity required to fluidize a bed of only inert spheres to the same porosity. The primary forces assumed to act on a segregating particle in this analysis are, therefore, fluid drag, gravity and buoyancy since the fluidizing velocity (upon which equation 36 is based) is determined solely by equating these forces. No direct attempt at verification of the model by comparison with experiment was made.

Martin et al. (1981) measured the terminal velocity of heavy ion exchange beads falling through a water fluidized bed of lighter beads and investigated the dependence of this velocity on the fluidizing velocity. The segregation velocity predicted from equation 36 was poor in comparison with their experimental data; it would overpredict the velocity at low porosities and underpredict at medium to high porosities. Hence, a modification to the Kennedy and Bretton expression was proposed and an empirical fit to the data gave

$$U_a = 2.5\frac{(U_\infty)_a - (U_\infty)_i}{(U_\infty)_i}(U_0 - U_{mf}) \tag{37}$$

where U_∞ is the terminal velocity of an isolated particle (i = inert, a = active) in an infinite fluid. The agreement between model and experiment for $\varepsilon > 0.8$, however, was still poor.

In his review paper on solid-liquid fluidization, Joshi (1983) used the concept of a turbulence intensity to account for the increase in fluid drag on a particle when it is placed in a multi-particle system. By equating this upwards fluid drag force with the gravity force and the buoyancy force (which was assumed proportional to the volume of liquid displaced), an expression for the segregation velocity of an active particle was obtained. In the laminar flow region, this expression was

$$U_a = (U_\infty)_a\left(\frac{(1-R_D)^2}{1-R_D^2}\right) - \frac{U_0}{\varepsilon} \tag{38a}$$

where

$$R_D = \left(1 + \frac{2}{3}\frac{\varepsilon}{(1-\varepsilon)}\frac{d_i}{d_a}\right)^{-1/2} \tag{38b}$$

It is interesting to note the explicit dependence on the inert particle diameter, d_i. Agreement with the laminar regime data of Prudhoe and Whitmore (1964) was claimed to be good. On closer inspection, however, it is apparent that the comparison involved only a small amount of data points in the low segregation velocity range (up to 13 mm/s) out of a possible range up to 50 mm/s (Figure 9 in Joshi, 1983). A more detailed comparison with the Prudhoe and Whitmore data is given in Figure 5. The fit is good, as claimed, in the low velocity region but can be seen to be poor at higher velocities. It was also reported that the Kennedy and Bretton (1966) and the Martin et al. (1981) models (equations 36 and 37 respectively) could not correlate the Prudhoe and Whitmore data.

3.2.2 Segregation Studies in Gas Fluidized Beds

BINARY SYSTEMS - general: The mixing process in bubbling gas fluidized beds has considerably more influence on the segregation process than that in liquid or particulate fluidized beds discussed in the previous section, simply because of the bulk convective velocity of solids within the bed induced by the bubbles. Consequently, both the competing mixing and segregation mechanisms in gas fluidized beds of binary mixtures are important in any analysis of segregation.

The majority of work in this area has originated from Rowe, Nienow and co-workers at University College, London. The salient aspects of their work are presented in the following.

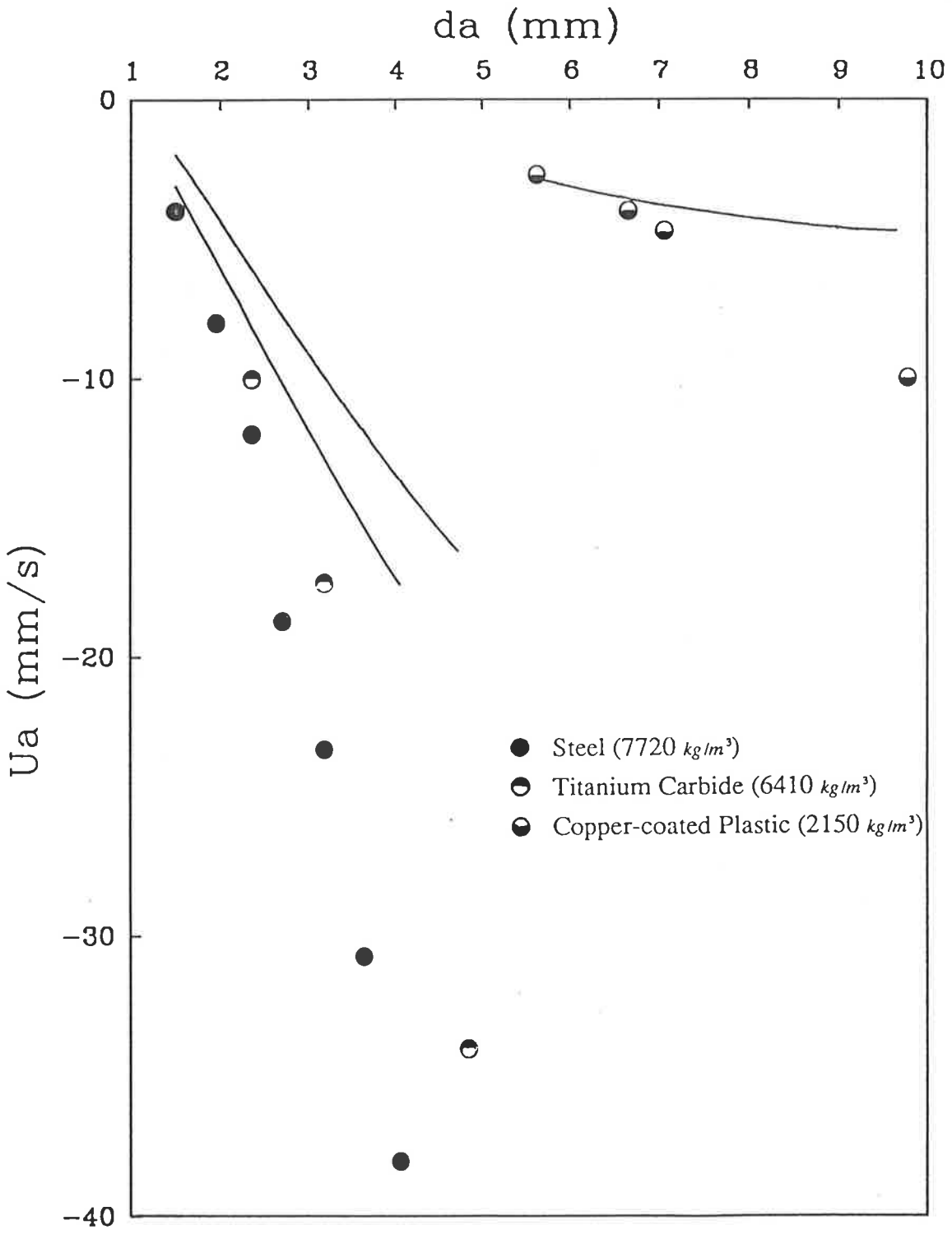

Figure 5 : Terminal Segregation Velocities of Heavy Active Particles falling through a Liquid Fluidized Bed of Glass Ballotini : comparison of Joshi (1983) model (equation 38) with the data of Prudhoe and Whitmore (1964)

Rowe et al. (1972), in a qualitative analysis of their segregation experiments in gas fluidized beds of binary mixtures, concluded that the primary mechanisms for segregation are:

1) the lifting of particles in the enclosed wake of passing bubbles (this may aid segregation but is more often associated with mixing);

2) the falling of large, dense particles (jetsam) through bubbles to descend through the bed;

3) the falling of jetsam, with respect to the flotsam, in those regions of the emulsion phase recently disturbed by a rising bubble;

and 4) the quasi-hydrostatic effect that causes light particles at the top to remain there (that is, flotsam). Under no circumstances were these light particles found to sink into the bed.

If the powders that make up the mixture differ in density, the denser becomes the jetsam; if they differ in size, it is the larger that settles to the bottom.

The first model to determine the steady state concentrations within the segregating gas fluidized bed was presented by Gibilaro and Rowe (1974). The bed was assumed to consist of two phases; a bulk or emulsion phase and a wake phase which travels upwards with the bubbles. Four adjustable parameters were defined to describe the three possible modes of mixing (namely, bulk circulation, exchange between the phases and axial diffusion) and the one of segregation, which was assumed to occur only in the bulk phase. The model was applicable only to those cases where the jetsam fraction in the bed is less than 50% by volume.

Naimer et al. (1982) expressed the adjustable parameters in the Gibilaro and Rowe model in terms of the system properties, thus allowing the parameters to be estimated from first priciples. The axial mixing effect was neglected. The segregation rate parameter was related to the bed and bubble properties by using the correlation of Tanimoto et al. (1981) which is outlined in the next section.

Chiba et al. (1980) presented experimental data which show that the denser particles, under some conditions, may be flotsam in contradiction with previous observations (Rowe et al., 1972).

When the jetsam fraction is greater than 90% by volume, the segregation patterns observed were distinctly different from those in low jetsam fraction systems. An additional overlayering mechanism was assumed to exist, which can cause flotsam particles at the top of the bed to sink back into the bed bulk (Nienow et al., 1978a). For the case of a few large active particles in a jetsam rich bed (as in the fluidized bed combustion of coal), Nienow et al. (1978b) found that the large flotsam particle would float at gas velocities little in excess of U_{mf}. However, at quite moderate bubbling rates, it would be constantly drawn beneath the surface by overlayering or downwards convective flow of the jetsam. The flotsam particles would move back upwards by short rides in passing bubbles.

SEGREGATION VELOCITY: As for the corresponding studies in liquid beds, most of the models in the literature determine the steady state segregation velocities only. They are mainly based on a mass balance approach which effectively makes them inapplicable to a single active particle analysis.

Gibilaro and Rowe (1974) expressed the segregation rate as an overtaking downward velocity of the jetsam particles with respect to the flotsam particles. It was assumed that the segregation occuring at a point was proportional to the concentration of jetsam at that point. Solids balance over a volume element of the bulk phase revealed that

$$\frac{dU_a}{dl} = k_s (1 - 2x_J) \frac{dx_J}{dl} \tag{39}$$

where U_a is the segregation velocity of jetsam in the bulk phase at a height, l, x_J is the jetsam fraction and k_s is an adjustable segregation factor that is assumed to be constant throughout the bed.

Tanimoto et al. (1981), as suggested by Rowe et al. (1972), considered segregation between the jetsam and the flotsam particles to be possible only in the drift produced by a passing bubble. The relative displacement between the two particles, $\bar{y}$, was measured under different experimental conditions and empirically correlated as

$$\bar{y} = 0.3\overline{d_b} \left(\frac{\rho_J}{\rho_F} \right) \left(\frac{d_J}{d_F} \right)^{1/3} \tag{40}$$

$\overline{d_b}$ is the bubble diameter and the J and F subscripts refer to the jetsam and flotsam fractions respectively. Note that if U_0 equals U_{mf}, so that $\overline{d_b}$ is zero, equation 40 predicts no relative motion between the particles.

Using the the above correlation for segregation displacement, Naimer et al. (1982) derived an expression for the segregation factor, k_s, in equation 39 in terms of the bubble and particle properties

$$k_s = \frac{3}{2} \frac{\bar{y}}{\overline{d_b}} \frac{\varepsilon_b}{1 - \varepsilon_b} U_b \tag{41}$$

where U_b is the bubble rise velocity and ε_b is the fraction of the bubble phase (including the wake phase) in the bed.

Beeckmans et al. (1985) found that the relative settling velocity between magnetite particles (ρ_J = 4500 kg/m^3, d_J = 170 μm) and sand particles (ρ_F = 2650 kg/m^3, d_F = 232 μm) in a gas fluidized bed that contained 2% magnetite particles (by volume) was approximately 3.2 mm/s. The gas velocity used was twice the bed minimum fluidization velocity. An expression for this segregation velocity was obtained by using the solids balance approach, used firstly by Kunii and Levenspiel (1969) to determine the bulk convective velocity, U_D, in a uniform particle fluidized bed, to give

$$U_a = \frac{\alpha(U_0 - U_{mf})((x_J)_w - (x_J)_b)}{(x_J)_b(1-(x_J)_b)(1-\varepsilon_b - \alpha\varepsilon_b)} \tag{42}$$

The ratio of wake volume to the bubble volume is α, and the w and b subscripts denote the wake and bulk/emulsion phases respectively.

As part of a study on the drag force on spheres moving through particulate gas fluidized beds, Daniels (1962) measured the terminal velocity of metallic particles falling through a fluidized bed of sand particles. It is interesting to note that these results indicate that segregation occurs in the emulsion phase without the presence of bubbles.

3.2.3 Forces that act on a Particle in a Fluidized Bed

It is apparent from the previous sections that a satisfactory hydrodynamic model for the segregation velocity is still required. To achieve this goal, the relevant forces acting on a particle while in the emulsion phase must be both

identified and quantified.

FLUID DRAG FORCE: Pressure drop resulting from the drag resistance to fluid flow through assemblages of particles has received wide research attention over the past fifty years. Flow through the medium has been modelled as that through a collection of equivalent tubes (hydraulic radius models) or as that over a collection of individual particles (submerged object models). Limitations to both models have been discussed already in section 2.2 in the last chapter.

The most widely used hydraulic radius model for pressure loss results from Ergun (1952)

$$\frac{\Delta P}{L} = 36C_1\frac{(1-\varepsilon)^2\mu}{\varepsilon^3 d_p^2}U_0 + C_2\frac{(1-\varepsilon)\rho}{\varepsilon^3 d_p}U_0^2 \qquad (43)$$

where C_1 is the Kozeny factor (Carman, 1956) and C_2 is an inertial drag factor. For packed beds, C_1 = 150/36 and C_2 = 1.75 were used. This model is applicable to low bed porosities, $0.4 < \varepsilon < 0.6$, and $Re_p < 2000$. The submerged object has been used to predict the pressure loss behaviour at higher porosities ($\varepsilon > 0.8$).

As mentioned in Section 2.2, Andersson (1961) extended the hydraulic radius approach to high bed porosities by using the cross-section factor, z, to account for the variation of the flow channel cross-section geometry with porosity. This allowed him to write

$$\frac{\Delta P}{L} = 36zq^2\frac{(1-\varepsilon)^2\mu}{\varepsilon^3 d_p^2}U_0 + 6C_i\frac{(1-\varepsilon)\rho}{\varepsilon^3 d_p}U_0^2 \qquad (44)$$

where zq^2 is a modified Kozeny factor, q is the tortuosity factor and C_i (= $C_{D_\infty} - 24/Re_{p,\infty}$) is an inertial drag coefficient. The first term on the right side of

equation 44 represents the viscous drag and was used in the viscous flow analysis presented in Chapter 2 (equation 4).

Foscolo et al. (1983), in determining the expansion characteristics of particulate fluidized beds from the packed bed state to the isolated particle regime, modified the Ergun hydraulic radius model (equation 43) by the inclusion of a tortuosity factor (equal to $1/\varepsilon$) in the viscous term and a porosity dependent inertial drag factor in the inertial term. This modified form was assumed to be applicable over the complete voidage range. The fluid drag on a particle within the suspension was then obtained from the modified Ergun equation by implicitly assuming that the buoyancy force acting on the the particle will be proportional to the suspension density. Extension to the isolated particle regime ($\varepsilon \rightarrow 1$) was possible only after the force on a single particle was added to the force balance. Verification of the model was achieved by comparing the expansion predictions of the model with the Richardson and Zaki correlation (1954). Agreement in the intermediate flow regime ($0.2 < Re_{\infty} < 500$) was poor due to the interpolatory nature (between the viscous and inertial flow regimes) assumed by the Ergun expression.

A combination of the submerged object and hydraulic radius approaches was also used by Agarwal and O'Neill (1988) in their formulation of a model for the porosity dependent drag force. The Andersson hydraulic radius expression (equation 44) was used since it already was applicable over a wide range of porosity. It should be pointed out that, as for the development of Foscolo et al. (1983), the combination of the two approaches was achieved assuming that the

buoyancy force results from the displacement of the suspension as a whole and not just the interstitial fluid. Separate functions for the three parameters in the Andersson equation, namely z, q and C_i were developed.

PARTICLE-PARTICLE INTERACTION FORCE: When a body moves relative to a suspension of particles then the suspension as a whole will be sheared and a shear force opposing the motion will result. This force is produced by fluid and particle interactions, both with the shear boundary and within the suspension bulk itself (Cheng, 1980b).

For dilute gas-solid flows (as in pneumatic transport), the importance of this force has been recognised. Arastoopour et al. (1980) (as discussed by Arastoopour et al., 1982) concluded that, although pressure drops over a pneumatic transport line carrying a binary solids mixture were predicted well by a hydrodynamic model, the calculated degree of segregation would deviate significantly from experiment. The deviation was ascribed to the neglect of a binary collision force in the model. Doss (1985), as discussed by Srinivasan and Doss (1985), came to the same conclusion. He found that inclusion of a particle interaction force in the particle momentum balance produced a better fit to his experimental data obtained from multi-particle solids/gas flows in a variable area duct.

For more concentrated suspensions of fluid and solid, the particle momentum balance approach becomes less valid. However, a considerable amount of work has been done in characterizing this force in terms of an effective suspension shear viscosity, $\overline{\mu}$.

(i) Liquid Suspensions:

Theoretically, the viscosity of suspensions, $\overline{\mu_s}$, of neutrally buoyant spheres can be determined from either the velocity gradient

$$\tau_{jk} = -\overline{\mu_s}\left(\frac{\partial U_j}{\partial l_k} + \frac{\partial U_k}{\partial l_j}\right) \tag{45}$$

or from the energy dissipation due to shearing, E_d as

$$E_d = -\overline{\mu_s}\int_V \frac{\partial U_j}{\partial l_k}\left(\frac{\partial U_j}{\partial l_k} + \frac{\partial U_k}{\partial l_j}\right)dV \tag{46}$$

The many theoretical and semi-theoretical approaches used in the literature have been reviewed by Jinescu (1974), the salient points of which are presented in the following.

Einstein (1906) published the first work on suspension viscosity. He accounted for longe range interactions between fluid and particles and found

$$\frac{\overline{\mu_s}}{\mu} = 1 + 2.5\phi_s \tag{47}$$

This equation is only applicable for solid volume fractions, ϕ_s, of less than ten percent. With more concentrated suspensions it is necessary to account for more complex interactions. The viscosity-concentration relation becomes non-linear; the rate of increase of viscosity accelerating as concentration increases (Cheng, 1980a). Many of the existing theoretical and empirical equations for this concentration region have been expressed as a power series in the solids concentration, ϕ_s. Alternatively, models for $\overline{\mu_s}$ have been proposed which give the viscosity-concentration relation in a closed form. For example, Thomas (1965) proposed the function

$$\frac{\overline{\mu_s}}{\mu} = 1 + 2.5\phi_s + 10.05\phi_s^2 + 0.00273\exp(16.6\phi_s) \tag{48}$$

where the ϕ_s term accounts for long distance interactions, the ϕ_s^2 term for particle collisions, doublet rotations and the rolling of doublet spheres one over the other, and the exponential term accounts for the rearrangement of particles, as the suspension is sheared, from one shear plane to another. The experimental results of thirteen investigators were correlated to within twelve percent for $\phi_s < 0.5$. Frankel and Acrivos (1967) theoretically determined, for high concentrations,

$$\frac{\overline{\mu_s}}{\mu} = 1 + \frac{9}{8}\frac{(\phi_s/(\phi_s)_{max})^{1/3}}{1-(\phi_s/(\phi_s)_{max})^{1/3}} \tag{49}$$

where $(\phi_s)_{max}$ is the maximum attainable concentration for a more or less compact arrangement of the solids. For example, $(\phi_s)_{max}$ is 0.26 for the most compact arrangement - the hexagonal lattice.

In conclusion, Jinescu (1974) stated that the collected theoretical and experimental results for the suspension viscosity remain inconclusive. As a first approximation, the model of Thomas (1965) (equation 47) was recommended.

Cheng (1980a), summarizing the work on viscosity-concentration equations for suspensions, concluded that the studies done up to 1980 are still inconclusive and that no correlation or model could be singled out as being superior.

More recently, Kawase and Ulbrecht (1983) proposed a correlation for the viscosity of suspensions of solid spheres in power law liquids. Starting from a cell model they obtained (only the Newtonian fluid solution is given here)

$$\frac{\overline{\mu_s}}{\mu} = \frac{1+8.203\phi_s^5}{1-2.478\phi_s+18.456\phi_s^5-20.326\phi_s^6} \tag{50}$$

This relation was in good agreement with the extensive experimental data of

Rutgers (1962).

Comparison of this model with the model of Thomas (equation 48) is given in Figure 6. For $\varepsilon > 0.7$ or $\phi_s < 0.3$, the predictions of the two models are close but significant deviation occurs at higher solid fractions.

It must be made clear at this point that the definition of the effective suspension viscosity, $\overline{\mu}_s$, given in equations 45 and 46 does not include those effective viscosities of Hawksley (1951) and Barnea and Mizrahi (1973). In the first case, the viscosity represents the suspension as a whole and is measured by viscometers. In the second case, the calculated viscosity is that experienced by the fluid only and is used in calculating the porosity dependent fluid drag on the suspended particles.

(ii) Gas Suspensions:

A gas-solid suspension can only be produced when the particles are fluidized by an upward flow of gas since the large density difference makes it impossible to have neutrally buoyant particles. It should be noted that, unlike solid-fluid suspensions which can have variable solid fractions, the emulsion or particle rich phase in a gas fluidized suspension remains essentially at the minimum fluidization porosity, ε_{mf}, even under bubbling conditions. Moreover, the effective viscosity is much higher than that obtained for liquid-solid systems at the same voidage (Saxton et al., 1970) due to the higher internal friction amongst the dry particles (that is, the particle surface is not wetted by liquid).

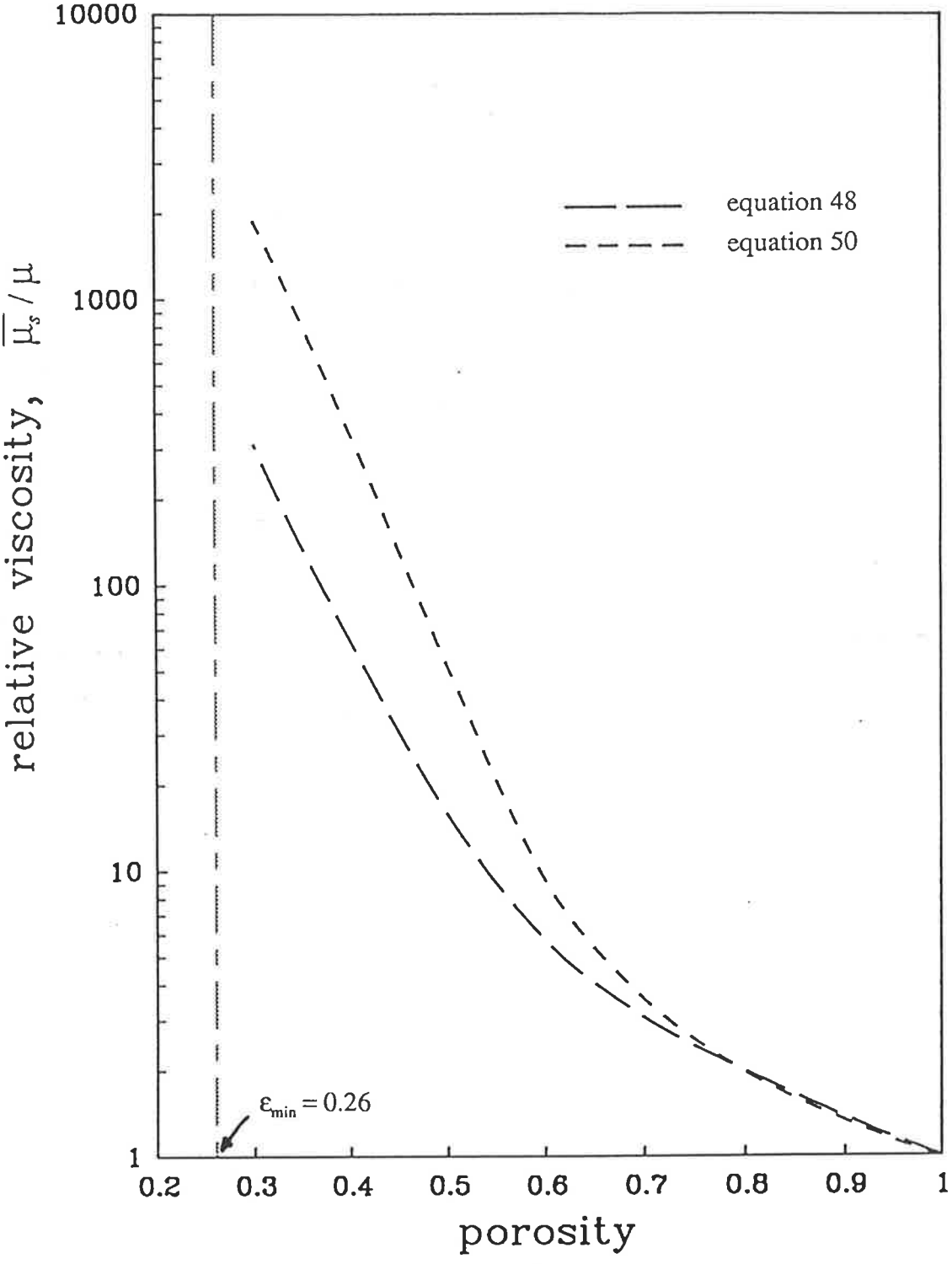

Figure 6 : Comparison of the Suspension Viscosity Correlations of Thomas (1965) (equation 48) and Kawase and Ulbrecht (1985) (equation 50)

The experimental methods that have been used to determine the emulsion phase (or suspension) viscosity fall into two categories

1) Techniques commonly used to determine the viscosity of Newtonian fluids.

Schugerl et al. (1961) and Hagyard and Sacerdote (1966) used a rotating cylinder viscometer to measure $\overline{\mu_s}$. Care was taken to ensure that the fastest rotation of the body was slow compared with the fluidizing velocity, thus minimizing bed disturbance. Daniels (1962) and King et al. (1985) used the falling sphere technique. A problem with these methods is that the local state of fluidization is disturbed.

2) Indirect methods based on the behaviour of bubbles in the fluidized bed.

This method allows the effective viscosity to be determined from bubble properties, thereby removing problems that arise from external measurement disturbances.

Murray (1967) inferred $\overline{\mu_s}$ from his estimates on the viscous drag coefficient for the rising bubbles. However, the resulting expression for the viscosity was found to be dependent on the bubble diameter. Stewart (1968) obtained values of $\overline{\mu_s}$ from the difference between predicted and observed pressure measurements as a bubble passed a probe. Grace (1970) estimated the viscosity from the shape of a bubble by comparing the fluidized bed bubble wake angle with those of bubbles rising in a liquid of known viscosity.

Table 7 summarizes the data of the various investigators.

TABLE 7

Experimental Suspension Viscosities, $\overline{\mu_s}$, for Gas-Solid Fluidized Beds

Reference	Particle Type	Particle Size (μm)	Suspension Viscosity $\overline{\mu_s}$ (Pa.s)
Schurgel (1961)	sharp edged quartz and silicon carbide	200 - 350	0.5 - 1.0
	smooth glass and polystyrol beads	200 - 350	0.1 - 0.5
Daniels (1962) (see section 3.5.1)	coarse sand	114	1.7
Stewart (1968)	silver sand	500	< 2.5
	magnesite	240	< 1.5
Grace (1970)	glass ballotini	60 - 550	0.4 - 1.2
	silver sand	72 - 500	0.5 - 1.4
	synclyst catalyst	52	0.4
	magnesite	240	0.9
King et al. (1985)	glass ballotini	64 - 475	0.25 - 2.2

EFFECTIVE WEIGHT FORCE: The effective weight of a particle, W_e, in a fluidized suspension is given by

$$W_e = W_b - \rho_a V_a g \qquad (51a)$$

where W_b is the buoyancy force on the submerged active particle of volume V_a and density ρ_a.

The buoyancy force acting on a particle has traditionally been described in terms of the density of the fluid alone (Wen and Yu, 1966; Kunii and Levenspiel, 1969) by

$$W_b = \rho V_a g \qquad (51b)$$

Other workers have, however, indicated that it should be described based on the density of the suspension which is a blend of fluid and solid (Richardson and Meikle, 1961; Reitema, 1982; Foscolo et al., 1983; Agarwal and O'Neill, 1988) as

$$W_b = \overline{\rho_s} V_a g \qquad (51c)$$

where $\overline{\rho_s} = \varepsilon\rho + (1-\varepsilon)\rho_i$ is the suspension density.

Recently, arguments have been put forward for both cases (Epstein, 1984; Gibilaro et al., 1984; Clift et al., 1987; Gibilaro et al., 1987). However, the problem has still not been resolved.

3.3 EXPERIMENTAL SYSTEM

Experiments to test the developed model (as outlined in the next section) were performed in a liquid fluidized bed using light active particles that rose in the bed of heavier inert particles.

3.3.1 Apparatus

The liquid fluidized bed system used is shown in Figure 7a. The column was made of perspex with a diameter of 150 mm and a height of approximately 500 mm. Distilled water (the fluidizing liquid) entered the bottom of the column through a calming section that controlled the water velocity profile to eliminate channelling before passing through a sintered bronze distributor plate into the fluidizing section. Glass ballotini (size range: -425 +250 μm; $\rho_i = 2470 kg/m^3$) was used as the inert bed material and the active particles were made from acrylic spheres.

The water flow rate was measured by one of three rotameters. Each meter was calibrated for flow over the low, middle and high flow regions to cover all the flow rates tested with good accuracy. The bed porosity was inferred from pressure readings made by a manometer tube inserted into the bed.

To insert and release the active particles within the bed, a simple sampler apparatus using a thin plastic tube (6 mm in diameter) and a 10 ml syringe was constructed. The active particle was attached to the bottom end of the tube by applying suction at the top end by the syringe. The suction efficiency was improved by coating a thin film of silicon sealant around the tube circumference

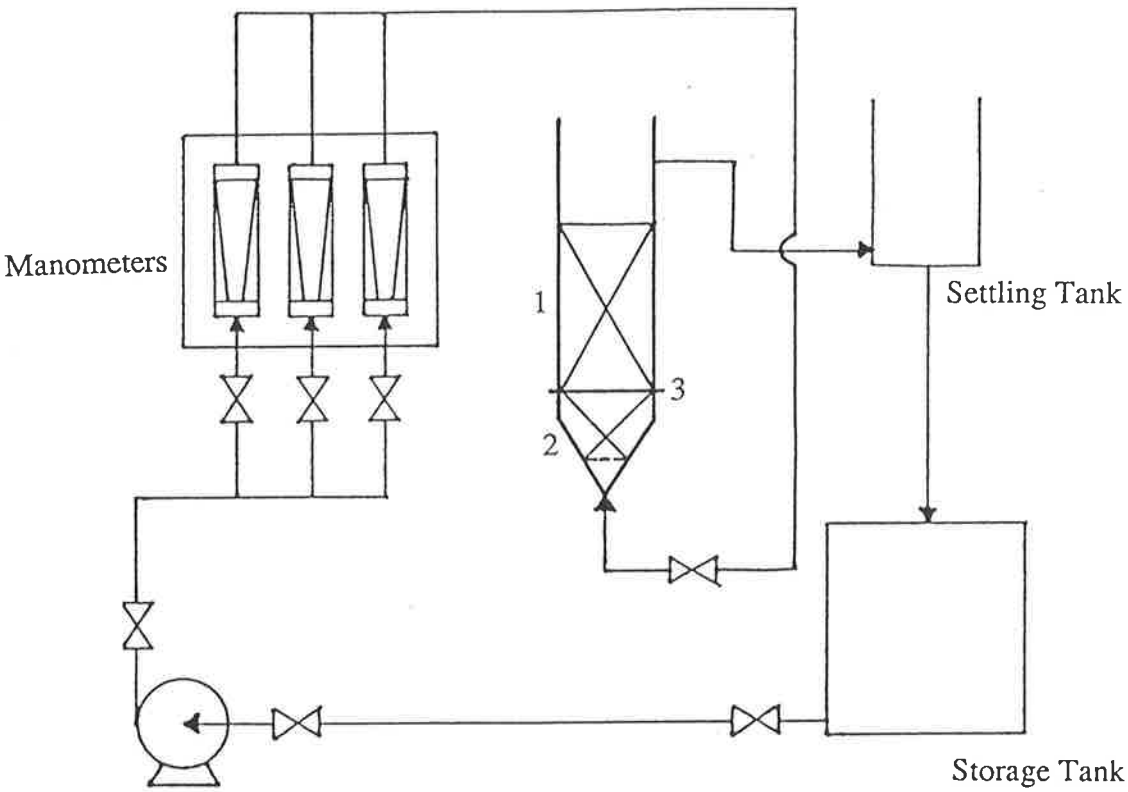

1 : Fluidized Section
2 : Calming Section
3 : Distributor Plate

Figure 7a : Experimental System

at the bottom end. To give the flexible tube a greater rigidity, it was wedged into the gap of an aluminium channel, 585 mm in length. The sampler device is shown in Figure 7b.

3.3.2 Active Particle Preparation

The active particles used in the experiments were made from acrylic spheres ($\rho_a = 1194\,kg/m^3$), 11.0 and 12.5 mm in diameter. Particles of different density were made by drilling holes into two of the larger spheres. A heavier particle ($\rho_a = 1522\,kg/m^3$) was produced by adding lead powder to the hole; a lighter particle ($\rho_a = 1079\,kg/m^3$) was produced by leaving it empty. The holes were sealed by Araldite glue.

3.3.3 Procedure

The bed was fluidized with water at a pre-determined flow rate. Sufficient bed material was added to maintain an expanded height of at least 300 mm. The sampler, with the active particle attached, was inserted to the desired depth (in this case, 280 mm) and the particle was released into the bed by removing the syringe from the tube. To ensure that the particle was released at the same time the syringe was removed, water was drawn up into the tube (before the particle was attached) so that the internal pressure at the bottom end of the tube exceeded the external fluid pressure at the bed depth of interest. The time taken for the the particle to move from rest to the top of the bed was measured, allowing an average velocity to be determined.

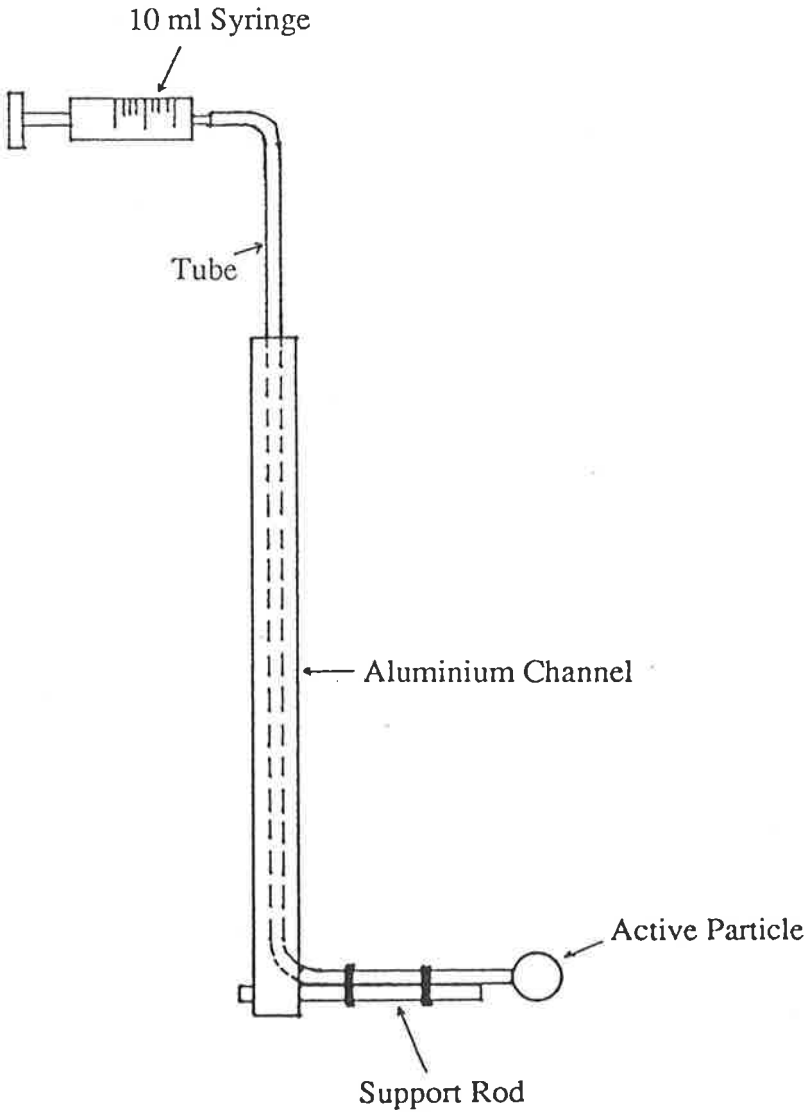

Figure 7b : Sampler Apparatus

3.4 MODELLING

3.4.1 General Development

The equation of motion (or force balance) for the active particle whilst in the emulsion phase can be written as

$$M_e \frac{dU_a}{dt} = \Sigma F_{ext} \tag{52}$$

where M_e is the effective inertial mass of the sphere, U_a is the active particle velocity in relation to the inert bed particles and ΣF_{ext} is the sum of the external forces that act on the particle (positive upwards). It is supposed that these forces can be written as

$$\Sigma F_{ext} = F_d + W_e + F_p \tag{53}$$

where F_d is the fluid drag force, W_e is the effective weight force of a particle in the suspension (weight plus buoyancy) and F_p is a particle-particle interaction force (as discussed in section 3.2.3). To solve equations 52 and 53 for the segregation velocity of an active particle, expressions for these forces in terms of this velocity are required.

FLUID DRAG FORCE: The model of Agarwal and O'Neill (1988) is used and can be expressed in the standard form as

$$F_d = C_{D\varepsilon} \frac{\pi d_a^2}{4} \frac{\rho(v - U_a) \mid v - U_a \mid}{2} \tag{54a}$$

where $v\ (= qU_0/\varepsilon)$ is the interstitial fluid velocity relative to the inert particles and $C_{D\varepsilon}$ is the porosity dependent drag coefficient which in terms of Re_G, the

generalized Reynolds Number (section 2.3.1), is

$$C_{D\varepsilon} = q\left(4\left(\frac{6}{Re_G}\right) + C_i\right) \tag{54b}$$

where $C_i\ (= C_{D\infty} - 24/Re_{a,\infty})$ accounts for the inertial fraction of the total drag. Correlations for $C_{D\infty}$, the drag coefficient for the particle in an infinite fluid, are well known and generally can be expressed in the form

$$C_{D\infty} = \frac{24}{Re_a} + \frac{K_1}{Re_a^n} + K_2 \tag{54c}$$

Note that the active particle Reynolds number, Re_a, is based on the superficial approach velocity, which for this problem, will be $|v - U_a|\varepsilon/q$. Equation 54c in equation 54b gives

$$C_{D\varepsilon} = \frac{24}{Re_a}(2z(1-\varepsilon)) + q\left(\frac{K_1}{Re_a^n} + K_2\right) \tag{54d}$$

For the conditions considered in this study, it is expected that Re_a, will always be less than 1000. Consequently, the $C_{D\infty}$ correlation of Lapple (1951) is used since for this Reynolds number region, this relation has a deviation of less than five percent. The coefficients defined in equation 54c are $K_1 = 3$, $K_2 = 0$, and $n = 0.28$. Equation 54a, with manipulation, now becomes

$$F_d = a_1(v - U_a) + a_2|v - U_a|^{1-n}(v - U_a) + a_3(v - U_a)|v - U_a| \tag{55}$$

where the coefficients a_1, a_2 and a_3 are solely functions of the bed properties and are given in Table 8.

The z factor is derived from the Hawksley (1951) relation for U_0/U_∞ (as discussed by Agarwal and O'Neill, 1988)

$$zq^2 = \frac{1}{2}\frac{\varepsilon}{1-\varepsilon}\exp\left(\frac{2.5(1-\varepsilon)}{1-39/64(1-\varepsilon)}\right) \tag{56}$$

TABLE 8

a_i Coefficients for use in the General Fluid Drag Force Model (equation 55)

Coefficient	Expression
a_1	$6\pi z q \frac{1-\varepsilon}{\varepsilon}\mu d_a$
a_2	$\frac{K_1}{8}\pi\rho d_a^2 q\left(\frac{\mu q}{\rho\varepsilon d_a}\right)^n$
a_3	$\frac{K_2}{8}\pi\rho d_a^2 q$

The tortuosity factor has already been presented in Table 4. It may be noted that this expression is different from that used in Chapter 2 (Table 4). There is no significant difference between the two zq^2 expressions for $\varepsilon > 0.53$; the expression in Table 4, however, is discontinuous at a porosity of 0.5 . Now, the analysis presented here in this study is strictly applicable to only fluidized beds; the previous analysis in Chapter 2 sought to unify transport phenomena for both packed and fluidized beds under viscous flow conditions. Consequently, there is no need to use the discontinous expression outlined in Table 4 for zq^2 which implicitly accounts for the transition between the packed and fluidized state at a porosity between 0.4 and 0.5. The relation given in equation 56 is a continous function that will be applicable over the whole range of fluidized bed porosities and is consequently easier to use in this case.

EFFECTIVE WEIGHT FORCE: As discussed in the literature survey (section 3.2.3), the exact form of this relation is controversial. However, the approach of Agarwal and O'Neill (1988) (in their development of the fluid drag model given in equation 54a) assumes that the buoyancy force is given in terms of the suspension density. Hence to be consistent this form is also used here, so that

$$W_e = (\overline{\rho_s} - \rho_a)\frac{\pi d_a^3}{6} g = a_4 \tag{57}$$

PARTICLE-PARTICLE INTERACTION FORCE: This force represents the resistance provided by the inert particles to the relative motion of the active particle. The suspension viscosity relations discussed earlier in section 3.2.3 characterise this force in terms of shearing both the particles and the fluid. However, the fluid drag expression given in equation 55 has already accounted

for the effects of the fluid. Hence, to use the suspension viscosity relations, this fluid shear effect must be deleted, thus leaving only the particle interaction effects with the shear boundary (that is, the active particle surface) and the transfer of this shear to the suspension bulk via collisions, rotations and so on.

For solid fractions in which the particle interaction force will be significant, the suspension viscosity will be high. Consequently, it would be reasonable to assume that the rate of shear will be low and under these conditions the suspension can be modelled as a Newtonian fluid (Cheng, 1980a). This allows us to write

$$\overline{F_s} = -3\pi\overline{\mu_s} d_a U_a \tag{58}$$

where $\overline{F_s}$ is the shear force produced from shearing the suspension as a whole. As a first approximation, one may consider this force as a linear combination of the individual fluid and particle interactions with the shear boundary; that is

$$\overline{F_s} = F_p + F_f \tag{59a}$$

F_f is the fluid drag contribution and F_p is that part of the total force due to particle interactions. Noting that for liquid suspensions, the viscosities are derived for particles suspended in a stagnant fluid and assuming low shear rate conditions

$$\overline{\mu_p} = \overline{\mu_s} - \mu \tag{59b}$$

where $\overline{\mu_p}$ is an effective viscosity that characterises the particle interaction force. Hence,

$$F_p = -3\pi\overline{\mu_p} d_a U_a = -a_5 U_a \tag{60}$$

In terms of the Thomas model for $\overline{\mu_s}$ (equation 48), $\overline{\mu_p}$ becomes

$$\overline{\mu_p} = \mu(2.5\phi_s + 10.05\phi_s^2 + 0.00273\exp(16.6\phi_s)) \tag{61a}$$

or in terms of the Kawase and Ulbrecht model (equation 50)

$$\overline{\mu_p} = \mu\left(\frac{2.478\phi_s - 10.253\phi_s^5 + 20.326\phi_s^6}{1 - 2.478\phi_s + 18.456\phi_s^5 - 20.326\phi_s^6}\right) \tag{61b}$$

For gas beds, $\overline{\mu_s}$ is in the range 0.5 to 2.0 Pa.s (Table 7) and μ is of the order 10^{-5} Pa.s . Hence, equation 60 can be used for the particle interaction force with $\overline{\mu_p}$ taken as $\overline{\mu_s}$ for these suspensions.

Substitution of equations 55, 57 and 60 in equation 52 gives

$$M_e \frac{dU_a}{dt} = a_1(v - U_a) + a_2 |v - U_a|^{1-n} (v - U_a) + a_3(v - U_a)|v - U_a| + a_4 - a_5 U_a \quad (62)$$

The coefficients, a_1 through a_5, are all known functions of the bed properties.

Two separate conditions can occur:

1) the active particle moves at a velocity less than the intersitial fluid; F_d will be directed upwards (and positive) and $|v - U_a|$ will equal $(v - U_a)$. Equation 62 becomes

$$M_e \frac{dU_a}{dt} = a_1(v - U_a) + a_2(v - U_a)^{2-n} + a_3(v - U_a)^2 + a_4 - a_5 U_a \quad (63a)$$

2) the active particle moves upwards faster than the interstitial fluid so that F_d will be downwards (and negative) and $|v - U_a|$ will equal $(U_a - v)$. For this case

$$M_e \frac{dU_a}{dt} = -a_1(v - U_a) - a_2(v - U_a)^{2-n} - a_3(v - U_a)^2 + a_4 - a_5 U_a \quad (63b)$$

The first and second cases above will hereafter be referred to as the low and high velocity models respectively.

To obtain an analytical solution for the segregation velocity, U_s, the troublesome non-integer power term (that is, x^{2-n}) must be removed. This is achieved by using a Taylor Series approximation. Expansion to the second term of the series should be sufficient since the non-integer power, 2-n, will between 1

and 2 (for example, n is 0.28 from the Lapple (1951) model). The series is centered at the point, U_{a0} equal to k v, where for the low velocity model (v$-U_a > 0$), k equals k_1 (which is less than 1), and for the high velocity model (v$-U_a < 0$), k equals k_2 (which is greater than 1). The expansion (as outlined in Appendix D) yields for the low velocity case

$$(\mathrm{v}-U_a)^{2-n} = b_1 - b_2 U_a + b_3 U_a^2 \tag{64a}$$

so that equation 63a becomes

$$M_e(dU_a/dt) = (a_1\,\mathrm{v} + a_2 b_1 + a_3\,\mathrm{v}^2 + a_4) - (a_1 + a_2 b_2 + 2a_3\,\mathrm{v} + a_5)\,U_a + (a_3 + a_2 b_3)\,U_a^2 \tag{64b}$$

$$= A_3 - A_2 U_a + A_1 U_a^2 \tag{64c}$$

and likewise for the high velocity case

$$(U_a - \mathrm{v})^{2-n} = b_4 + b_5 U_a + b_6 U_a^2 \tag{65a}$$

and equation 63b

$$M_e(dU_a/dt) = (a_1\,\mathrm{v} - a_2 b_4 - a_3\,\mathrm{v}^2 + a_4) - (a_1 + a_2 b_4 - 2a_3\,\mathrm{v} + a_5)\,U_a - (a_3 + a_2 b_6)\,U_a^2 \tag{65b}$$

$$= A_6 - A_5 U_a + A_4 U_a^2 \tag{65c}$$

The coefficients b_1 through b_6, in their most general form, are given in Table 9.

3.4.2 Steady State Analysis - Terminal Segregation Velocities

The equation of motion for the low velocity case (equation 64c) with the acceleration term neglected becomes

$$0 = A_3 - A_2 U_a + A_1 U_a^2 \tag{66c}$$

This quadratic has the solutions

TABLE 9

b_i Coefficients for use in the High and Low Velocity Models for the Fluid Drag Force (equations 64 and 65)

Coefficient	Expression
b_1	$\left((1-k_1)^{2-n}+(2-n)(1-k_1)^{1-n}k_1+\frac{(2-n)(1-n)}{2}(1-k_1)^{-n}k_1^2\right)v^{2-n}$
b_2	$((2-n)(1-k_1)^{1-n}+(2-n)(1-n)(1-k_1)^{-n}k_1)v^{1-n}$
b_3	$\left(\frac{(2-n)(1-n)}{2}(1-k_1)^{-n}\right)v^{-n}$
b_4	$\left((k_2-1)^{2-n}-(2-n)(k_2-1)^{1-n}k_2+\frac{(2-n)(1-n)}{2}(k_2-1)^{-n}k_2^2\right)v^{2-n}$
b_5	$((2-n)(k_2-1)^{1-n}-(2-n)(1-n)(k_2-1)^{-n}k_2)v^{1-n}$
b_6	$\left(\frac{(2-n)(1-n)}{2}(k_2-1)^{-n}\right)v^{-n}$

$$(U_a)_1 = \frac{A_2 - \sqrt{A_2^2 - 4A_1A_3}}{2A_1} \tag{66b}$$

$$(U_a)_2 = \frac{A_2 + \sqrt{A_2^2 - 4A_1A_3}}{2A_1} \tag{66c}$$

Likewise for the high velocity case,

$$(U_a)_1 = \frac{A_5 + \sqrt{A_5^2 - 4A_4A_6}}{2A_4} \tag{67a}$$

$$(U_a)_2 = \frac{A_5 - \sqrt{A_5^2 - 4A_4A_6}}{2A_4} \tag{67b}$$

The correct solution is $(U_a)_1$, since $(U_a)_2$ violates the velocity condition for both of the above cases; that is, $(U_a)_2$ is greater than v for the low velocity model and is less than v for the high velocity model.

The exact value for $(U_a)_1$ may be determined by varying k_1 (or k_2 depending on the model being considered), until the $(U_a)_1/v$ ratio becomes equal to k_1 (or k_2). Variation of this k value around the exact solution gave a small (if any) change in the $(U_a)_1$ solution; the $(U_a)_2$ value however is very sensitive to k and could change by over 100% even for a small variation.

3.4.3 Unsteady State Analysis

When the external forces applied to the active particle are not balanced, acceleration will occur. The particle velocity, under these conditions, is given by equations 64 and 65 for the low and high velocity models respectively.

The effective inertial mass of the particle, M_e, must account for the acceleration of the nearby suspension as well. This effect is expressed in terms of a virtual mass coefficient, $V(\varepsilon)$, as

$$M_e = M_a(1 + V(\varepsilon)) \tag{68}$$

Bassett (1888) derived

$$V(\varepsilon = 1) = \frac{1}{2} \tag{69a}$$

for a particle accelerating in an infinite fluid. For solid-fluid suspensions, Reitema (1982) recommends

$$V(\varepsilon) = \frac{\varepsilon}{2} \tag{69b}$$

This form is assumed in this analysis.

To obtain an analytical solution for the dynamic response of the active particle, integration of equations 64 and 65 is required. However, this step requires the quadratic in these equations in a factorised form, that is, for the low velocity case

$$A_3 - A_2 U_a + A_1 U_a^2 = A_1 (U_a - U_{a1})(U_a - U_{a2}) \tag{70}$$

However, as pointed out above, the $(U_a)_2$ root is physically meaningless, as well as extremely sensitive to k_1. This in turn implies that integration of the factorised equation results in a solution that is also physically meaningless. It is therefore not possible to solve analytically, and numerical solution of the general force balance was sought. Putting Y (= v - U_a) into equation 62 gives

$$-M_e \frac{dY}{dt} = (a_1 - a_5)Y + a_2 Y \mid Y \mid^{1-n} + a_3 Y \mid Y \mid + (a_4 + a_5)\mathrm{v} \tag{71}$$

Numerical integration of this equation will allow the determination of the unsteady particle velocity at any time, t (for a specified initial velocity).

3.4.4 Criteria for Flotsam

In the general case, the necessary condition for the active particle to be flotsam is that the particle moves upward with respect to the inert bed particles. The sufficient condition is that the active particle will move up in relation to the container walls whilst in the emulsion phase. These conditions are expressed more fully in the following.

NECESSARY CONDITIONS: Assume at t = 0, U_a = 0. The general equation of motion (equation 62) reduces to

$$M_e\left(\frac{dU_a}{dt}\right)_{t=0} = (a_1 \mathrm{v} + a_2 \mathrm{v}^{2-n} + a_3 \mathrm{v}^2) + a_4 \tag{72}$$

The term in brackets is the initial fluid drag force (which is always positive) and a_4 is the effective weight force acting on the particle (equation 57). For the active particle to move upwards, the initial acceleration, $(dU_a/dt)_{t=0}$ must be positive, that is,

$$a_1 \mathrm{v} + a_2 \mathrm{v}^{2-n} + a_3 \mathrm{v}^2 > -a_4 \tag{73}$$

Equation 73 represents the necessary flotsam condition. If a_4 is positive (that is, $\rho_a < \rho_s$), then the condition will always be satisfied since both forces act upwards. However, if a_4 is negative ($\rho_a > \rho_s$), this condition will not always hold.

As expected, the particle interaction force has no influence on this condition.

SUFFICIENT CONDITIONS: For particulate fluidized beds, there is no net motion of the inert bed material. Consequently, the necessary flotsam condition given in equation 73 is also sufficient.

The inert particles in the emulsion phase of a bubbling fluidized bed, however, have a non-zero downwards convection velocity, U_D (section 3.1.1). Kunii and Levenspiel (1969) have estimated this velocity as

$$U_D = \frac{\alpha \varepsilon_b U_b}{1 - \varepsilon_b - \alpha \varepsilon_b} \tag{74}$$

where U_b is the bubble rise velocity, α is the fraction of a bubble that is solids (assumed to be 1/3) and ε_b is the bubble fraction. To estimate U_D, U_b may be obtained using (Davidson and Harrison, 1963)

$$U_b = (U_0 - U_{mf}) + 0.71(g\overline{d_b})^{1/2} \tag{75a}$$

and the height averaged bubble diameter, $\overline{d_b}$, can be determined from the model of Darton et al. (1977)

$$\overline{d_b} = \frac{0.3(U_0 - U_{mf})^{0.4}}{g^{0.2} L}[(L + 4\sqrt{A_0})^{0.8} - (4\sqrt{A_0})^{0.8}] \tag{75b}$$

A_0 is the area of a multi-orifice distributor per hole and is taken as 0.56 0.56×10^{-6} m^2 for a porous plate distributor. The bubble fraction can then be estimated (Valenzuela and Glicksman, 1985) as

$$\varepsilon_b = \frac{U_0 - U_{mf}}{U_b + 2U_{mf}} \tag{75c}$$

Keeping in mind that the active particle can only move downwards in the emulsion phase (section 3.1.1), the sufficient condition can be written as

$$U_a + U_D > 0 \tag{76}$$

since $(U_a + U_D)$ is the segregation velocity of the particle in the emulsion in relation to the container walls. The steady state velocity, U_a (equations 66b and 67a), is used since if the particle spends sufficient time in the emulsion, it will accelerate to this velocity.

3.5 RESULTS AND DISCUSSION

Details of the literature data used in the model comparisons below are given in the literature survey (section 3.2).

3.5.1 Steady State Segregation Velocity

The terminal falling velocity data of Martin et al. (1981) are compared with the model predictions in Figures 8a-d. Since (v - U_s) is positive in this case, the low velocity model (equation 66b) is used. Predictions assuming both the Thomas model (equation 61a) and the Kawase and Ulbrecht model (equation 61b) for the particle interaction viscosity, $\overline{\mu_p}$, are presented. The model predictions that result assuming $\overline{\mu_p}$ as zero are also given. The agreement between the data and model is generally good over the entire flow range considered; some deviation occurs at the intermediate flow velocities in the Figures 8c and d. The $\overline{\mu_p}$ equal to zero solution deviates from the data significantly at lower porosities. At high porosities, there is no difference between the Kawase and Ulbrecht and Thomas expressions as expected (Figure 5). At lower porosities, the Kawase and Ulbrecht model is more severe (that is, $\overline{\mu_p}$ is higher). When the fluid velocity reaches the isolated terminal velocity of the inert particles, U_{i_∞}, they will be carried away and the bed porosity becomes one. Now, any increase in the fluid velocity before U_{i_∞} is reached, decreases the positive buoyancy force and the negative particle interaction force (since porosity rises), which results in a faster falling velocity of the active particle as observed in Figure 8. However, if the fluid velocity is increased above U_{i_∞} the falling velocity decreases because only the upwards fluid drag changes. This behaviour is also shown in Figure 8.

In Figures 9a and b, the terminal segregation velocity data of Prudhoe and Whitmore (1964) are plotted against the active particle diameter, d_a, with the active

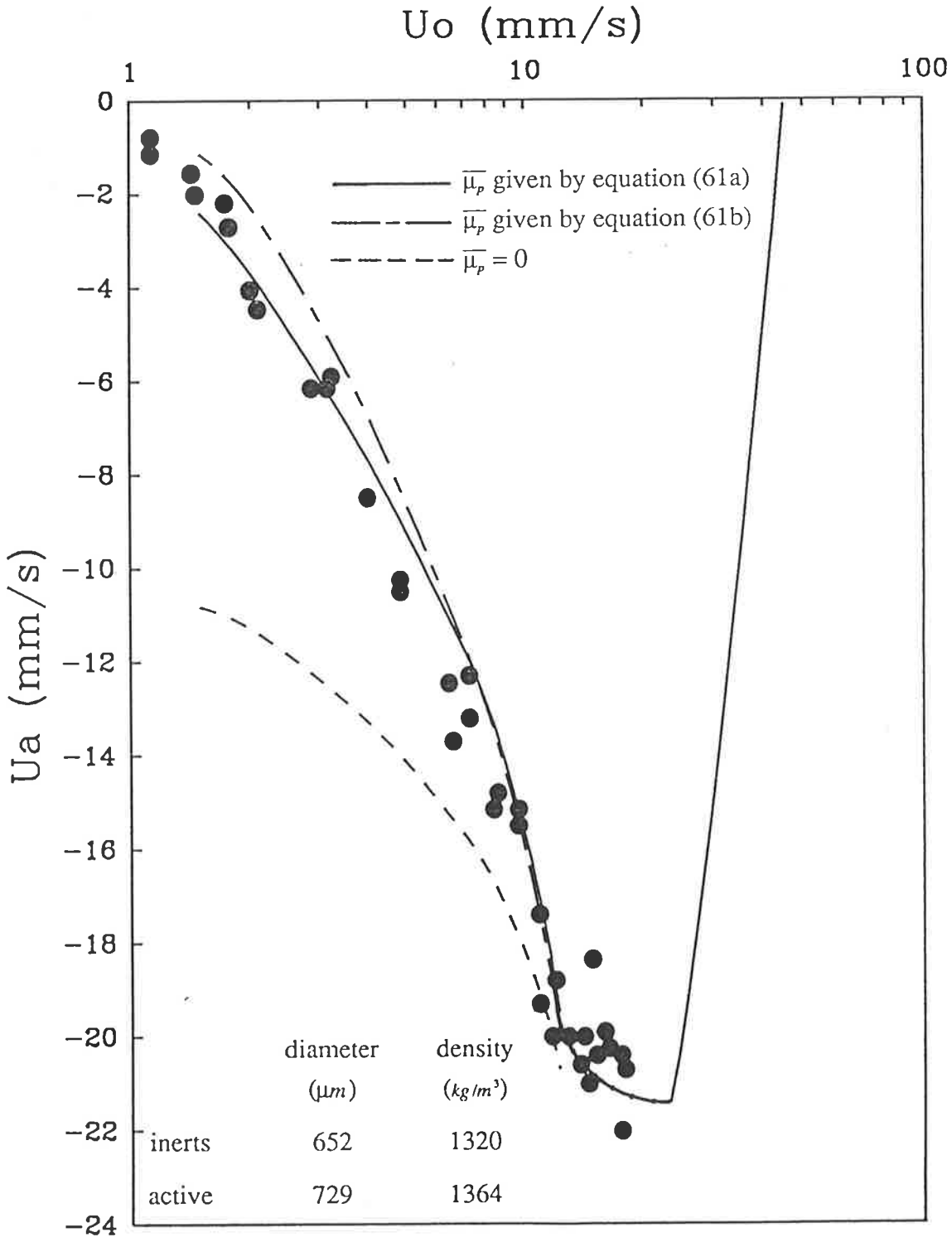

(8a)

Figure 8 : Terminal Segregation Velocities of Heavy Active Particles falling through a Liquid Fluidized Bed of Ion Exchange Beads : comparison of equation 66 with the data of Martin et al. (1981)

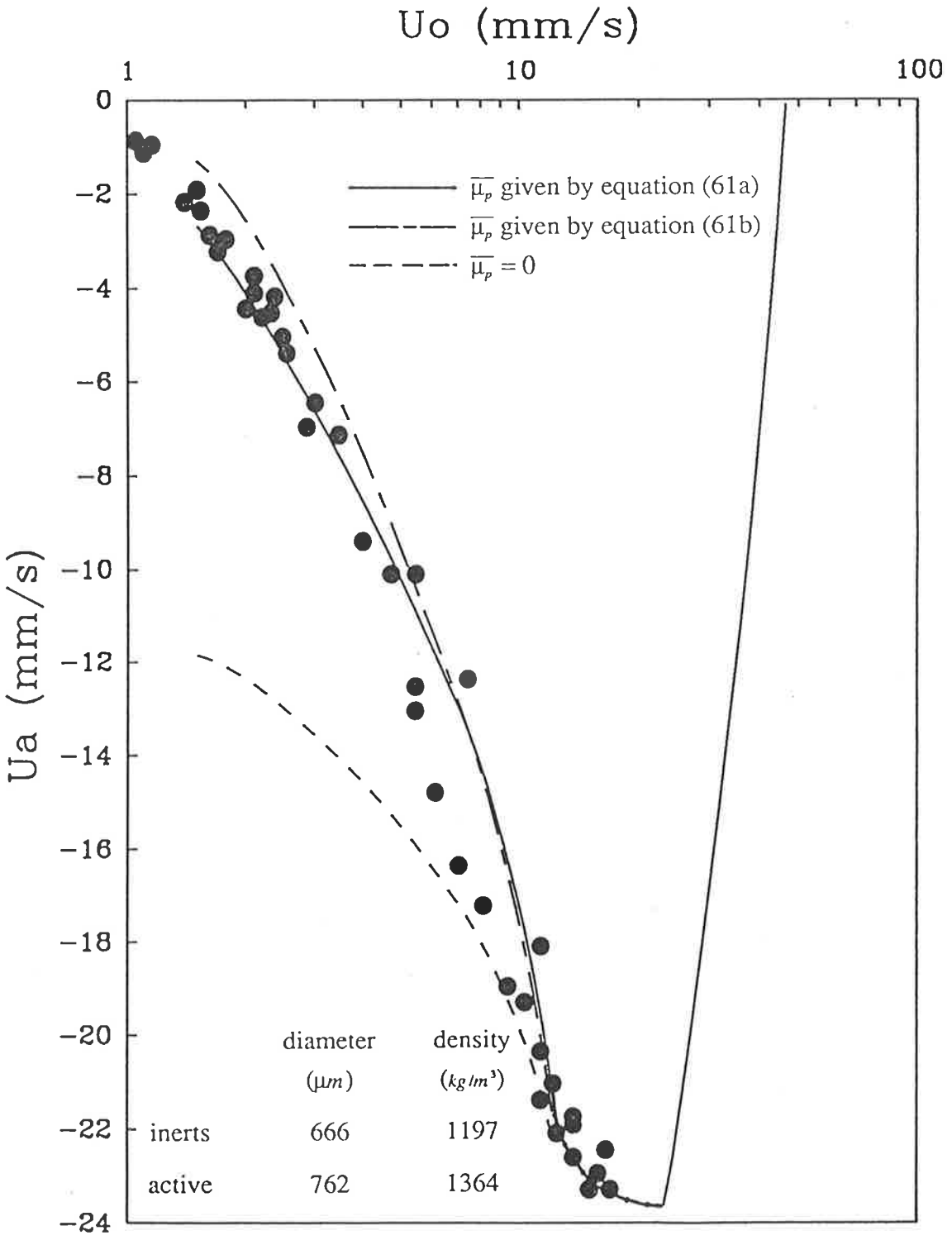
Uo (mm/s)
1
10
100
0
−2
−4
−6
−8
−10
−12
−14
−16
−18
−20
−22
−24
Ua (mm/s)
$\overline{\mu_p}$ given by equation (61a)
$\overline{\mu_p}$ given by equation (61b)
$\overline{\mu_p} = 0$
diameter (μm)
density (kg/m^3)
inerts 666 1197
active 762 1364

(8b)

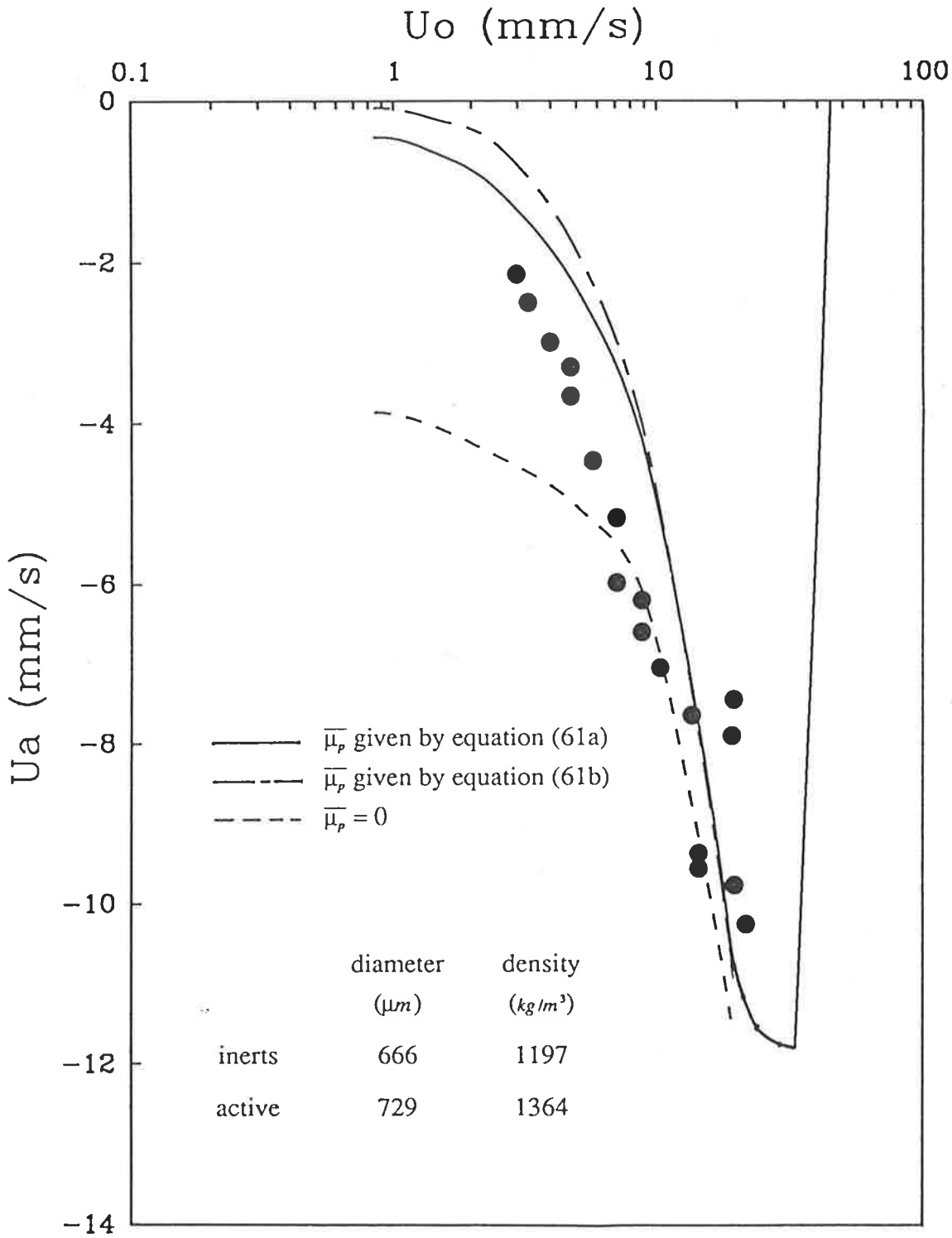
Uo (mm/s)
0.1
1
10
100
0
-2
-4
-6
-8
-10
-12
-14
Ua (mm/s)
$\overline{\mu_p}$ given by equation (61a)
$\overline{\mu_p}$ given by equation (61b)
$\overline{\mu_p} = 0$
diameter (μm)
density (kg/m^3)
inerts 666 1197
active 729 1364

(8c)

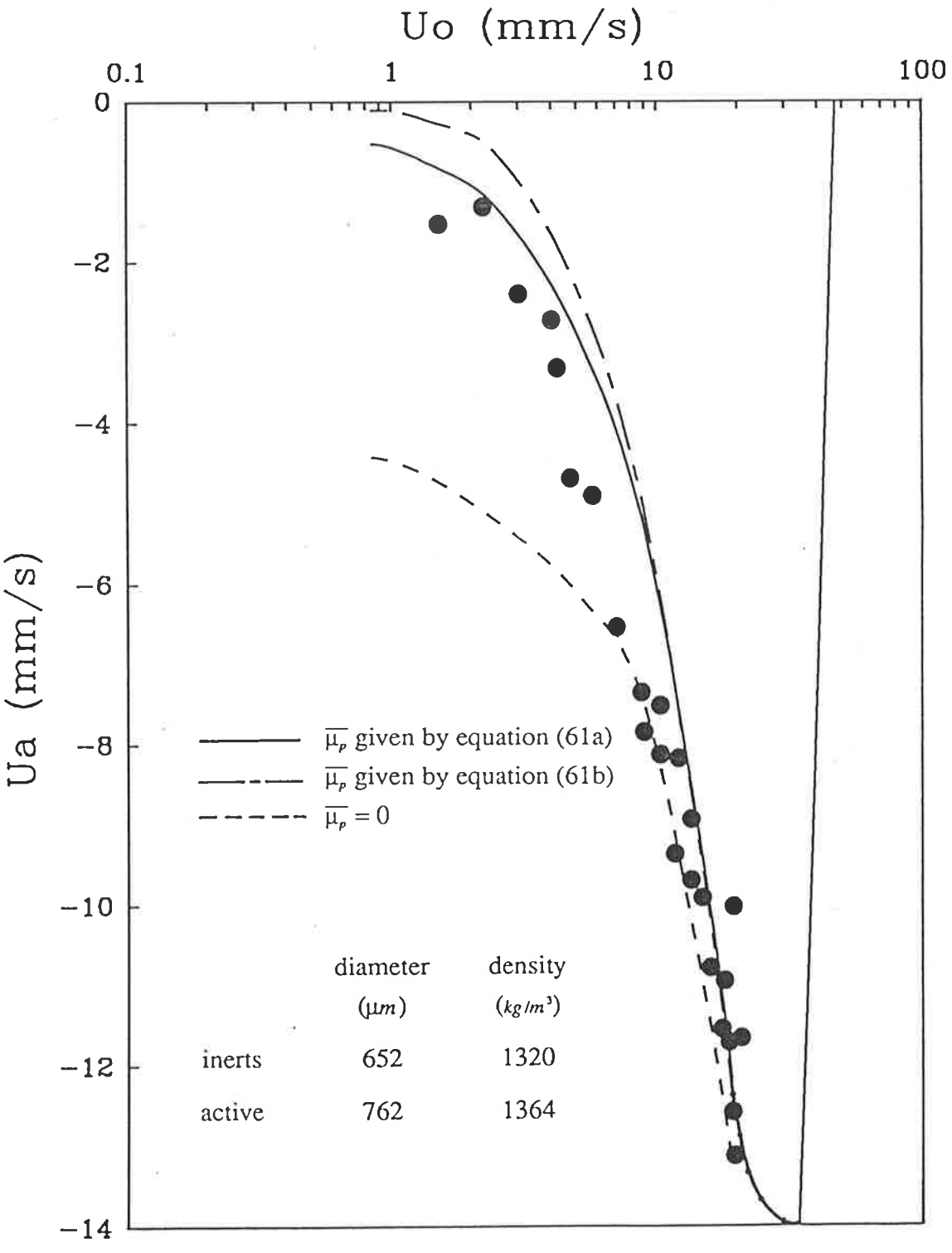
Uo (mm/s)
0.1
1
10
100
0
-2
-4
-6
-8
-10
-12
-14
Ua (mm/s)
$\overline{\mu_p}$ given by equation (61a)
$\overline{\mu_p}$ given by equation (61b)
$\overline{\mu_p} = 0$
diameter (μm)
density (kg/m³)
inerts 652 1320
active 762 1364

(8d)

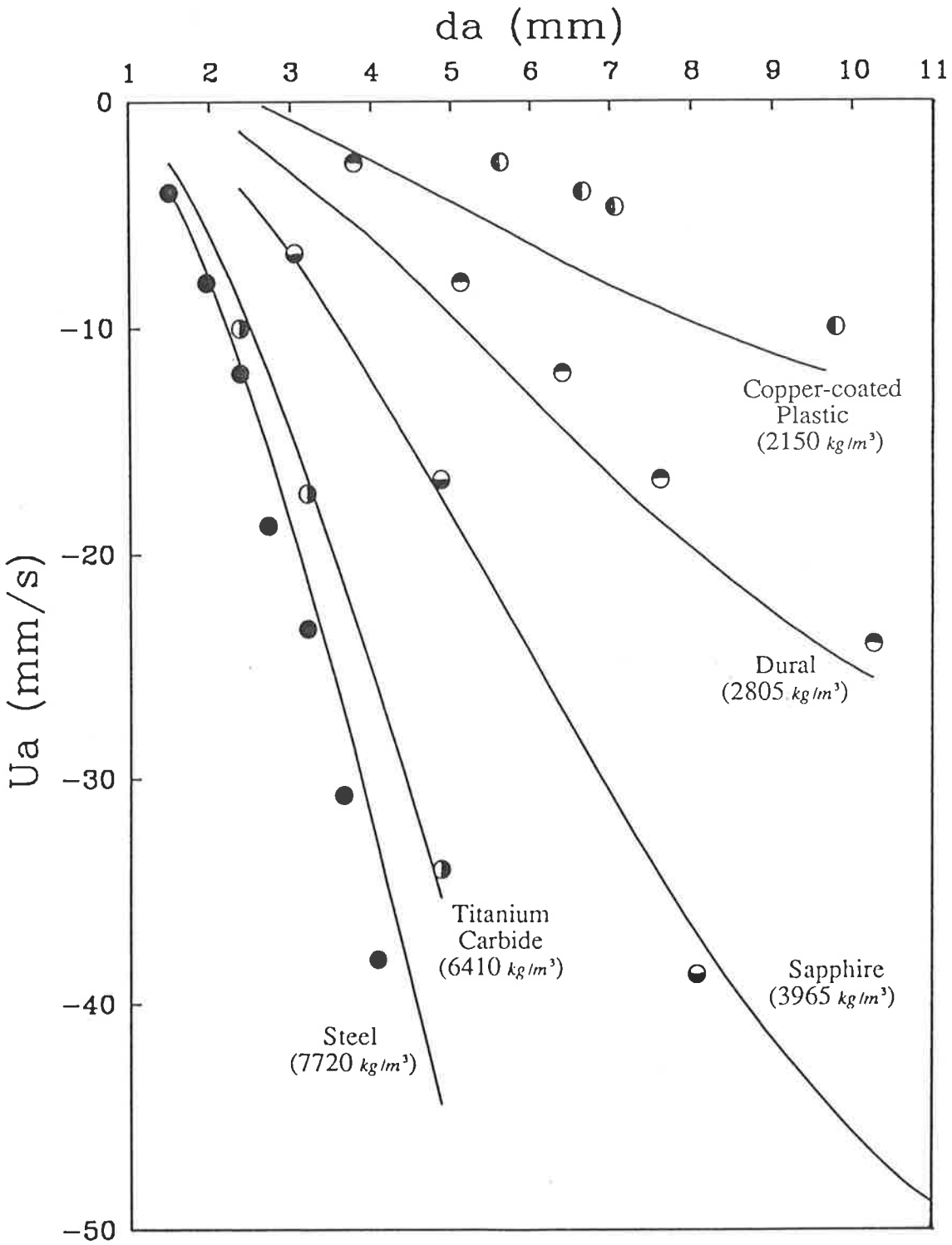

(9a) : bed porosity = 0.77

Figure 9 : Terminal Segregation Velocities of Heavy Active Particles falling through a Liquid Fluidized Bed of Glass Ballotini : comparison of equation 77 with the data of Prudhoe and Whitmore (1964)

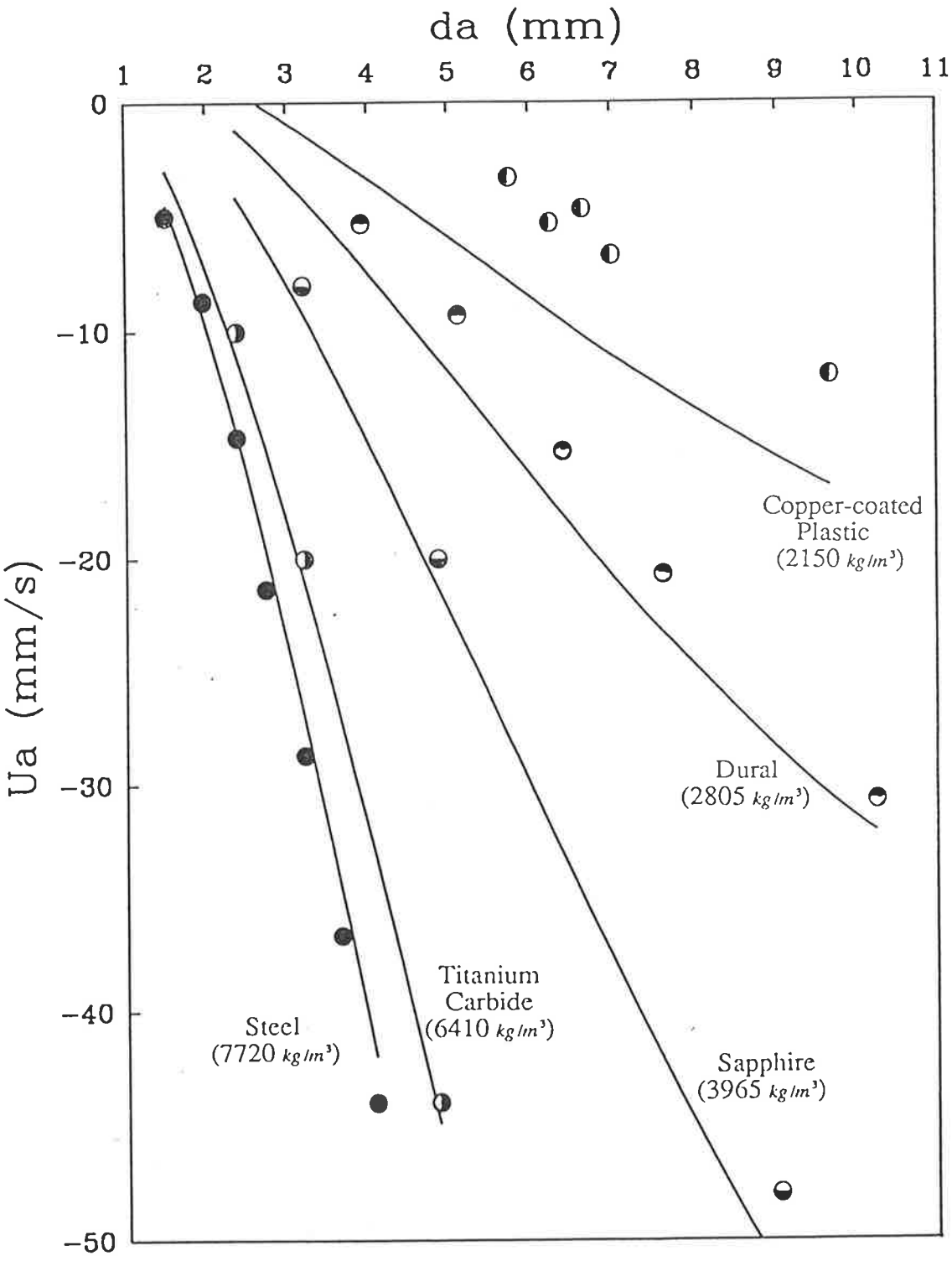

(9b) : bed porosity = 0.81

particle density, ρ_a, as a parameter. Oil was used to ensure viscous flow conditions prevailed; consequently, the generalized viscous flow drag expression from Chapter 2 applies (equation 7). The general force balance (equation 62), therefore, becomes under steady state conditions

$$0 = a_1(\mathrm{v} - U_a) + a_4 - a_7 U_a \tag{77a}$$

So for viscous flow conditions

$$U_a = \frac{a_4 + a_1 \mathrm{v}}{a_1 + a_7} \tag{77b}$$

Using equations 57, 60 and Table 8 in equation 77b gives

$$U_a = \frac{1}{(\overline{\mu_p}/\mu + 2zq(1-\varepsilon)/\varepsilon)} \left(\frac{(\overline{\rho_s} - \rho_a)g}{18\mu} d_a^2 + 2zq \frac{1-\varepsilon}{\varepsilon} \mathrm{v} \right) \tag{77c}$$

so that U_a is proportional to d_a^2, which is an expected result for this flow regime. Comparison of equation 77c with the experimental data in Figures 9a and b is excellent with the data trends being well predicted by the model for all cases. The model tends to overpredict experiment for the lighter particles. In addition, the following points need to be made:

1) the model, as plotted is not a true d^2 form because the experiments were performed under conditions where the d_a/D_t ratio was sufficiently high for the retarding effects of the walls to be significant. Prudhoe and Whitmore (1964) verified that the Francis equation

$$(U_a)_w = U_a \left(\frac{1 - d_a/D_t}{1 - 0.475 d_a/D_t} \right)^4 \tag{77d}$$

accounts for this effect in the fluidized beds they tested. Hence, deviation from the d^2 law at higher d_a values would be expected.

2) the model predictions presented in Figure 9 assumed the Thomas model for the particle interaction viscosity. No distinction between this model and the Kawase and Ulbrecht model need be applied in this case because the experiments were performed at porosities greater than 0.7 .

The laminar flow expression is certainly much easier to use than the full expression (equation 66b) since there is no k factor to be adjusted. A quick check revealed, however, that the predictions from the laminar flow model was within ten percent of this more detailed solution for all the conditions considered. The maximum deviation occurred at the high d_a and U_a values where the low Reynolds number assumption is expected to be less valid.

It is also interesting to note that the solution obtained by assuming k_1 as zero in the full steady state model (equation 66b) was within one percent of the exact solution for the conditions of Martin et al. (1981) and within six percent for the conditions of Prudhoe and Whitmore (1964).

Figure 10 presents the segregation velocity data of Daniels (1962) who measured the rate of fall of metallic spheres through a particulate air fluidized bed of sand particles. A preliminary calculation revealed that for the conditions used, fluid drag effects could be neglected. The full force balance (equation 62), under steady state conditions, gives

$$U_a = \frac{(\overline{\rho_s} - \rho_a)g}{18\overline{\mu_p}} d_a^2 \tag{78}$$

where the particle interaction viscosity, $\overline{\mu_p}$, for the gas-solid suspension, may be used as an adjustable parameter (within the range 0.5 to 2.0 Pa.s (Table 7)). Excellent agreement between the model predictions (equation 78) and the data was obtained with $\overline{\mu_p}$ equal to 1.73 Pa.s (Figure 10). This high value of $\overline{\mu_p}$ is reasonable since the coarse sand particles would be expected to produce a higher resistance to shear than smooth round particles (which have a low $\overline{\mu_p}$ value).

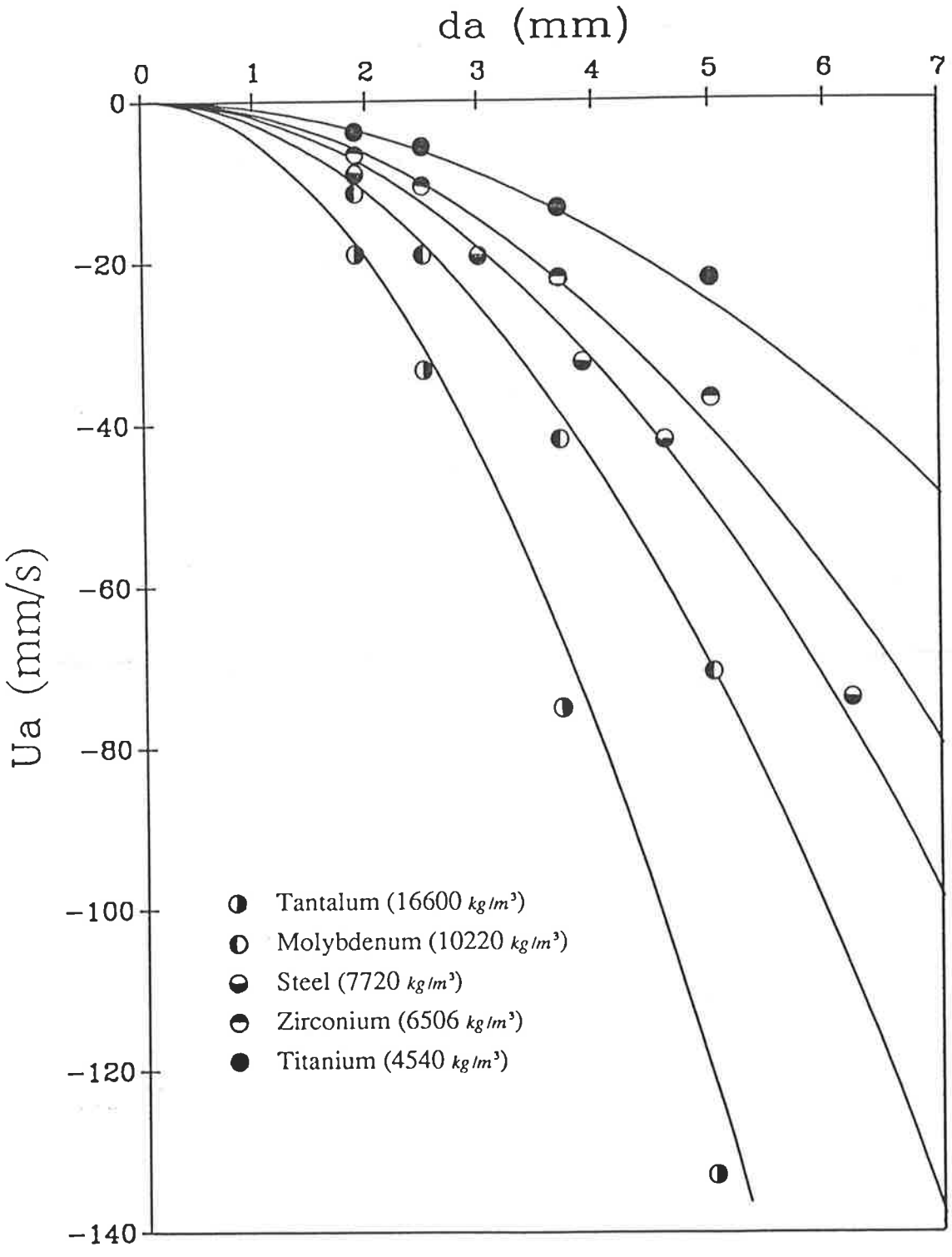

Figure 10 : Terminal Segregation Velocities of Heavy Active Particles falling through a Gas Fluidized Bed of Sand Particles : comparison of equation 78 with the data of Daniels (1961)

3.5.2 Unsteady State Segregation Velocity

To obtain a more complete test for the model, a preliminary experimental study was set up to determine the segregation velocities of active particles that are lighter than the inert bed particles and hence will rise. This is more in line with the conditions in a fluidized bed combustor. However, to delete the mixing effects of bubbles, the experiments had to be performed in a liquid fluidized bed.

Details of the active and inert particles used in the experiments are given in Table 10.

The experimentally determined porosity, ε, versus superficial velocity, U_0 curve is given in Figure 11. Comparison with the Richardson and Zaki (1954) correlation for bed expansion is also given and can be seen to be good. It can also be seen, however, that a dip in the experimental curve occurs at about U_0 equal to 13 mm/s which is unexpected and can only be due to a series of faulty readings at that flow rate.

The experimental data obtained from the preliminary study are presented in terms of an average rise velocity, L/t, where L is the length travelled (280 mm) in time, t, from rest (Figures 12a-d). The raw data is given in Appendix E.

To produce model predictions for the average rise velocity, the time taken for the particle to rise the 280 mm (from rest) was required. This time was obtained by numerically integrating the unsteady state model given in equation 71 twice.

For all the cases considered, the average rise velocity was found to increase as the fluid velocity (or bed porosity) was decreased until a critical fluid velocity (or

TABLE 10

Properties of the Inert and Active Particles used in the Experimental Study

Particle Type	Particle Material	Particle Diameter (mm)	Particle Density (kg/m^3)
A1	acrylic plus lead powder	12.6	1522
A2	acrylic	12.5	1194
A3	acrylic	12.5	1079
A4	acrylic	11.0	1192
inert	glass ballotini	0.33	2470

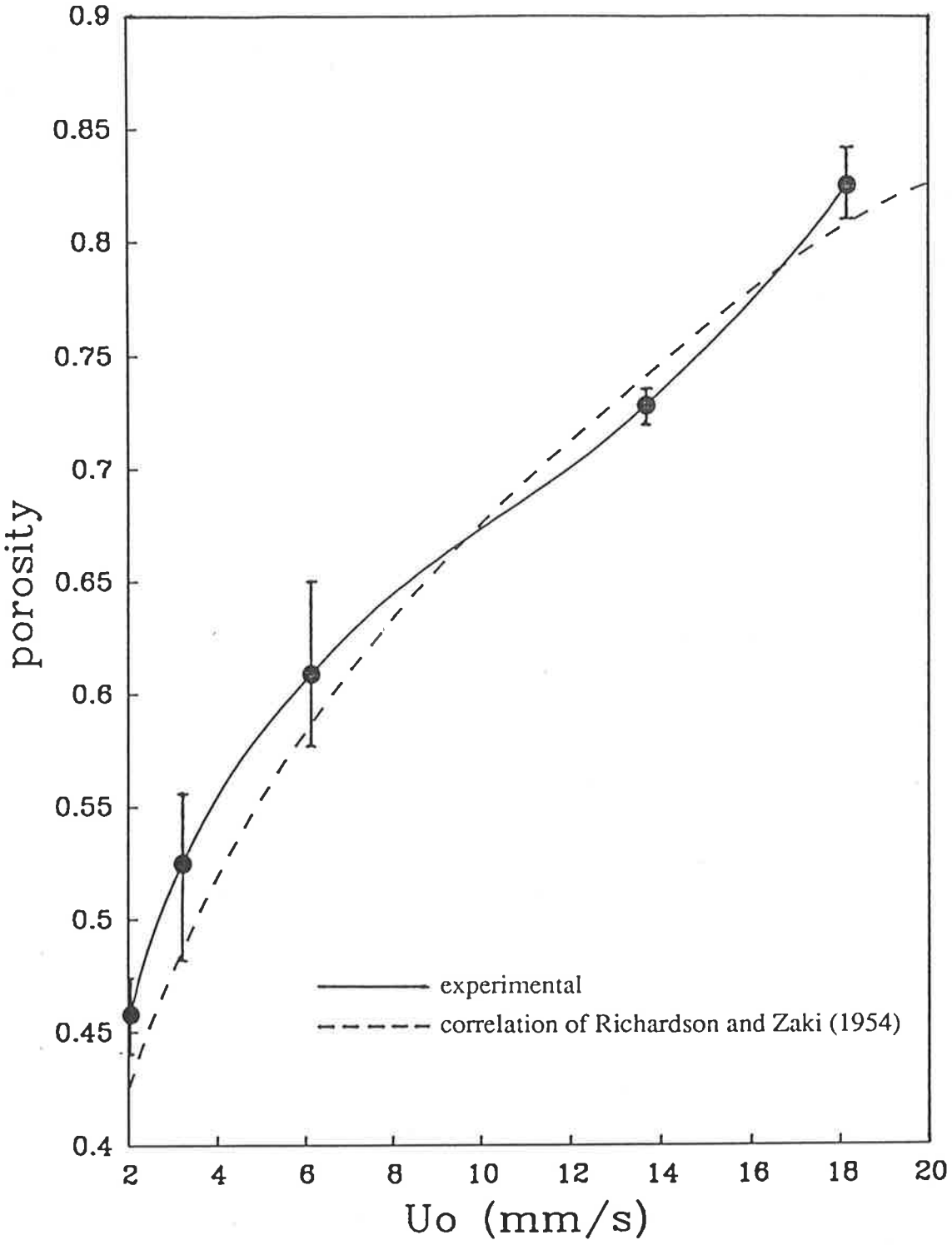

Figure 11 : Bed Porosity versus Fluid Velocity Curve

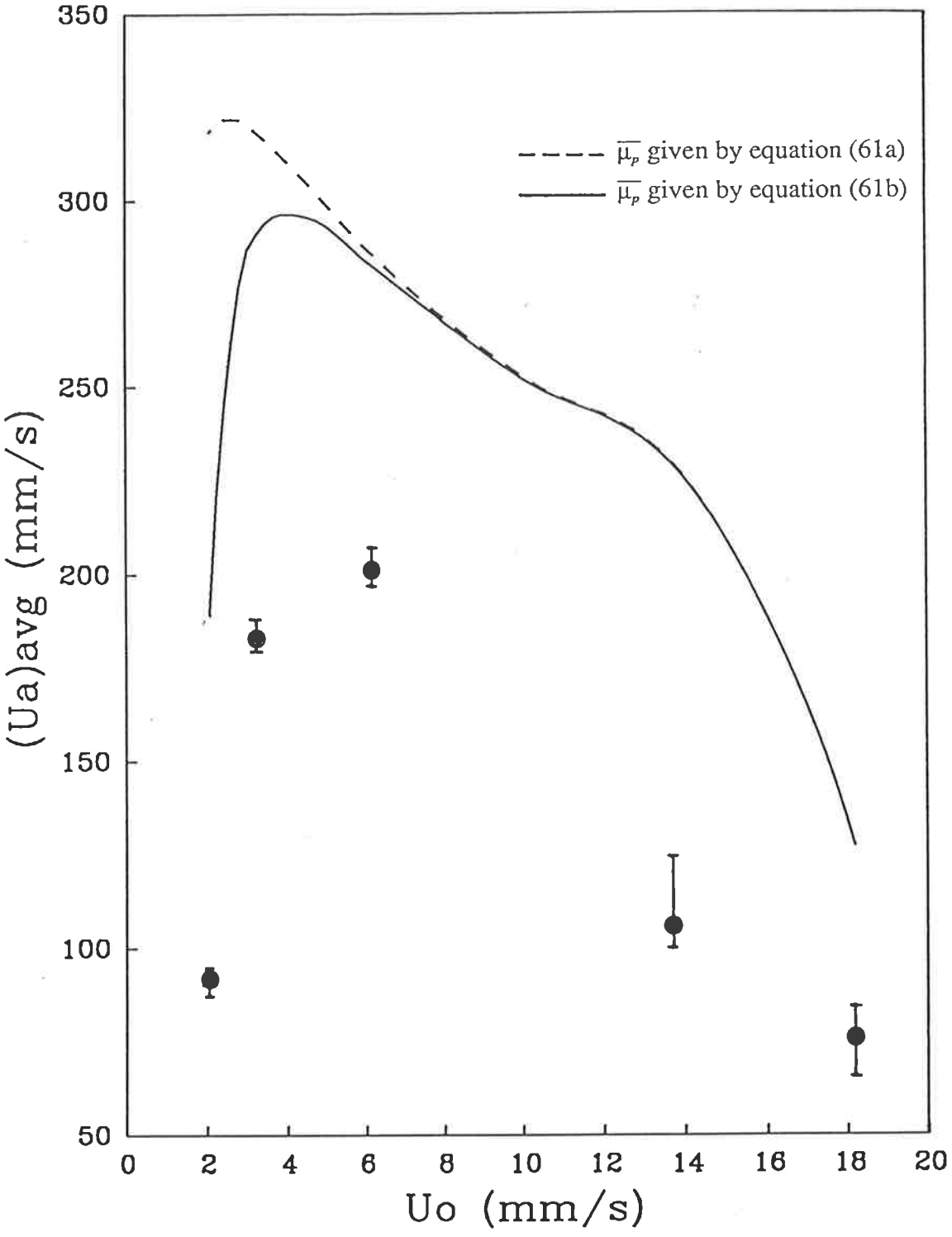

(12a) : A1 particle (12.6 mm, 1522 kg/m^3)

Figure 12 : Average Segregation Velocities of Light Active Particles rising through a Liquid Fluidized Bed of Glass Ballotini : comparison of equation 71 with experiment

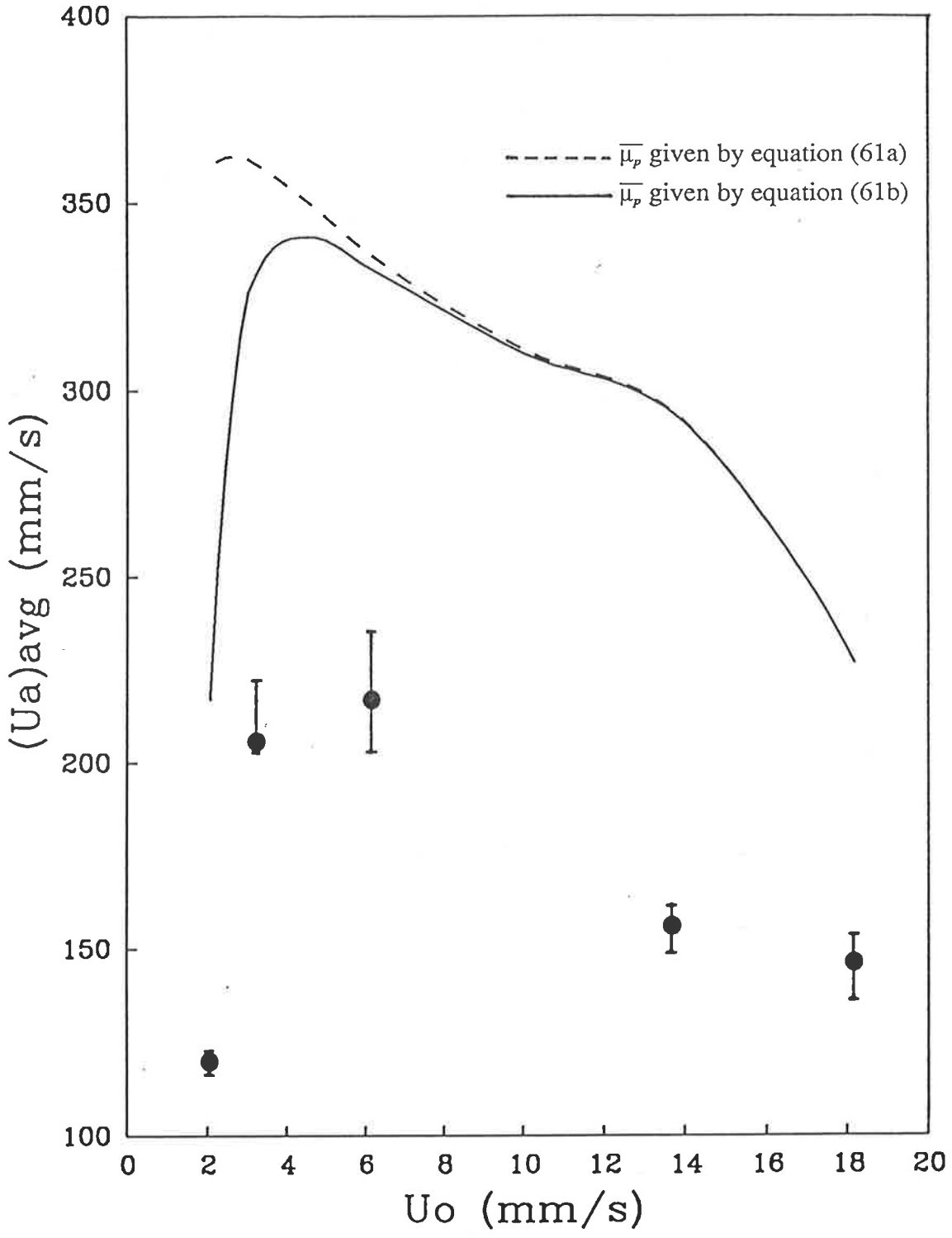

(12b) : A2 particle (12.5 mm, 1194 kg/m^3)

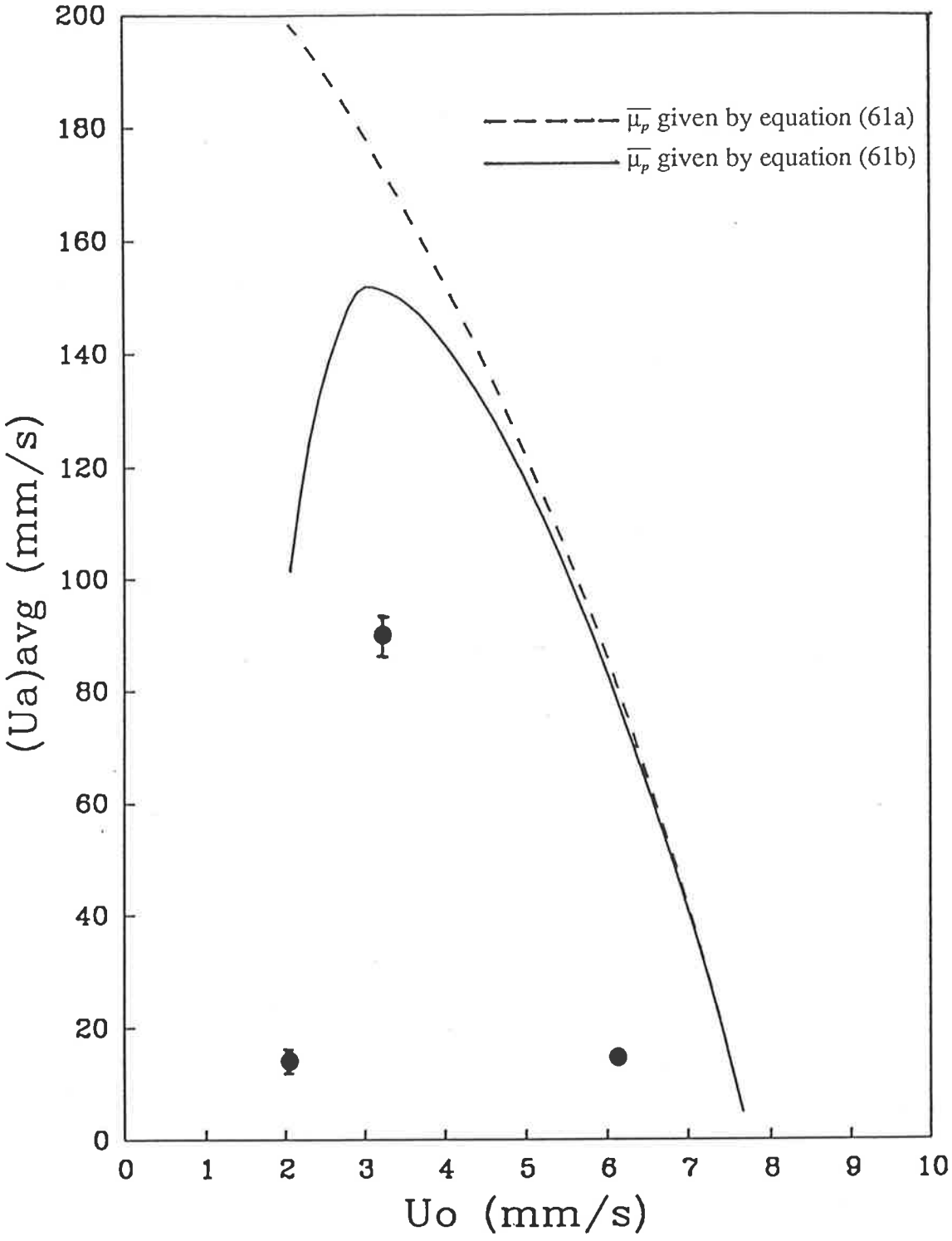

(12c) : A3 particle (12.5 mm, 1079 kg/m^3)

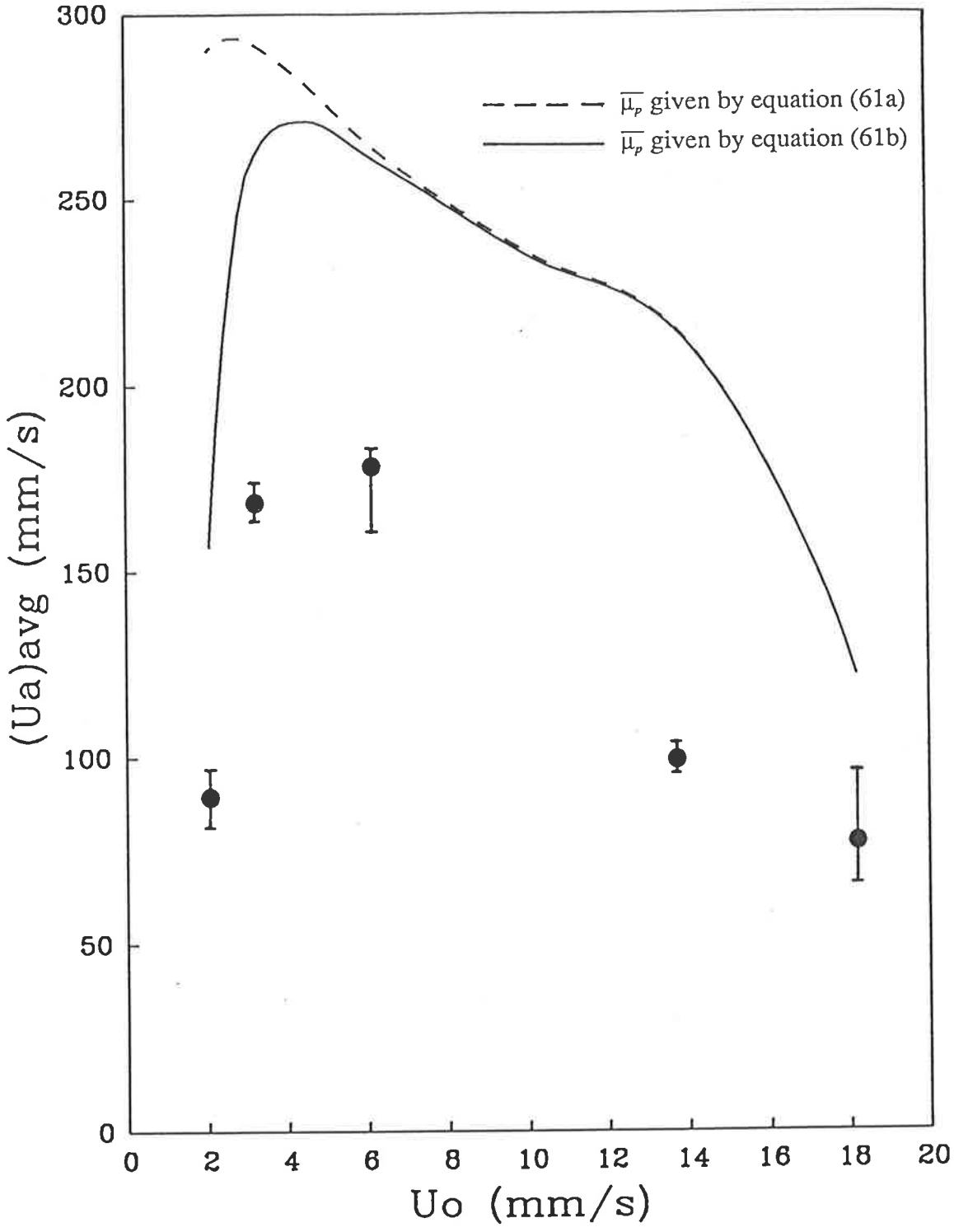

(12d) : A4 particle (11.0 mm, 1192 kg/m^3)

porosity) was reached, whereupon the active particle ascent would be slower. Ultimately, the packed bed state would be reached and the particle velocity would be expected to drop to zero. Although there is significant disagreement between model and experiment on a quantitative basis, the data trends are predicted perfectly by the numerical solution of the unsteady state model (equation 71) when $\overline{\mu_p}$, is given by the Kawase and Ulbrecht model. The less severe expression of Thomas (that is, $\overline{\mu_p}$ is not as high) also predicts these trends but with a slight lag.

This observed behaviour, which at first may seem surprising, can be rationalized by the following argument. Since the active particle is lighter than the inert particles that make up the bed, the effective weight force acting on the particle (weight plus buoyancy) will act upwards as will the fluid drag force. The downwards acting force is the the particle interaction force that opposes the upward motion of the active particle in relation to the inert particles. In the high porosity region (U_0 = 12 - 18 mm/s), the particle interaction force is small and the particle accelerates upwards relatively freely. As the velocity is decreased, both the effective weight force, W_e, (by virtue of the suspension density) and the particle interaction force, F_p, increase. The fluid drag, F_d, stays approximately constant (if anything it will probably drop slightly) since the decrease in U_0 is offset by the decrease in the effective flow channel area. Now at velocities greater than about 4 mm/s (for the system considered), the increase in F_p is offset by the increase in the buoyancy or W_e, so that the particle continues to rise faster as the fluid velocity is decreased. However, when this velocity is dropped below 4 mm/s, the active particle velocity begins to slow indicating that the particle interaction force is dominant; that is, the inert particles exhibit a large resistance to shearing that is able to negate the considerable upwards buoyancy force that exists in this porosity region.

However, despite the success of the model from a qualitative point of view the point still remains that there is a significant difference in the numerical values predicted by the model and the experimental data. To explain this deviation an additional resistance that has not yet been accounted for must be considered.

Visual observations indicate that when a large active particle was held in the fluidized bed of smaller inert particles (near the perspex walls), a defluidized cap of inert particles and fluid was formed on the top of the large particle. The effect of this cap would be two-fold:

1) it would increase the effective inertial mass of the sphere thus making its response to change more sluggish;
2) it would increase the absolute weight and effective volume of the particle.

To account for these effects, the following simplified analysis was applied.

The cap is assumed to have a density, $\rho_c (=(1-\varepsilon_{mf})\rho_i + \varepsilon_{mf}\rho)$, and mass, M_c, such that

$$M_c = f_c M_a \tag{79}$$

and f_c is expected to depend on porosity, ε, the diameter ratio, d_i/d_a, and the density ratio, ρ_a/ρ_i. Therefore, the total inertial mass, M_t, of the active particle becomes

$$M_t = M_c + M_a = (f_c + 1)M_a \tag{80a}$$

and the total volume, V_t, is

$$V_t = V_c + V_a = \left(f_c \frac{\rho_a}{\rho_c} + 1\right)V_a \tag{80b}$$

With this understanding, the modified effective weight force and effective inertial mass can be determined as

$$W_e' = \left(\left(f_c \frac{\rho_a}{\rho_c} + 1\right)\overline{\rho_s} - (f_c + 1)\rho_a\right)\frac{\pi d_a^3}{6} g = a_4' \tag{81a}$$

and

$$M_e' = \left((f_c + 1) + \frac{\varepsilon}{2}\right)\frac{\pi d_a^3}{6} \qquad (81b)$$

Substitution of these modified values in the general force balance for the active particle then allows estimates for f_c to be made, so that the numerical solution matches the experimental data. The results are presented in Table 11.

It is apparent from the Table that as the particle density increases, f_c becomes smaller (compare the A1, A2 and A3 particles in Table 11). This behaviour is expected, because as the particle becomes denser, the effect of the defluidized cap on the active particles movement becomes less significant (due to the increasing inertial mass of the sphere). Consequently, the analysis already presented for heavy particles falling through fluidized beds would not be affected by this cap. f_c is also expected to decrease as the diameter ratio, d_a/d_i drops; ultimately going to zero as the ratio reaches unity. This trend has not been predicted by the results in Table 11, mainly due to the lack of variable diameter data.

Finally, it must be pointed out that the rise appearing in the model predictions at a fluid velocity of approximately 13 mm/s in Figures 12a, b and d is not a result of some factor inherent in the model, but more a result of the dip in the experimental porosity-superficial velocity curve (given in Figure 11) at the same velocity. The use of this lower porosity produces a larger effective weight force which in turn results in a faster transit time.

3.5.3 Flotsam conditions

PARTICULATE FLUIDIZATION: In the previous analyses, all of the experimental observations followed the obvious: the heavy active particles would

TABLE 11

Defluidized Cap Coefficient, f_c (equation 79) determined from Experimental Study

Particle Type	U_0 (mm/s)	$f_c = \frac{M_c}{M_a}$
A1	18.2	-
	13.7	-
	6.1	0.195
	3.2	0.57
	2.1	4.24
A2	18.2	0.09
	13.7	0.50
	6.1	0.79
	3.2	1.85
	2.1	6.92
A3	18.2	0.26
	13.7	0.76
	6.1	1.29
	3.2	2.50
	2.1	7.56
A4	18.2	0.09
	13.7	0.51
	6.1	0.88
	3.2	1.85
	2.1	5.81

- details on each particle type are given in Table 10

sink and the light active particles would rise. The necessary flotsam condition given in equation 73 (which is sufficient since all the experiments were performed under particulate conditions) predicts this behaviour. This, unfortunately, is no great verification of the model.

Chiba et al. (1980), however, have performed experiments where, contrary to previous experience, the heavy particles (glass beads; $\rho_a = 2520\ kg/m^3$) would float in a particulate air fluidized bed of light inert particles (hollow char; $\rho_i = 1080\ kg/m^3$). Since no bubbling occurs, the necessary flotsam condition (equation 73) will be sufficient. This behaviour can be explained by considering this flotsam condition in detail. If a heavy active particle (so that a_4 is negative) is small enough, then the absolute value of a_4 (which varies as d_a^3) can be less than the value of the initial drag force, $a_1 + a_2 v^{2-n}$ (a_3 is zero from Lapple's correlation for $C_{D\infty}$), which at most varies as d_a^2. This gives rise to flotsam behaviour. The necessary flotsam condition is presented graphically in Figure 13. All the data points represent experiments with a different combination of active and inert particle sizes, different air flow rates and different bed fractions of the active particles. For points that lie above the 45° line drawn in the Figure,

$$| a_4 | > a_1 + a_2 v^{2-n} \tag{82}$$

which implies the active particles will be jetsam under the conditions considered for those particular data points. For the points that lie below this line the opposite is true and the active particles will be flotsam. The experimentally determined condition for each data point is indicated on Figure 13 as (J) for jetsam and (F) for flotsam. The model is seen to be in exact agreement with the experimental observations. No effect of the defluidized cap of spheres is considered since the d_i/d_a ratio is much greater than unity. The above can be interpreted as a more rigorous verification of the model.

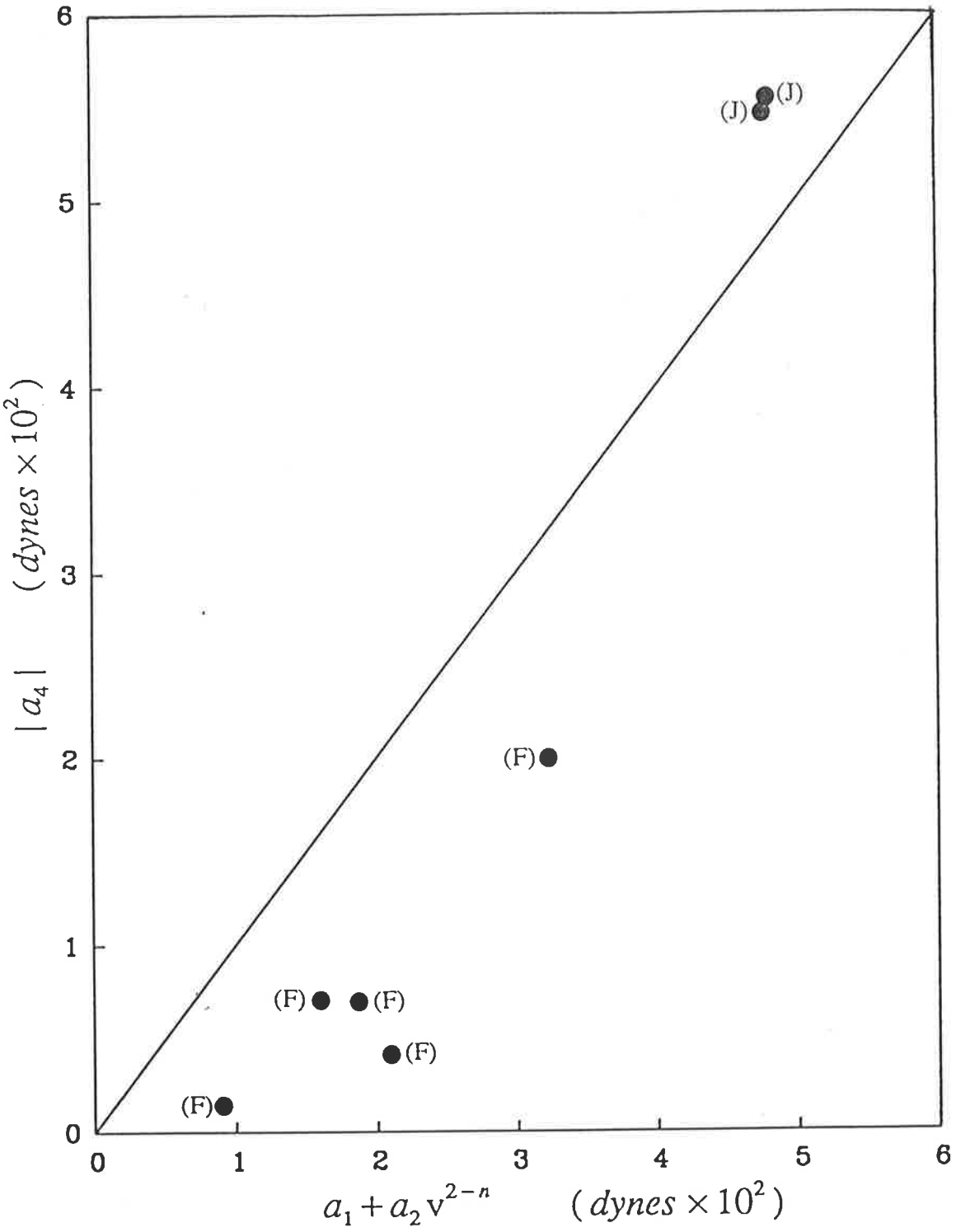

Figure 13 : Comparison of the Necessary and Sufficient Flotsam Condition (equation 73) with the Segregation Experiments of Chiba et al. (1980)

BUBBLING FLUIDIZATION: As discussed, the detailed modelling of the fluidized bed combustion of coal requires the elucidation of the mass transfer processes around large active particles in bubbling fluidized beds of smaller inert particles. To obtain experimental data for this configuration, experiments that use light napthalene spheres subliming in air fluidized beds of glass ballotini (Prins et al., 1985; Coelho and Guedes de Carvalho, 1987) as well as those that use light carbon particles burning in a hot air fluidized bed of sand particles (LaNauze et al., 1984; Prins, 1987) have been performed.

However to obtain their napthalene sublimation data, Coelho and Guedes de Carvalho (1987) had to coat steel spheres with napthalene to obtain an active particle that would sink into the bed bulk. It was claimed that if pure napthalene particles were used (as in the study of Prins et al., 1985) the active napthalene spheres would just float on the top of the bed.

The model predictions for the steady state segregation velocity, U_s, as well as the predictions for the downwards emulsion phase velocity, U_D (equation 24), are given for the sublimation and the combustion experiments described above, in Table 12a-c. The particle interaction vicosity was assumed to be in the range 0.5 to 2.0 Pa.s . The effect of the defluidized cap is not accounted for in the U_s values given.

According to the sufficient flotsam condition given in equation 76, the active particle will be flotsam if $(U_s + U_D)$ is positive; the necessary condition is no longer sufficient for the bubbling bed. In Table 12a (conditions of Prins et al., 1985) it is therefore apparent, for the range of inert and active particle sizes considered, the light napthalene spheres will have a definite tendency to float. Even allowing for the defluidized cap of inert material on the large napthalene sphere, which would at

TABLE 12a

Mass Transfer Experiments in Gas Fluidized Beds - Napthalene Sublimation data of Prins (1987)

ρ_i (kg/m^3)	d_i (mm)	U_{mf} (mm/s)	U_o/U_{mf} (mm/s)	U_D (mm/s)	d_a (mm)	$\bar{\mu}_p$ (Pa.s)	U_a (mm/s)
2800	0.098	12.0	2	-3.5	3.0	0.5	7.1
						2.0	1.8
					10.0	0.5	78.3
						2.0	19.6
					15.0	0.5	176.2
						2.0	44.1
					22.0	0.5	379.2
						2.0	94.8
2870	0.229	65.0	2	-17.3	3.0	0.5	7.0
						2.0	1.8
					10.0	0.5	77.2
						2.0	19.3
					15.0	0.5	173.5
						2.0	43.4
					20.0	0.5	308.4
						2.0	77.1
2850	0.620	360.0	2	-81.5	3.0	0.5	9.5
						2.0	2.4
					10.0	0.5	92.0
						2.0	23.1
					15.0	0.5	204.5
						2.0	51.2
					20.0	0.5	361.5
						2.0	90.6

- the active napthalene particle density equals 1015 kg/m^3

TABLE 12b

Mass Transfer Experiments in Gas Fluidized Beds - Napthalene Sublimation data of Coelho and Guedes de Carvalho (1987)

ρ_i (kg/m^3)	d_i (mm)	U_{mf} (mm/s)	U_o/U_{mf} (mm/s)	U_D (mm/s)	d_a (mm)	$\bar{\mu}_p$ (Pa.s)	U_a (mm/s)
2900	0.20	48.5	2	-13.8	5.0	0.5	6.4
						2.0	1.6
					10.0	0.5	14.3
						2.0	3.6
					15.0	0.5	25.3
						2.0	6.3
					20.0	0.5	39.5
						2.0	9.9
2900	0.46	185.0	2	-44.9	5.0	0.5	8.3
						2.0	2.1
					10.0	0.5	17.9
						2.0	4.5
					15.0	0.5	31.3
						2.0	7.8
					20.0	0.5	48.4
						2.0	12.1
2900	1.04	603.0	2	-129.5	5.0	0.5	6.7
						2.0	1.7
					10.0	0.5	10.8
						2.0	2.7
					15.0	0.5	15.8
						2.0	4.0
					20.0	0.5	21.8
						2.0	5.5

- the active napthalene particle diameter equals 1700 kg/m^3

TABLE 12c

Mass Transfer Experiments in Gas Fluidized Beds - Coke Combustion data

Reference	ρ_i (kg/m^3)	d_i (mm)	U_{mf} (mm/s)	U_o/U_{mf} (mm/s)	U_D (mm/s)	d_a (mm)	$\bar{\mu}_p$ (Pa.s)	U_a (mm/s)
	2650	0.655	19.5	2.72	-107.1	1.0	0.5	0.4
							2.0	0.1
						2.0	0.5	0.1
							2.0	0.0
						10.0	0.5	-11.2
LaNauze et al. (1984) $\rho_a = 1700\,kg/m^3$	2650	0.780	20.5	1.34	-11.26	1.0	2.0	-2.8
							0.5	0.5
							2.0	0.1
						2.0	0.5	0.2
							2.0	0.1
						10.0	0.5	-11.1
							2.0	-2.8
Prins (1987) $\rho_a = 1820\,kg/m^3$	3390	0.670	230.0	2.00	-54.6	3.0	0.5	2.1
							2.0	0.5
						10.0	0.5	16.8
							2.0	4.2
						13.0	0.5	27.9
							2.0	7.0

most decrease the segregation velocities by fifty percent, the same result would be obtained. This conclusion is in exact agreement with the observations of Coelho and Guedes de Carvalho (1987).

The conclusions from Tables 12b and c are less dramatic. For the napthalene coated steel sphere experiments of Coelho and Guedes de Carvalho (1987), the sufficient flotsam condition indicates that the majority of the data were obtained with a non-floating active particle. Those data points where ($U_a + U_D$) is positive (thus indicating a flotsam condition) are only slightly so, and allowance for the cap of defluidized inerts on the particle would be expected to make this sum negative. The carbon combustion experiments of LaNauze et al. (1984) and Prins (1987) will not have active spheres that will float since ($U_a + U_D$) is negative for all the cases considered. Allowance for the defluidized cap will make this more so.

3.6 CONCLUSIONS

Consideration of the equation of motion of an active particle in the emulsion phase of a fluidized bed, as well as identification of the relavant forces acting on the particle, allow one to infer:

1) the relative velocity between the inert bed particles and the active particle;

and 2) necessary and sufficient flotsam conditions that determine whether a particle will float or mix in a particulate or a bubbling fluidized bed.

To complete the analysis the following must be addressed:

1) The effect of the defluidized cap of inert particles on large, light active particles that rise in the emulsion must be more completely investigated. This includes correlating the parameter, f_c (defined in equation 79), in terms of the bed porosity, ε, and the size, d_a/d_i, and density, ρ_a/ρ_i, ratios.

2) For bubbling gas fluidized beds, this model for motion in the emulsion phase must be combined with studies on the motion of the particle, both in the bubble phase and between the two phases to obtain a complete description of the circulation patterns of an active particle that is different from the rest of the bed material.

NOMENCLATURE

2a	equatorial diameter of axisymmetric body, m
A_n	maximum projected area normal to the flow, m^2
a_i	coefficients defined in equation 55
A_0	area of a multiorifice distributor per hole, m^2
A_s	surface area, m^2
2b	axial length of axisymmetric body, m
B	Leveque/Levich geometry constant; defined in equation 2
b_i	coefficients defined in equations 64 and 65
c	solute concentration in solvent, kgmole m^{-3}
C_1	Kozeny factor
C_2	inertial drag factor
C_i	inertial drag coefficient
c_1	$(c - c_0)/(c_s - c_0)$, dimensionless solute concentration in solvent
c_0	inlet or upstream solute concentration in solvent, kgmole m^{-3}
c_s	saturated solute concentration at the body surface, kgmole m^{-3}
C_D	drag coefficient
$C_{D\varepsilon}$	porosity dependent drag coefficient; defined in equation 54a
C_f	principal translational resistance for axisymmetric bodies, see Table 3
d_a	active particle diameter, m
d_b	bubble diameter, m
d_i	inert particle diameter, m
d_e	equivalent.sphere diameter upon which the drag force is based (equation A.3), m
d_h	4m, hydraulic diameter, m
d_p	spherical particle diameter, m
D	diffusivity of solute in solvent, $m^2 s^{-1}$

D_t tube diameter, m

E b/a, aspect ratio of axisymmetric body

f_c M_c/M_a, defluidized cap coefficient

F_d surface average drag force, N

F_p particle-particle interaction force, N

$F_{d\varepsilon}$ porosity dependent drag force; defined in equation A.2, N

Gz_G generalized Graetz number defined in equation 17b

h heat transfer coefficient, W m^{-2} K

H_c curvature of body surface, m^{-1}

j_d $StSc^{2/3}$, Chilton-Colburn transfer factor

k fluid phase mass/heat transfer coefficient, m s^{-1}

k_c fluid phase thermal conductivity, W m^{-1} K^{-1}

k_s segregation rate constant, defined in equation 39, m s^{-1}

k_1 U_a/v ratio for use in Taylor Series expansion (Appendix D)

K $Sh^{\infty}_{spheroid}/Sh^{\infty}_{p}$

K_d drag geometry constant, defined in equation 1

K_1 parameter that defines the viscous component of the drag coefficient

K_2 parameter in equation 31a for viscous flow analysis (Chapter 2); coefficient defined in equation 54c for particle motion analysis (Chapter 3)

K_3 variable defined in equation 34a

K_4 parameter in equation 34b

K_5 parameter in equation 34c

l co-ordinate length, m

L bed height or plate length, m

L_e total flow length of the channel, m

L_f fluid flow length over or through a body, m

m hydraúlic radius, m

M_e effective inertial mass of a particle, kg

M_c mass of defluidized cap of particles, kg

N $L(1-\varepsilon)/V_p$, number of particles in a unit cross-section of the assemblage, m^{-2}

N_f effective drag factor for different conduits, see Table 1

Nu_{d_h} $(hd_h)/k_c$, Nusselt number based on the hydraulic diameter

Nu_G $(h(3m/z))/k_c$, generalized Nusselt number

Nu_L hL/k_c, Nusselt number for the flat plate geometry

ΔP pressure loss, Pa

Pe $(Ud_p)/D$, Peclet number

Pr Prandtl number

P_w local wetted perimeter, m

q tortuosity factor

r polar radius; defined in Figure B.1, m

Re_{d_h} $\overline{U}d_h/\nu$, Reynolds number based on the hydraulic diameter

Re_a Ud_a/ν, Reynolds number based on active particle diameter

Re_G generalized Reynolds number defined in equation 4

Re_L $\overline{U}L/\nu$, Reynolds number for the flat plate

Re_p Ud_p/ν, Reynolds number based on a sphere diameter

Re_s Ud_e/ν, Reynolds number based on an equivalent sphere diameter

Re_ε $Re_p q/(2z(1-\varepsilon))$, multi-particle Reynolds number

R_D parameter defined in equation 38b

Sc Schmidt number

Sh $(k(2a))/D$, Sherwood number based on the equatorial diameter

Sh_p kd_p/D, Sherwood number based on particle diameter

Sh_G generalized Sherwood number defined in equation 17a

St $k/\overline{U}$, Stanton number

t time, s

u tangential velocity component in the x direction, m s^{-1}

u_0' $(du/dy)_{y=0}$, tangential velocity gradient at the surface, s^{-1}

U_0 superficial velocity, m s^{-1}

$\overline{U}$ average approach velocity of the fluid, m s^{-1}

U_a segregation velocity of the active particle with respect to the inert particles, m s^{-1}

$(U_a)_w$ segregation velocity of the active particle with respect to the inert particles in the presence of significant wall effects, m s^{-1}

U_b bubble rise velocity, m s^{-1}

U_D convective velocity of emulsion solids in bubbling fluidized beds, m s^{-1}

U_{mf} minimum fluidization velocity, m s^{-1}

v normal velocity component in the y direction, in the viscous flow analysis, m s^{-1} (Chapter 2); qU_0/ε, interstitial fluid velocity in the particle motion analysis, m s^{-1} (Chapter 3)

V_p particle volume, m^3

W_e effective weight force acting on a particle, N

W_b effective buoyancy force acting on a particle, N

x_J volume fraction of jetsam particles

x position along the flow path on the surface; defined in Figure B.1, m

y distance from the surface in the direction normal to the flow path; defined in Figure B.1, m

$\bar{y}$ average segregation displacement; defined in equation 40

z cross-section factor

Greek symbols

α wake fraction in a bubble

ν fluid phase kinematic viscosity, $m^2 s^{-1}$

ε bed voidage

ε_b bubble fraction

β dummy variable used in equation B.14

χ variable defined in equation B.12b, $m^{9/2} s^{3/2}$

η variable defined in equation B.6c, $m^{3/2} s^{1/2}$

Γ gamma function

μ fluid phase viscosity, kg $m^{-1} s^{-1}$

$\overline{\mu_s}$ suspension viscosity, kg $m^{-1} s^{-1}$

$\overline{\mu_p}$ particle-particle interaction viscosity; defined in equation 59b, kg $m^{-1} s^{-1}$

ϕ generalized drag factor; defined in equation 7

ϕ_s solids volume fraction

ρ fluid density, kg m^{-3}

ρ_c defluidized cap density; defined in equation 79, kg m^{-3}

$\overline{\rho_a}$ active particle density, kg m^{-3}

$\overline{\rho_i}$ inert particle density, kg m^{-3}

$\overline{\rho_s}$ suspension density, kg m^{-3}

σ standard deviation of the error, %

ζ $\{\eta/(9\chi)\}^{1/3}$, variable

Subscripts

a active particle

i inert particle

F flotsam particle

J jetsam particle

m surface average

x peripheral average

∞ isolated particle in infinite fluid conditions

Superscripts

0 $Gz_G \rightarrow 0$ solution

∞ $Gz_G \rightarrow \infty$ solution

LITERATURE CITED

Agarwal, P.K. and O'Neill, B.K., Chem.Eng.Sci. (in press), 1988.

Agarwal, P.K., Chem.Eng.Sci. (in press), 1988.

Agarwal, P.K., Mitchell, W.J. and LaNauze, R.D., Chem.Eng.Sci. (in press), 1988.

Andersson, K.E.B., Chem.Eng.Sci., 1961, 15, 276-297.

Andersson, K.E.B., Trans.Royal.Inst.Tech.Stockholm, No. 201, 1963.

Andersson, K.E.B., Hatcher, M. and Stelling, O., Trans.Royal.Inst.Tech.Stockholm, No. 222, 1964.

Arastoopour, H., Wang, C-H., Weil, S.A., Chem.Eng.Sci., 1982, 37, 1379-1386.

Arastoopour, H., Lin, D.H., Gidaspow, D., 'Multiphase Transport- Vol. 4', Hemisphere, Washington, 1980.

Bassett, A.B., 'A Treatise on Hydrodynamics - Vol. 2', Deighton Bell, Cambridge, 1888 (republished: Dover Publications, New York, 1961)

Barnea, E. and Mizrahi, J., Chem.Eng.J., 1973, 5, 171-189.

Beeckmans, J.M., Nilsson, J., Large, J-F., Ind.Eng.Chem.Fund., 1985, 24, 90-95.

Carman, P.C., 'Flow of Gases Through Porous Media', Butterworths, London, 1956.

Cheng, D.C.H., Chem.and.Ind, 1980a, 403-406.

Cheng, D.C.H., Chem.and.Ind, 1980b, 407-414.

Chiba, S., Nienow, A.W., Chiba, T., Kobayashi, H. Powd.Tech., 1980, 26, 1-10.

Churchill, S.W. and Ozoe, H., Trans.A.S.M.E., 1973, 416-419.

Coelho, M.A.N., and Guedes de Carvalho, J.R.F., Chem.Eng.Res.Des., 1987 (in press).

Clift, R., Grace J.R. and Weber, M.E., 'Bubbles, Drops and Particles', Academic Press, New York, 1978.

Clift, R., Seville, J.P.K., Moore, S.C., Chavarie, C., Chem.Eng.Sci., 1987, 42, 191-194.

Daniels, T.C., J.Mech.Eng.Sci, 1962, 4, 103-110.

Darton, R.C., LaNauze, R.D., Davidson, J.F., Harrison, D., Trans.I.Chem.E., 1977, 55, 274-280.

Davidson, J.F. and Harrison, D., 'Fluidized Particles', Cambridge University Press, Cambridge, 1963.

Davies, S.J. and White, C.M., Engg., 1929, 128, 69-

Doss, E.D., Int.J.Multiphase.Flow., 1985, to be published.

Einstein, A., Ann.Physik., 1906, 19, 289-

Epstein, N., Chem.Eng.Sci., 1984, 39, 1533-1534.

Ergun, S., Chem.Eng.Prog., 1952, 48, 89-94.

Foscolo, P.U., Gibilaro, L.G., Waldram, S.P., Chem.Eng.Sci., 1983, 38, 1251-1260.

Frankel, N.A.and Acrivos, A., Chem.Eng.Sci., 1984, 22, 847-851.

Gibilaro, L.G., and Rowe, P.N., Chem.Eng.Sci, 1974, 29, 1403-1412.

Gibilaro, L.G., Waldram, S.P., Foscolo, P.U., Chem.Eng.Sci., 1984, 39, 1533-1534.

Gibilaro, L.G., Hossain, I., Waldram, S.P., Chem.Eng.Sci., 1985, 40, 2333-2338.

Gibilaro, L.G., DiFelice, R., Waldram, S.P., Foscolo, P.U., Chem.Eng.Sci., 1987, 42, 194-196.

Goldstein, S. (ed), 'Modern Developments in Fluid Dynamics:An Account of Theory and Experiment Relating to Boundary Layers, Turbulent Motion and Wakes, Volume 1', Dover Publications, New York, 1965.

Grace, J.R., Can.J.Chem.Eng., 1970, 48, 30-34.

Hagyard, T. and Sacerdote, A.M., Ind.Eng.Chem.Fund., 1966, 5, 500-508.

Happel, J. and Brenner, H., 'Low Reynolds Number Hydrodynamics', Martinus Nijhoff Publishers, Dordrecht, 1983.

Hawksley, P.G.W., 'Some Aspects of Fluid Flow', Inst.Phys., Arnold, London, 1951, 114-135.

Jakob, M., 'Heat Transfer, Volume 1', John Wiley and Sons, New York, 1949.

James, P.A., Can.J.Chem.Eng., 1970, 48, 330-332.

Jinescu, V.V., Int.Chem.Eng., 1974, 14, 397-420.

Joshi, J.B., Chem.Eng.Res.Des., 1983, 61, 143-161.

Karabelas, A.J., Wegner, T.H. and Hanratty, T.J., Chem.Eng.Sci., 1971, 26, 1581-1589.

Kawase, Y. and Ulbrecht, J.J., Chem.Eng.Commun., 1983, 20, 127-136.

Kawase, Y. and Ulbrecht, J.J., Ind.Eng.Chem.Fundam., 1985, 24, 115-116.

Kennedy, S.C. and Bretton, R.H., Chem.Eng.Sci, 1966, 12, 24-28.

King, D.F., Mitchell, F.R.G., Harrison, D., Powd.Tech., 1981, 28, 55-58.

Kunii, D. and Levenspiel, O., 'Fluidization Engineering', John Wiley, New York, 1969.

Kramers, H., Physica, 1946, 12, 61-80.

Krishnamurty, V.V.G., Indian.J.Tech., 1967, 5, 167-168

Krishnamurty, V.V.G. and Sambasiva Rao, N.V., Indian.J.Tech., 1967, 5, 331-333.

LaNauze, R.D., Jung, K., Kastl, J., Chem.Eng.Sci., 1984, 39, 1623-1633.

LaNauze, R.D., Chem.Eng.Res.Des., 1985, 63, 3-33.

Leveque, M.A., Ann.Mines.Mem.Ser., 1928, 13, 201-209.

Levich, V.G., 'Physicochemical Hydrodynamics', Prentice-Hall, New York, 1962.

Lewis, W.K., Gilliland, E.R. and Bauer, W.C., Ind.Eng.Chem., 1949, 41(6), 1104-1117.

Lochiel, A.C. and Calderbank, P.H., Chem.Eng.Sci, 1964, 19, 471-484.

Martin, B.L.A., Kolar, Z., Wesselingh, J.A., Trans.I.Chem.E., 1981, 59, 100-104.

Murray, J.D., Rheol.Acta, 1967, 6, 27-

Molerus, O., Chem.Eng.Sci, 1980, 35, 1331-1340.

Naimer, N.S., Chiba, T., Nienow, A.W., Chem.Eng.Sci., 1982, 37, 1047-1057.

Nienow, A.W., Rowe, P.N., Cheung, L.Y., Powd.Tech., 1978a, 20, 89-97.

Nienow, A.W., Rowe, P.N., Chiba, T., AIChE.Symp.Ser.74, 1978b, 176, 45-53.

Oliver, D.R. and Rao, S.S., Trans.I.Chem.E., 1979, 57, 104-112.

Porter, J.E., Trans.I.Chem.E., 1971, 49, 1-29.

Prins, W., Casteleijn, T.P., Draijer, W., Swaaij, W.P.M., Chem.Eng.Sci., 1985, 40, 481-497.

Prins, W., PhD Thesis, 1987, Twente University.

Prudhoe, J. and Whitmore, R.L., Brit.Chem.Eng., 1964, 9, 371-375.

Rao, S.S., Pattabhi Ramacharyulu, N.Ch. and Krishnamurty, V.V.G., Appl.Sci.Res., 1969, 21, 185-193.

Reed, C.C. and Anderson, J.L., AIChE.J., 1980, 26, 816-827.

Reitema, K., Chem.Eng.Sci., 1982, 37, 1125-1150.

Richardson, J.F. and Zaki, W.N., Trans.I.Chem.E., 1954, 39, 35-53.

Richardson, J.F. and Meikle, R.A., Trans.I.Chem.E., 1961, 39, 357-

Richardson, S.M., Lett.Heat.Mass.Transfer, 1980, 7(5), 353-362.

Rowe, P.N. and Claxton, K.T., Trans.I.Chem.E., 1965, 43, 321-331.

Rowe, P.N., Nienow, A.W., Agbim, A.J., Trans.I.Chem.E., 1972, 50, 310-323.

Rutgers, R., Rheol.Acta., 1962, 2, 305-

Saxton, J.A., Fitton, J.B., Vermuelen, T., AIChE.J., 1970, 16, 120-130.

Schugerl, K., Merz, M., Fetting, F., Chem.Eng.Sci., 1961, 15, 39-

Scheidegger, A.E., 'The Physics of Flow Through Porous Media', Macmillan, New York, 1960.

Sehlin, R.C., M.S. Thesis, Carnegie-Mellon University, Pittsburgh, Pennsylvania, 1969.

Shah, R.K. and London, A.L., 'Laminar Flow Forced Convection in Ducts', Academic Press, New York, 1978.

Srinivasan, M.G., Doss, E.D., Chem.Eng.Sci., 1985, 9, 1791-1792.

Stewart, W., Trans.I.Chem.E., 1968, 46, 60-

Tanimoto, H., Chiba, S., Chiba, T., Koboyashi, H., J.Chem.Eng.Japan, 1981, 14, 273-

Thomas, D.G., J.Colloid.Sci., 1965, 20, 267-

Valenzuela, J.A. and Glicksman, L.R., Powd.Tech., 1985, 44, 103-113.

Wen, C.Y. and Yu, Y.H., Chem.Eng.Prog.Symp.Ser.62, 1966, 62, 100-111.

Wilhelm, R.H. and Kwauk, M., Chem.Eng.Prog., 1948, 44(3), 201-218.

Williamson, J.E., Bazaire, K.E. and Geankoplis, C.J., Ind.Eng.Chem.Fundam., 1963, 2(2), 126-129.

Wilson, E.J. and Geankoplis, C.J., Ind.Eng.Chem.Fundam., 1966, 5(1), 9-14.

Young, R.J., J.Appl.Chem., 1952, 2, S51-S61.

APPENDICES

APPENDIX A

Derivation of the m/z factor for external flow over axisymmetric bodies

From equation 3, the drag force on a body of any shape in the viscous flow regime can be written as

$$F_d = \phi A_s \frac{\rho \overline{U}^2}{2} \qquad (A.1)$$

where A_s is the surface area and $\overline{U}$ is the approach velocity. Using the conventional definition of the drag coefficient we can write

$$F_d = C_D A_n \frac{\rho \overline{U}^2}{2} \qquad (A.2)$$

where A_n is a projected area normal to the flow. Values of the drag coefficient for axisymmetric bodies are available in the literature (Clift et al., 1978; Happel and Brenner, 1983) in terms of an equivalent sphere with diameter, d_e as

$$C_D = \frac{K_1}{Re_s} \qquad (A.3)$$

where $Re_s = \overline{U} d_e / \nu$ and A_n, in equation A.2, is the maximum equivalent sphere area normal to the flow i.e. $(\pi d_e^2)/4$. K_1 is a parameter which depends on the orientation of the body with respect to the flow direction and the basis upon which the equivalent sphere diameter is defined. It may be noted however, that the $(d_e K_1)$ product is independent of this basis.

Consequently, equating equations A.1 and A.2 and using equation A.3 gives the (m/z) factor for a general axisymmetric body

$$\frac{m}{z} = \frac{8}{\pi} \frac{A_s}{K_1 d_e} \tag{A.4}$$

Values of (m/z) for different body and flow geometries are summarized in Table 1. The method used is illustrated below for a prolate spheroid.

Happel and Brenner (1983) present the drag force on a prolate spheroid (equatorial radius a, axial radius b) in terms of the drag on a sphere with an equivalent equitorial radius (i.e. $d_e = 2a$) as

$$(C_D)_{\substack{prolate \\ spheroid}} = \frac{4.8(4+E)}{Re_s} \tag{A.5}$$

where E (= b/a) is the aspect ratio. Thus by comparison with equation A.3

$$K_1 = 4.8(4+E) \tag{A.6}$$

For a prolate spheroid

$$A_s = 2\pi a^2 \left(\frac{E^2}{\sqrt{E^2-1}} \sin^{-1}\left(\sqrt{\frac{E^2-1}{E}} \right) + 1 \right) \tag{A.7}$$

Using equations A.6 and A.7 in equation A.4 then gives

$$\left(\frac{m}{z} \right)_{\substack{prolate \\ spheroid}} = \frac{8a}{4.8(4+E)} \left(\frac{E^2}{\sqrt{E^2-1}} \sin^{-1}\left(\sqrt{\frac{E^2-1}{E}} \right) + 1 \right) \tag{A.8}$$

APPENDIX B

Derivation of the dimensionless concentration gradient at the surface

The boundary layer equation for species conservation in flow through conduits and over axisymmetric bodies with low curvature, and the flat plate can be reduced to

$$u\frac{\partial c}{\partial x}+\mathrm{v}\frac{\partial c}{\partial y}=D\frac{\partial^2 c}{\partial y^2} \qquad (B.1)$$

The coordinate systems are shown, for each of the above geometries, in Figure B.1. For configuration (a) in Figure B.1, the continuity equation is

$$\frac{\partial}{\partial x}(ru)+\frac{\partial}{\partial y}(r\,\mathrm{v})=0 \qquad (B.2)$$

and for configuration (b) we have (Goldstein, 1965)

$$\frac{\partial u}{\partial x}+\frac{1}{(1-H_c y)}\frac{\partial}{\partial y}((1-H_c y)\mathrm{v})=0 \qquad (B.3)$$

where H_c is the body curvature. In the thin concentration boundary layer however $(1-H_c y)\sim 1$ and so the continuity equation for conduits reduces to that for the flat plate (configuration c)

$$\frac{\partial u}{\partial x}+\frac{\partial \mathrm{v}}{\partial y}=0 \qquad (B.4)$$

Hence, equation B.2 can represent the continuity equation for all three geometries with $r=1$ for conduits and flat plates.

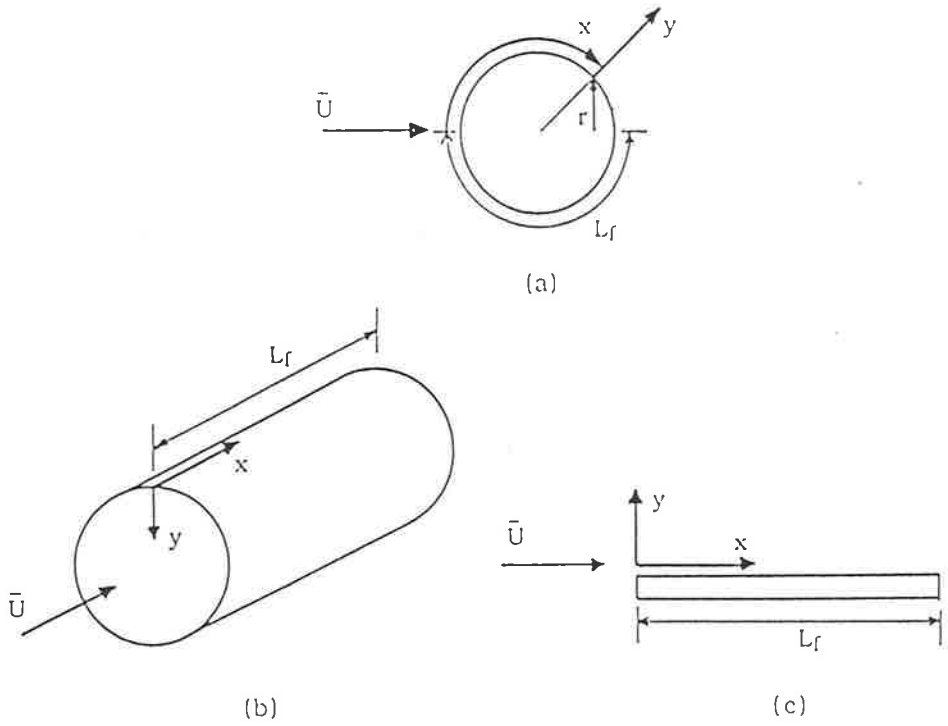

Figure B.1 : Co-ordinate Systems used for flow:
(a) over axisymmetric bodies;
(b) through conduits;
and (c) over flat plates

In the thin concentration boundary layer limit, the mass transfer processes will occur in a layer of fluid in which the tangential velocity gradient may be considered as constant

$$u = u_0' y \tag{B.5}$$

Substitution of this expression into equation B.2 and integration yields

$$v = -\frac{1}{r}\frac{\partial}{\partial x}\left(\frac{u_0' y^2 r}{2}\right) \tag{B.6a}$$

$$= -\frac{1}{r}\frac{\partial}{\partial x}\left(\frac{\eta^2}{2}\right) \tag{B.6b}$$

where

$$\eta = y(u_0' r)^{1/2} \tag{B.6c}$$

The dimensionless concentration is defined as

$$c_1 = \frac{c - c_0}{c_s - c_0} \tag{B.7}$$

Using this definition along with equations B.5 and B.6 reduces the species boundary layer equation B.1 to

$$(u_0' y)\frac{\partial c_1}{\partial x} - \frac{\eta}{r}\frac{\partial \eta}{\partial x}\frac{\partial c_1}{\partial y} = D\frac{\partial^2 c_1}{\partial y^2} \tag{B.8}$$

For a fixed set of flow conditions, we have

$$c_1 = c_1(x,y) \tag{B.9a}$$

$$\eta = \eta(x,y) \tag{B.9b}$$

so, alternatively, we may write

$$c_1 = c_1(x,\eta) \tag{B.9c}$$

Using the definition of the total differential then allows the partial derivatives in equation B.8 to be determined as

$$\frac{\partial c_1}{\partial y} = \frac{\partial c_1}{\partial \eta}\frac{\partial \eta}{\partial y} \qquad (B.10a)$$

$$\frac{\partial c_1}{\partial \eta}\frac{\partial \eta}{\partial x} = 0 \qquad (B.10b)$$

and

$$\frac{\partial^2 c_1}{\partial y^2} = \frac{\partial^2 c_1}{\partial \eta^2}\left(\frac{\partial \eta}{\partial y}\right)^2 \qquad (B.10c)$$

These equations further reduce equation B.1 to

$$(u_0' y)\frac{\partial c_1}{\partial x} = D\frac{\partial^2 c_1}{\partial \eta^2}\left(\frac{\partial \eta}{\partial y}\right)^2 \qquad (B.11)$$

and noting that

$$\left(\frac{\partial \eta}{\partial y}\right)^2 = u_0' r \qquad (B.12a)$$

as well as defining

$$d\chi = \frac{D\,(u_0' r)^{3/2}}{u_0'}dx \qquad (B.12b)$$

gives equation B.11 in the standard form

$$\eta\frac{\partial c_1}{\partial \chi} = \frac{\partial^2 c_1}{\partial \eta^2} \qquad (B.13)$$

With the boundary conditions $c_1 = 1$ at $y = 0$ and $c_1 = 0$ at $y \to \infty$, the general solution obtained is

$$c_1 = 1 - \frac{\int_0^{\zeta} \exp(-\beta^3)d\beta}{\Gamma(4/3)} \qquad (B.14)$$

where $\zeta = \eta/(9\chi)^{1/3}$ leading to

$$\left(\frac{\partial c_1}{\partial y}\right)_{y=0} = -\frac{1}{\Gamma(4/3)}\frac{(u_0' r)^{1/2}}{(9\chi)^{1/3}} \qquad (B.15)$$

Note that for conduits and flat plates the above expressions are independent of r as r is taken as 1 (equation B.4).

APPENDIX C

Comparison of model with literature data for ducts for all Graetz number conditions

The literature data used in the following tables are taken from the numerical computations of Shah and London (1978).

TABLE C.1

Comparison for Rectangular Ducts

$Re_{d_h} Pr(d_h/x)$	Surface average Nusselt number, $Nu_{d_h,m}$		Peripheral average Nusselt number, $Nu_{d_h,x}$	
	Literature Results	This Theory (equation 34b)	Literature Results	This Theory (equation 34c)
aspect ratio = 1.00				
0	2.65	2.65	2.65	2.65
10	3.50	3.40	2.86	2.89
20	4.03	3.96	3.08	3.10
30	4.47	4.42	3.24	3.30
40	4.85	4.80	3.43	3.48
60	5.50	5.46	3.78	3.80
80	6.03	6.00	4.10	4.09
100	6.46	6.47	4.35	4.35
120	6.86	6.89	4.62	4.58
140	7.22	7.27	4.85	4.80
160	7.56	7.61	5.03	5.00
180	7.87	7.93	5.24	5.19
200	8.15	8.23	5.41	5.37
aspect ratio = 0.500				
0	3.39	3.39	3.39	3.39
10	3.95	3.98	3.43	3.56
20	4.46	4.46	3.54	3.72
30	4.86	4.87	3.70	3.87
40	5.24	5.23	3.85	4.01
60	5.85	5.85	4.16	4.27
80	6.37	6.37	4.46	4.51
100	6.84	6.83	4.72	4.74
120	7.24	7.24	4.93	4.94
140	7.62	7.62	5.15	5.14
160	7.97	7.96	5.34	5.32
180	8.29	8.28	5.54	5.50
200	8.58	8.58	5.72	5.66
aspect ratio = 0.333				
0	3.96	3.96	3.96	3.96
10	4.54	4.52	4.02	4.11
20	5.00	4.98	4.17	4.26

TABLE C.1 (continued)

$Re_{d_h} Pr(d_h/x)$	Surface average Nusselt number, $Nu_{d_h,m}$		Peripheral average Nusselt number, $Nu_{d_h,x}$	
	Literature Results	This Theory (equation 34b)	Literature Results	This Theory (equation 34c)
30	5.39	5.38	4.29	4.40
40	5.74	5.74	4.42	4.53
60	6.35	6.35	4.67	4.78
80	6.89	6.89	4.94	5.01
100	7.33	7.34	5.17	5.22
120	7.74	7.76	5.42	5.42
140	8.11	8.14	5.62	5.61
160	8.45	8.49	5.80	5.79
180	8.77	8.81	5.99	5.96
200	9.07	9.12	6.18	6.13
aspect ratio = 0.250				
0	4.51	4.51	4.51	4.51
10	5.00	5.01	4.53	4.64
20	5.44	5.44	4.65	4.76
30	5.81	5.82	4.76	4.88
40	6.16	6.15	4.87	4.99
60	6.73	6.75	5.08	5.22
80	7.24	7.26	5.32	5.42
100	7.71	7.72	5.55	5.61
120	8.13	8.13	5.77	5.79
140	8.50	8.51	5.98	5.97
160	8.86	8.86	6.18	6.14
180	9.17	9.18	6.37	6.30
200	9.47	9.49	6.57	6.45
aspect ratio = 0.167				
0	5.22	5.22	5.22	5.22
10	5.66	5.65	5.24	5.32
20	6.04	6.04	5.34	5.42
30	6.37	6.37	5.41	5.52
40	6.70	6.69	5.48	5.62
60	7.26	7.26	5.64	5.80
80	7.77	7.75	5.86	5.97
100	8.17	8.19	6.07	6.14
120	8.63	8.59	6.27	6.30

TABLE C.1 (continued)

$Re_{d_h} Pr(d_h/x)$	Surface average Nusselt number, $Nu_{d_h,m}$		Peripheral average Nusselt number, $Nu_{d_h,x}$	
	Literature Results	This Theory (equation 34b)	Literature Results	This Theory (equation 34c)
140	9.00	8.96	6.47	6.46
160	9.35	9.31	6.66	6.60
180	9.67	9.63	6.86	6.75
200	10.01	9.94	7.02	6.89

TABLE C.2

Comparison for Parallel Plates (aspect ratio, E = 0.000)

$Re_{d_h} Pr(d_h/x)$	Surface average Nusselt number, $Nu_{d_h,m}$		Peripheral average Nusselt number, $Nu_{d_h,x}$	
	Literature Results	This Theory (equation 34b)	Literature Results	This Theory (equation 34c)
1000000	184.548	184.542	122.943	122.964
500000	146.425	146.401	97.538	97.531
200000	107.833	107.783	71.83	71.787
142857	96.375	96.314	64.200	64.143
100000	85.557	85.484	56.999	56.927
50000	67.890	67.793	45.245	45.149
20000	50.027	49.895	33.379	33.259
14285.7	44.731	44.586	29.867	29.744
10000	39.736	39.579	26.560	26.438
5000	31.598	31.421	21.188	21.090
2000	23.416	23.235	15.830	15.830
1428.57	21.009	20.837	14.270	14.333
1000	18.752	18.599	12.822	12.970
500	15.125	15.043	10.545	10.909
200	11.623	11.708	8.517	9.180
142.857	10.662	10.817	8.053	8.770
100	9.825	10.042	7.741	8.437
50	8.713	8.959	7.550	8.013
20	8.010	8.165	7.541	7.736
14.2857	7.876	7.996	7.541	7.681
10	7.775	7.865	7.541	7.639
5	7.658	7.706	7.541	7.590
0	7.541	7.540	7.541	7.541

TABLE C.3

Comparison for Triangular Ducts

$Re_{d_h} Pr(d_h/x)$	Surface average Nusselt number, $Nu_{d_h,m}$		Peripheral average Nusselt number, $Nu_{d_h,x}$	
	Literature Results	This Theory (equation 34b)	Literature Results	This Theory (equation 34c)
aspect ratio = 1.000 (equilateral triangle)				
0	2.47	2.47	2.47	2.47
10	3.10	3.10	2.57	2.68
20	3.66	3.59	2.73	2.86
30	4.07	4.00	2.9	3.04
40	4.43	4.36	3.08	3.20
50	4.75	4.68	3.26	3.35
60	5.02	4.97	3.44	3.49
80	5.49	5.48	3.73	3.75
100	5.93	5.93	4.00	3.99
120	6.29	6.33	4.24	4.21
140	6.61	6.69	4.47	4.41
160	6.92	7.02	4.67	4.60
180	7.18	7.33	4.85	4.78
200	7.42	7.62	5.03	4.95
aspect ratio = 0.866 (right-angled isoceles triangle)				
0	2.34	2.34	2.34	2.34
10	2.87	2.85	2.40	2.50
20	3.33	3.27	2.53	2.66
30	3.70	3.64	2.70	2.80
40	4.01	3.96	2.90	2.94
50	4.28	4.26	3.05	3.06
60	4.52	4.53	3.20	3.19
80	4.91	5.01	3.50	3.42
100	5.23	5.43	3.77	3.63
120	5.52	5.81	4.01	3.83
140	5.78	6.16	4.21	4.01
160	6.00	6.48	4.40	4.19
180	6.17	6.78	4.57	4.35
200	6.33	7.06	4.74	4.51

TABLE C.4

Comparison for Circular Ducts (aspect ratio, E = 1.000)

$Re_{d_h} Pr(d_h/x)$	Surface average Nusselt number, $Nu_{d_h,m}$		Peripheral average Nusselt number, $Nu_{d_h,x}$	
	Literature Results	This Theory (equation 34b)	Literature Results	This Theory (equation 34c)
1000000	160.358	160.080	106.538	106.284
500000	127.051	126.759	84.341	84.063
200000	93.334	93.023	61.877	61.565
142857	83.332	83.000	55.208	54.884
100000	73.869	73.536	48.914	48.575
50000	58.429	58.075	38.637	38.270
20000	42.813	42.424	28.254	27.849
14285.7	38.181	37.778	25.178	24.760
10000	33.815	33.392	22.275	21.847
5000	26.685	26.235	17.558	17.107
2000	19.501	19.014	12.824	12.365
1428.57	17.379	16.881	11.433	10.982
1000	15.384	14.877	10.130	9.697
500	12.152	11.640	8.036	7.673
200	8.943	8.474	6.002	5.817
142.857	8.014	7.580	5.430	5.334
100	7.155	6.771	4.916	4.920
50	5.814	5.559	4.172	4.357
20	4.640	4.565	3.710	3.960
14.2857	4.367	4.334	3.669	3.876
10	4.116	4.148	3.658	3.812
5	3.906	3.914	3.657	3.736
0	3.657	3.657	3.657	3.657

APPENDIX D

Taylor Series Expansion of the Non-Linear Term in the General Equation of Motion (equation 63)

Only the low velocity case ($v - U_a > 0$) will be considered in detail here; the argument is the same for the high velocity model.

The Taylor series to the second for a general function, $f(x)$ about the point x equal to x_0 can be written as

$$f(x) = f(x_0) + \left(\frac{\partial f}{\partial x}\right)_{x_0}(x - x_0) + \frac{1}{2}\left(\frac{\partial^2 f}{\partial x^2}\right)_{x_0}(x - x_0)^2 \qquad (D.1)$$

Putting $x = v - U_a$ and $f(x) = x^{2-n}$ and noting that $x_0 = (1 - k_1)v$ (since $U_{a0} = k_1 v$) gives

$$\left(\frac{\partial f}{\partial x}\right)_{x_0} = (2-n)(1-k_1)^{1-n} v^{1-n} \qquad (D.2a)$$

$$\left(\frac{\partial^2 f}{\partial x^2}\right)_{x_0} = (2-n)(1-n)(1-k_1)^{-n} v^{-n} \qquad (D.2b)$$

and

$$x - x_0 = (k_1 v - U_a) \qquad (D.2c)$$

Equation D.1 now becomes

$$(v - U_a)^{2-n} = (1-k_1)^{2-n} v^{2-n} + (2-n)(1-k_1)^{1-n} v^{1-n}(k_1 v - U_a) + \frac{(2-n)(1-n)}{2}(1-k_1)^{-n} v^{-n}(k_1 v - U_a)^2 \qquad (D.3)$$

Manipulation yields

$$(v - U_a)^{2-n} = \left((1-k_1)^{2-n} + (2-n)(1-k_1)^{1-n} k_1 + \frac{(2-n)(1-n)}{2}(1-k_1)^{-n} k_1^2 \right) v^{2-n} - \left((2-n)(1-k_1)^{1-n} + (2-n)(1-n)(1-k_1)^{-n} k_1 \right) v^{1-n} U_a$$

$$+\left(\frac{(2-n)(1-n)}{2}(1-k_1)^{-n}\right)\nu^{-n}\,U_a^2 \qquad (D.4a)$$

$$=b_1-b_2U_a+b_3U_a^2 \qquad (D.4b)$$

The b_i coefficients for both cases are tabulated in Table 9.

APPENDIX E

Experimental data

The data presented in the following tables are the raw experimental times that each active particle took to rise a height of 280 mm in the liquid fluidized bed. Details of the experimental system and technique are given in section 3.3. Details of the active particle types are given in Table 10.

TABLE E.1

Raw Data for A1 particles

U_0 (mm/s)	Transit time (s)
18.2	Sinks
13.7	Sinks
6.1	18.93
3.2	3.25 3.04 3.00 3.04 3.22
2.1	20.69 19.40 17.41 21.74 19.61

TABLE E.2

Raw Data for A2 particles

U_0 (mm/s)	Transit time (s)
18.2	4.27
	4.10
	3.32
	3.44
	3.34
	3.53
	3.73
13.7	2.76
	2.25
	2.80
	2.66
	2.71
6.1	1.42
	1.39
	1.35
	1.40
	1.40
3.2	1.56
	1.54
	1.53
	1.49
	1.54
2.1	3.21
	3.04
	2.98
	2.97
	3.00

TABLE E.3

Raw Data for A3 particles

U_o (mm/s)	Transit time (s)
18.2	1.96
	1.99
	2.05
	1.76
	1.87
	1.82
	1.97
	1.86
13.7	1.73
	1.76
	1.88
	1.79
6.1	1.19
	1.38
	1.22
	1.33
	1.34
3.2	1.40
	1.26
	1.41
	1.35
	1.28
2.1	2.36
	2.40
	2.28
	2.28
	2.33

TABLE E.4

Raw Data for A4 particles

U_0 (mm/s)	Transit time (s)
18.2	2.91
	3.91
	4.25
	4.11
	3.15
	3.50
	3.24
	4.18
	3.34
13.7	2.92
	2.69
	2.74
	2.81
	2.91
6.1	1.61
	1.46
	1.52
	1.62
	1.74
	1.33
	1.69
	1.60
3.2	1.62
	1.69
	1.61
	1.67
	1.71
2.1	3.23
	3.00
	2.91
	2.89
	3.43
	3.21
	3.15